DOCTORAL DISSERTATION

Computer simulations of structural and hopping conduction properties of disordered solids

Krisztián Koháry

Thesis advisors:

Dr. Sándor Kugler
Department of Theoretical Physics,
Budapest University of Technology and Economics,
H-1521 Budapest, Hungary

and

PD Dr. Sergei Baranovskii
Institut für Physikalische Chemie und Zentrum für
Materialwissenschaften der Philipps–Universität Marburg,
Philipps–Universität Marburg,
D-35032 Marburg, Germany

2001

Vom Fachbereich Physik der Philipps-Universität
als Dissertation angenommen am 18.06.2001
Erstgutachter: Prof. Dr. Koichi Shimakawa
Zweitgutachter: Prof. Dr. Peter Thomas
Tag der mündlichen Prüfung: 02.07.2001

Contents

1 Introduction **1**

2 Molecular dynamics simulation of amorphous carbon structures **3**
2.1 Introduction 3
2.1.1 Experimental background 3
2.1.2 Proposed models for tetrahedrally bonded amorphous carbon . 4
2.1.3 Computer simulations 5
2.2 Modeling the growth of amorphous carbon 8
2.2.1 Molecular dynamics calculations 9
2.2.2 First simulations 10
2.2.3 Numerical algorithm and simulation details 11
2.2.4 Energy dissipation 13
2.2.5 Structural properties and discussion 14
2.2.6 Summary 25
Bibliography for amorphous carbon 26

3 Atomistic simulation of the bombardment process during the BEN phase of diamond CVD **31**
3.1 Introduction 31
3.1.1 The bias enhanced nucleation CVD growth of diamond 31
3.1.2 Proposed model for the formation of diamond nuclei in the BEN process 32
3.2 Surface model of hydrogenated amorphous carbon 33
3.2.1 Generation of the surface model 33
3.2.2 Properties of the model 34
3.3 C_xH_y projectile bombardments. The simulation details 35
3.4 Results 39
3.4.1 Dissociation of the projectiles 39
3.4.2 Penetration of the projectiles 40
3.4.3 Structural rearrangement 42
3.5 Summary 45

Bibliography for C_xH_y bombardments 46

4 Growth of amorphous silicon **49**
4.1 Introduction 49
4.2 Simulation details 50
4.3 Structural properties 52
4.3.1 Time development of relaxations 54
4.3.2 Density 56
4.3.3 Ring statistics 56
4.3.4 Coordination number 57
4.3.5 Radial distribution and bond angle distribution functions . . . 58
4.4 Summary 58
Bibliography for amorphous silicon 60

5 One-dimensional hopping in disordered organic solids **63**
5.1 Introduction 63
5.2 Analytic theory 65
5.2.1 Drift mobility in the random-barrier model 66
5.2.2 Drift mobility in the random-energy model without correlations 69
5.2.3 Drift mobility in the random-energy model with correlated disorder 75
5.2.4 Concluding remarks 79
5.3 Monte Carlo simulations 79
5.3.1 Numerical algorithm and simulation details 80
5.3.2 Nearest neighbor hopping 83
5.3.3 Hopping with tunneling to further neighbors 84
5.3.4 Concluding remarks 86
Bibliography for one-dimensional hopping 89

Summary **91**

Zusammenfassung (in German) **94**

Összefoglalás (in Hungarian) **99**

Acknowledgments **102**

List of publications **105**

Curriculum Vitae **107**

Chapter 1

Introduction

Disordered materials have been the subject of numerous experimental and theoretical works for a significantly long period of time. There are several forms of disorder and they can be classified in the following way. Topological disorder is a structural arrangement where the long range order of a crystal is missing. This can be considered as the definition of *amorphous materials*, which are non-crystalline materials. Other types of disorder also exist. Substitutional disorder is where the units of the elementary cell change randomly with other units in the lattice. Vibrational disorder is where the positions of the atoms around their equilibrium positions are random due to temperature. Finally, some materials have magnetic disorder. Here the underlying crystal can posses randomly oriented spins at lattice points. Materials which are topologically disordered and posses a randomly oriented spin are called spin glasses. They must be not confused with "real" glasses. The latter are prepared by quick quenching from the melt. The glass transition appears when the supercooled liquid has a sudden change in derivative thermodynamic properties. Henceforth, we will define the glasses, which exhibit this glass transition. The glass transition temperature is always lower than the melting temperature for crystallines and it partly depends on thermal history.

It is highly important that one is aware of the detailed structure of amorphous materials, as this determines the main physical properties. The structure of amorphous covalently bonded materials is still however not known in detail and lots of physical phenomena are yet to be explained. The amorphous structure cannot be understood in terms of a unit cell consisting of a few atoms. The lack of periodicity in the material does not allow for the use of elegant theorems as used for crystalline structures. The complex nature of the systems also cannot be described by the means of theories used for the periodic structures of solids. In amorphous materials the structural information can only be determined in a statistical sense. Diffraction experiments are employed to retrieve information about atomic arrangements, which are to yield the radial distribution functions containing integrated information about the amor-

phous structures. Continuous random network models were proposed to describe the structure of covalent amorphous semiconductors on an atomic scale. In the past two decades, however, vast advances in information technology has allowed scientists to use computers in a more effective way to study disordered materials on the atomic scale.

Transport and energy relaxation of charge carriers in disordered solids has been the subject of intensive experimental and theoretical research for the past few decades. Detailed knowledge of the real underlying structure is not necessary in order to understand the electronic properties. Instead, simple models (extended Hamiltonians) were proposed, which are able to give reasonable descriptions for these physical properties. However, the model parameters used in these Hamiltonians could only be determined by some minimal information about the structure. It is possible to describe conductivity, mobility, thermopower, and other electronical properties of disordered materials with these models.

This thesis focuses on two physical properties of disordered materials: *(i)* on the *structure* of amorphous carbon and amorphous silicon, and *(ii)* on the *mobility* of the quasi one-dimensional disordered organic solids. In chapter 2, the description of the molecular dynamics simulation growth of amorphous carbon with low energy carbon bombardment is given. The atomistic simulation of the bombardment process during the bias enhanced nucleation phase of diamond chemical vapor deposition is presented in chapter 3. Chapter 4 deals with the study of the growth of amorphous silicon structures by the same preparation method as it was applied for the amorphous carbon structures (chapter 2). Finally, in chapter 5, the mobility of quasi one-dimensional organic semiconductors will be examined via Monte Carlo simulations. The thesis concludes with a summary in English, German and Hungarian.

Chapter 2

Molecular dynamics simulation of amorphous carbon structures

Amorphous carbon (a−C) has been the subject of numerous experimental and theoretical works in recent decades. The ability of carbon atoms to form sp^3, sp^2 and sp^1 bonding configurations leads to a large variation in structure. Various methods of preparation produce a wide range of macroscopic parameters for a−C. Tetrahedrally bonded amorphous carbon (ta−C) is found to be optically transparent, extremely hard and chemically inert whereas a−C which mostly consists of threefold coordinated atoms has a small gap in the electronic density of states. In amorphous forms of carbon the most elementary parameter is the ratio of fourfold, threefold, and twofold coordinated atomic sites which determine electronic and mechanical properties of the film.

In this chapter the growth of amorphous carbon thin film on a [111] diamond surface is studied with the tight-binding molecular dynamics technique. Six different three-dimensional networks were constructed with periodic boundary conditions in two dimensions. Time-dependent non-equilibrium growth was studied and densities, radial distribution functions, coordination numbers, bond angle distributions, and ring statistics were analyzed.

2.1 Introduction

2.1.1 Experimental background

At the early stage of structure investigations the amorphous carbon was studied using diffraction techniques. The obtained results show a wide range of structures. One of the first experiments was carried out by a Japanese group on an evaporated a−C sample using electron diffraction [kak60]. From the measured data they proposed a microcrystalline model of amorphous carbon structures, consisting of graphite-like

and diamond-like regions. The first neutron diffraction measurement was carried out by Mildner and Carpenter [mil82]. They estimated a 5% diamond-like atomic configuration in their sample. Li and Lannin published another neutron diffraction measurement on a sputtered a−C sample [li90]. The obtained radial distribution functions differed in detail from the theoretical models. A small fraction of sp^3 atoms were found and the chainlike configurations are also present in the disordered a−C network. The absence of a significant fraction of ordered sixfold rings was also shown, which was observed in glassy carbon. A diffraction study of a small volume of amorphous carbon materials prepared by filtered vacuum-arc method proposed nearly 100% of the sp^3 atomic configuration [gas91]. Another neutron diffraction study was employed on an anomalous a−C sample [shi91] in order to determine the atomic arrangement and to decide whether the structure has temperature dependence or not [kug93]. The sample contained mostly sp^2 atomic arrangements. One of the most recent neutron diffraction measurement was carried out at the Rutherford Appleton Laboratory [gil95]. About half a gram of tetrahedral amorphous carbon was prepared by deposition on glass substrates.

In the experiments amorphous carbon films are usually prepared by evaporation growth techniques. During the evaporation, carbon atoms are directed towards the target. If they reach the surface they could *(i)* scatter backwards, *(ii)* penetrate under the surface atoms, *(iii)* start collision-cascade, or *(iv)* chemically bond on the surface, producing the growth of amorphous carbon. The above mentioned processes (*(i)*−*(iv)*) depend mainly on the environmental conditions. The most important parameters are substrate temperature T_{sub} and the kinetic energy E_{beam} of bombarding carbon atoms. The diamond-like amorphous carbon is usually prepared at low pressure (10^{-5} mbar), with the substrate temperature lower than 80 °C. In the experiments, negative bias is usually applied to accelerate the carbon ions from the plasma, causing an extreme increase of initial kinetic energy (usually around 300−500 eV from 5−10 eV) [mil00]. However, there are some neutral atoms that mainly contribute to the surface growth because their kinetic energy (1−10 eV) is too low to penetrate under the surface.

2.1.2 Proposed models for tetrahedrally bonded amorphous carbon

The diamond-like amorphous carbon, otherwise frequently referred to as tetrahedral amorphous carbon (ta−C), has been the subject of several experiments and theoretical works in the last decade. This is so, as the material has lots of very good applicable parameters. The ta−C itself has a high percentage of sp^3 carbon atoms (nearly to even 100%) and the density of states has a wide gap, similar to that of a diamond. There are two main models which try to describe how the C^+ ions change the sp^2

rich matrix target to sp^3 rich film. These two models were proposed empirically from the results of experiments and computer simulations.

The so-called *subplantation model* is based on experimental observation and physical intuition. It was proposed in 1989 to describe the film deposition technology for semiconductors, metals, and ceramics with low energy E = 1−1000 eV hyperthermal species [lif89, lif90]. Later similar models were proposed by Davis [dav93] and Robertson [rob93]. In these models the ions are implanted into the subsurface of the film, producing densification and compressive stress in the process. The ion impact affects processes on three different time scales: *(i)* a collision stage involving penetration, energy loss and generation of ballistic displacements ($\sim 10^{-13}$ s), *(ii)* a thermalization stage, in which the excess energy is dissipated and the local structure relaxes ($\sim 10^{-12}$ s), *(iii)* a long-term relaxation stage in which temperature activated processes may occur ($> 10^{-10}$ s). It is postulated that the ions cause local melting near the impact site, a phenomenon known as "thermal spike" which anneals the surface region and reduces the stress.

An alternative model was proposed by Marks *et al.* [mar96a]. This suggests that the collision induced stress is stochastically localized on the surface and not in the subsurface region, arguing that the growth proceeds directly on the surface and not in the bulk region. For this, two-dimensional (2D) MD simulations were done on a graphite-like substrate with ion energies from 1 eV to 75 eV. It was emphasized that the simulations are not an attempt to reproduce the dynamics of a particular material, it should be viewed as a 2D model of a hypothetical material using a realistic interatomic potential. It is really hard to accept any result of this kind of simulations. However, it was found that the stress calculated in this 2D model reaches the maximum at 30 eV deposition energy and then gradually decreases at higher energies. This transition has not been previously reproduced by any simulation, but is commonly observed experimentally.

2.1.3 Computer simulations

There is no experimental method for the determination of microscopic structures in three dimensions. Efforts to develop simulation techniques for analyzing atomic scale structures are therefore continually being made. The research in this area has recently focused on the construction of realistic model structures for amorphous carbon using computer simulations by help of two basic methods. Both, the Monte Carlo (MC) and molecular dynamics (MD) simulations need local potentials that are usually difficult to derive yet are essential to simulations.

The MC method uses a random number generator to discover the phase space. For the initial structure a random packed matrix (or continuous random network) is usually chosen. Then an algorithm which satisfies the detailed balance is applied. The structure having the lowest energy is believed to have the best amorphous struc-

ture. A more efficient algorithm was proposed for continuous disordered systems by Barkema *et al.* in 1996 [bar96], which is called activation-relaxation technique (ART). Another simulation method based on MC simulations has also been developed by McGreevy and Pusztai [mcg88] for the investigation of non-crystalline structures. The Reverse Monte Carlo (RMC) scheme is based on the results of diffraction measurements and this is the only simulation method which is free from the description of the interaction between atoms. It was applied for amorphous carbon [wal98] providing a large scale three-dimensional model. MC simulations are very successful in finding the minimal energy structures. However, the dynamics of any system cannot be followed.

Molecular dynamics simulation is a technique to compute the equilibrium and transport properties of a classical many-body system. MD simulations are in many respects very similar to real experiments. When a MD study is done, a sample is prepared consisting of N particles and then the Newton equations of motion are solved for this system. Time averages for such a system almost represents that of a microcanonical ensemble (E,N,V), if one assumes that time average is equivalent to ensemble averages. The microcanonical ensemble is inconvenient both for theoretical analysis and also for comparisons of computed results with experimental data. Canonical and other ensembles can be derived using extended Hamiltonians. The reader can find more details about MC and MD simulations, for example, in the book by Allen and Tildesley [all90], and in the book by Rapaport [rap95].

In the MD simulations two different interatomic potentials are often applied. The first set of potentials are the classical empirical potentials. The most empirical potentials fell into two main groups. Pair potentials like Morse or Lennard–Jones 6−12 interatomic potentials are inapplicable to covalently bonded systems. The second group of interactions contain at least one additional term, i.e. three-body potential is included [ter88, bre90] . This term could stabilize the covalently bonded structure. The above two interactions between carbon atoms are the most commonly applied classical empirical potentials for large system with several hundred atoms [ter88, kau92, kel93, kau00, jäg00].

Although simulations based on empirical potentials achieved remarkable success, extension of the simulation method to quantum mechanics is important. A more accurate approach is to derive the interatomic potential directly from the electronic ground state where the total energy functional is calculated using density functional theory (DFT) within the local-density approximation (LDA). Unfortunately, DFT is very computer time-consuming, it is therefore unthinkable to perform a separate self-consistent electronic minimization at every MD step. The approach called Car-Parrinello method [car85] overcomes this difficulty and it has been successfully applied for MD simulations of covalently bonded amorphous systems yielding valuable structural and electronic information of small systems. Structural simulations

were carried out using *ab initio* or modified Car-Parrinello DFT method for a−C [gal89, mar96b, mcc00].

Larger systems are necessary to study for understanding complex dynamics processes such as growth. An alternative possibility to Car-Parrinello DFT method is to find tight-binding (TB) models that could be applied to larger systems (a few hundred atoms) and could be less time consuming than DFT [wan89, xu92, san89, els98]. In the last decade applications of different TB potentials were widespread in the MD study of carbon systems [dra91, wan93a, wan93b, dra94, jun94, por95, köh95, don98, uhl98, chu99].

The above quantum mechanical potentials were efficiently used to simulate the bulk of a−C structures. A common feature of the simulations was that each had an initial random network which was then annealed and cooled down near room temperature. Lots of physical parameters were recovered. Every model shows a very good agreement in the short-range order measured in these materials. Furthermore, other physical properties were compared like electronic density of states and vibrational density of states. In 1989, a simulation was made by Galli and her colleagues [gal89]. The disordered carbon network was generated by quenching from liquid using the Car-Parrinello method. The 54-atom-supercell reproduced well, the short-range order of the atomic structure and the electronic structure of a−C. In the work of Wang *et al.* [wan93a] the amorphous structure was generated by quenching from liquid phase. The supercell contained 216 atoms and the ring statistics analysis showed that the clusters formed graphite-like sheets at 2.20, 2.44 and 2.69 g/cm^3 densities as well. It was also found that at higher densities the fraction of fourfold coordinated atoms increased. In addition, contrary to previous MD quenching [gal89], twofold coordinated atoms were found in the amorphous matrix. Their latter work [wan93b] focused on ta−C. The 74% percentage of fourfold coordinated atoms was generated in a sample where the initial density was very high 4 g/cm^3. Note that the density of diamond is close to 3.5 g/cm^3. At that density the structure consisted 80% of sp^3 carbon atoms, and then by decreasing the density, the sp^3 content decreased to 74%. Drabold *et al.* [dra94] criticized the transferability of the potential [xu92] used in the works of Wang *et al.* [wan93a, wan93b]. However, Wang and Ho argued with this statement [wan94]. Recently, a more accurate form of their carbon potential was published [tan96]. The above preparation methods do not contain the information of the growth of amorphous carbon.

Atomic scale modeling of ion-beam-induced growth of amorphous carbon was simulated by Kaukonen and Nieminen [kau92, kau00] and by Jäger and Albe [jäg00]. The work of Kaukonen and Nieminen [kau92] – redone later [kau00] – report 1−150 eV ion beam kinetic energy window simulations. The empirical Tersoff [ter88] potential described the interatomic interaction between carbon atoms. It was found in the latter work that the low energy (10−40 eV) bombardment produces the highest sp^3

content in the host matrix, supporting the model proposed by Marks *et al.* [mar96a]. However, the sp^3 content was half of the experimental observed value. In the work of Jäger and Albe [jäg00] a similar simulation work was carried out with the Tersoff's [ter89] and Brenner's [bre90] potential. They have found that the fraction of tetrahedrally coordinated atoms is too low, even if structures with densities close to diamond are obtained. However, changing the cutoff distance in Brenner's potential, the sp^3 fraction close to 82% was found, which is in good agreement with experiments. This modification has an undesired side effect, it has increased the fraction of fivefold coordinated carbon atoms, which was never observed by any quantum mechanical treatment of interatomic potentials. A general problem of classical potentials that are fitted to a limited set of materials properties is their accuracy in describing processes which cover areas lying far from the fitted points of the potential energy hyperface. In the case of a−C (and t−aC) deposition the validity of using classical empirical potentials can be argued.

It means that quantum mechanical potentials are needed to describe interatomic potentials. The first pioneer work was done by Uhlmann *et al.* [uhl98]. In this work the diamond-like carbon (DLC, ta−C) films were investigated by bombardment with neutral carbon atoms a 3 g/cm^3 amorphous film. The results supported the subplantation model. It was shown that for E $>$ 30 eV the deposition is a subplantation process, where the carbon atom species penetrate and occupy subsurface positions, producing a defective, low density, sp^2 rich surface layer and a dense, sp^3-rich layer is formed below this surface. Chu-Chun Fu *et al.* [chu99] published a simulation method for the film growth over silicon substrate. The silicon surface is assumed to enhance hardness through the formation of a large proportion of tetrahedral bonds. They published that a mixed thin layer in the surface preferring carbon-silicon bonds to carbon-carbon bonds were formed at impinging energy 7.55 eV of carbon atoms. This simulation contained only 9 and 16 bombarding carbon atoms. The above two results were published very recently. The project which was done in part of this Ph.D. thesis was started long before these results were achieved and will be summarized in the next section.

2.2 Modeling the growth of amorphous carbon

The aim of this chapter is to describe in detail the low energy (1−5 eV) bombardment of the target surface. If the carbon atom reaches the surface with such a low kinetic energy the probability of its penetration under the surface and the probability that it starts a collision-cascade is very low. It can however sometimes scatter backwards and can chemically bond on the surface producing the growth of amorphous carbon. These statements allow us to study the growth of amorphous carbon in this environment. We address here the analysis of the growth of amorphous carbon with quantum

mechanical treatment of the interatomic potential on large scale systems with over 100 atoms.

2.2.1 Molecular dynamics calculations

Molecular dynamics simulations were carried out to study the dynamics of the growth process. The tight-binding (TB) Hamiltonian of Xu, Wang, Chan, and Ho [xu92] was used to calculate the interatomic potential between carbon atoms. All the parameters and functions of these methods were fitted to the results of local density functional calculations. In that scheme, the system is described by a Hamiltonian of the form

$$H(\{\vec{\mathbf{r}}_i\}) = \sum_i \frac{\vec{\mathbf{p}}_i^2}{2m_i} + \sum_n^{occupied} \langle \Psi_n | H_{TB}(\{\vec{\mathbf{r}}_i\}) | \Psi_n \rangle + E_{rep}(\{\vec{\mathbf{r}}_i\}) \tag{2.1}$$

where $\{\vec{\mathbf{r}}_i\}$ denote the positions of the atoms (i = 1, 2, ..., N), and $\vec{\mathbf{p}}_i$ is the momentum of the ith atom. The first term in Eq. (2.1) is the kinetic energy of the ions. The second term is the electronic band-structure energy calculated from a parameterized tight-binding Hamiltonian $H_{TB}(\{\vec{\mathbf{r}}_i\})$. It consists of the sum of the energy eigenvalues E_i for the occupied part of the electronic band structure, which is calculated by the Slater-Koster empirical tight-binding method [sla54] with the tight-binding parameters determined by fitting the calculated electronic structure of carbon. The off-diagonal elements of H_{TB} are described by a set of orthogonal sp^3 two-center hopping parameters, $V_{ss\sigma}$, $V_{sp\sigma}$, $V_{pp\sigma}$, $V_{pp\pi}$, scaled with interatomic separation r as a function $s(r)$ (Eq. 2.2); and the on-site elements are the atomic orbital energies of the corresponding atom. The third term is a short-ranged repulsive energy. It represents the sum of the ion-ion repulsion and the correction to the double counting of the electron-electron interaction in the second term. In this scheme, the quantum mechanical nature of the covalent bonding among the carbon atoms is explicitly taken into account in the electronic structure which is calculated for each of the atomic configurations in the MD simulations. Details of the tight-binding model are described in reference [xu92]. The interatomic potential describes accurately the energetic, vibrational, and elastic properties of the diamond (fourfold), graphite (threefold), and linear-chain (twofold) structures in comparison with self-consistent first-principles density functional calculations. The realistic TB potential has already been used for preparation of amorphous carbon [wan93a], tetrahedrally bonded amorphous carbon [wan93b] and successfully applied for preparation of fullerenes [zha92, las98].

The orbital basis used is $2s$ and $2p$. The off-diagonal elements for the tight-binding Hamiltonian are given in terms of a function of the interatomic distance $s(r)$

$$s(r) = \left(\frac{r_0}{r}\right)^n \exp\left\{n\left[-\left(\frac{r}{r_c}\right)^{n_c} + \left(\frac{r_0}{r_c}\right)^{n_c}\right]\right\}. \tag{2.2}$$

This function contains four independent parameters, that have been adjusted with results of *ab initio* calculations or experiments. The diagonal elements, as well as the hopping integrals for the equilibrium distance for one particular structure have also been parameterized, and are given in the tables of reference [xu92]. The repulsive energy is a function for the sum of pair interactions, of a similar functional form as $s(r)$, with again four independent parameters which are also taken from the previous reference

$$\phi(r) = \phi_0 \left(\frac{d_0}{r}\right)^m \exp\left\{m\left[-\left(\frac{r}{d_c}\right)^{m_c} + \left(\frac{d_0}{d_c}\right)^{m_c}\right]\right\}. \tag{2.3}$$

To use these interactions in a MD simulation it is necessary to introduce a cutoff for the interatomic distances. This is particularly important in cases where periodic boundary conditions are imposed, so that replicas of the same atom do not interact with each other.

For integration of Newton's equations of motion the velocity Verlet algorithm was used with time step of 0.5 fs:

$$\vec{\mathbf{r}}_i(t+\Delta t) = \vec{\mathbf{r}}_i(t) + \vec{\mathbf{v}}_i(t)\Delta t + \frac{1}{2}\vec{\mathbf{a}}_i(t)\Delta t^2 + \mathcal{O}(\Delta t^3) \tag{2.4}$$

$$\vec{\mathbf{v}}_i(t+\Delta t) = \vec{\mathbf{v}}_i(t) + \frac{\vec{\mathbf{a}}_i(t+\Delta t) + \vec{\mathbf{a}}_i(t)}{2}\Delta t. \tag{2.5}$$

The attractive forces were obtained using the Hellmann-Feynman theorem. The Hellmann-Feynman force on atom i is

$$\vec{\mathbf{F}}_i = -\sum_n^{occupied} \langle\Psi_n|\partial H_{TB}(\{\vec{\mathbf{r}}_i\})/\partial\vec{\mathbf{r}}_i|\Psi_n\rangle, \tag{2.6}$$

where the sum is over occupied levels. The repulsive forces are directly the gradient of E_{rep}. Finally, we would refer to two articles which describe the above tight-binding molecular dynamics method in more details: the work of Wang *et al.* [wan89] with orthogonal basis, whose scheme is used in this chapter for simulation of growth process of a−C and the work of the Paderborn group [els98, fra00], which uses non-orthogonal basis.

2.2.2 First simulations

The review of our computer simulations will be given in this section. This project started in 1997 and our aim was to find the best treatment of the description of a−C growth using quantum mechanical treatment of applied potential.

First, we applied 0 K substrate which is the simplest method to simulate the energy dissipation process during the collision of bombarding atoms and the substrate

atoms. The quantity *critical distance* was introduced, which was chosen 17% larger than the first neighbor bond distance in diamond (1.54 Å). We used the following model. If a bombarding carbon atom arrived in the neighborhood of a substrate atom, it became the part of atoms where the kinetic energy was decreased in every time step with a given number, which was smaller, but close to one. If the next bombarding atom arrived in the neighborhood of the substrate atom or the closeness of the atoms whose kinetic energy decreased in every time step, the similar decrease of energy was employed. This model can be considered as the cooling of the bombarding atom in the region of the impact, decreasing its kinetic energy in every time step. The zero temperature of the substrate provides the quickest energy dissipation. The first results showed that the low energy (1.29 eV) bombardment gives a more chainlike structure and the higher energy bombardment close to 10 eV provides more amorphous network structures [koh98a, kug99].

To improve the description of energy dissipation in our computer experiments the task of finding the better temperature control of the substrate was addressed. There are several opportunities to control the temperature in MD simulation. The Nosé-Hoover thermostat uses extended Hamiltonian and describes the canonical ensemble in the right statistical physics form. In the case where the particle number N in the system tends to infinity, it can be shown that the canonical ensemble can be realized approximately in equilibrated systems. However, systems with size $N \approx 100$ already show very good results. Unfortunately, it turned out that the non-equilibrium growth process cannot be simulated with the above description of constant substrate temperature [koh98b]. The failure of the use of Nosé-Hoover thermostat does not mean that the constant temperature cannot be realized in the simulations.

For the next step we decided to use substrates, with fixed atoms in the bottom layer and giving initially 0 K to the remaining atoms in the substrate. The results of the simulations provided similar results as the rigid substrate [kug98] with 6.5 and 13 eV bombardment. The snapshots of the final structures are shown on Fig 2.1. It is supported by the results that lower kinetic energy bombardment supports more chainlike structures and that larger energy constructs more amorphous structures. It was also shown that the kinetic energy of the atoms in the film decreases near exponentially after no further bombarding atoms appeared in the film [koh00]. This behavior will be discussed in more detail later in this chapter.

2.2.3 Numerical algorithm and simulation details

In this section a more realistic model of amorphous carbon deposition will be given [koh01]. The simulation technique was as follows. An ideal diamond film consisting of 120 atoms was employed to model the substrate. The rectangular simulation cell was open along the positive z-axis ([111] direction in our case) and periodic boundary conditions were used in planar, x and y directions. Atoms in the bottom substrate

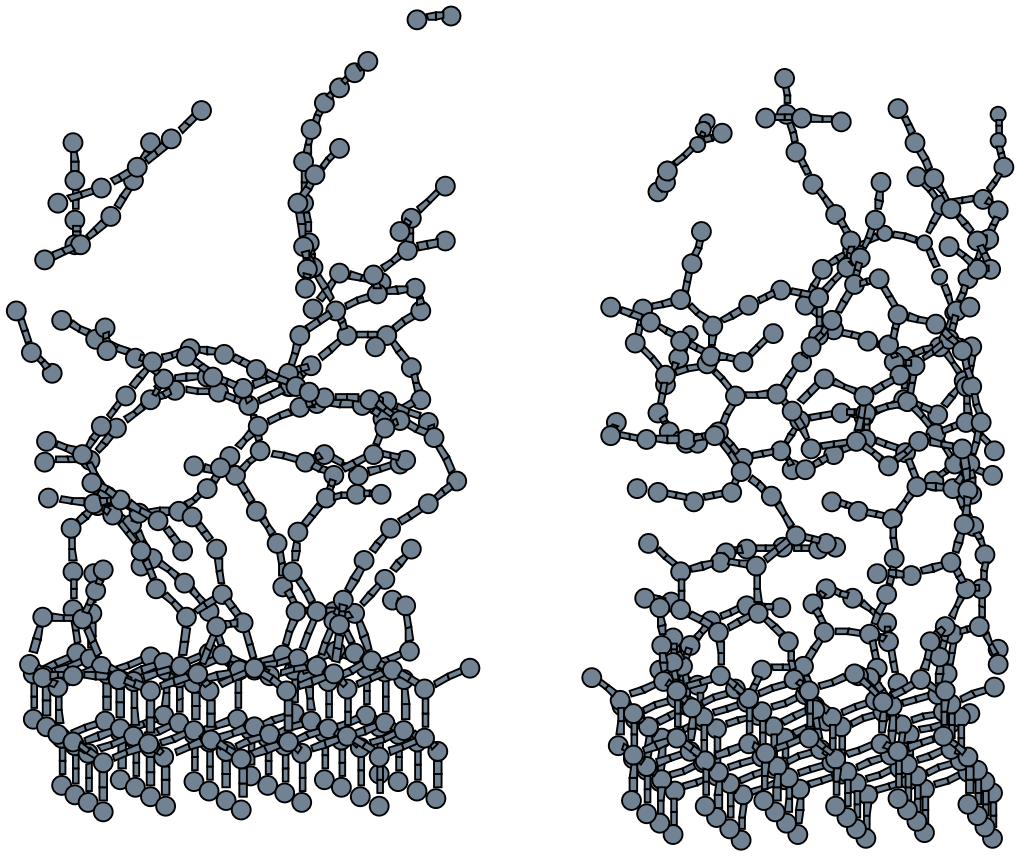

Figure 2.1: The final structures of the atom-by-atom deposition. The left model is chainlike amorphous structure with deposition energy 6.5 eV. It contains 286 atoms including 120 atoms in the substrate. The right model shows the structure made after 13 eV deposition. It contains 323 atoms.

layer were fixed at their ideal lattice positions, whereas the rest of the 96 atoms in the uppermost substrate layers were allowed to move with full dynamics. To simulate the constant substrate temperature the kinetic energy of the moveable atoms in the substrate were rescaled in every time step. The velocity Verlet algorithm was used to determine the trajectories of the carbon atoms. Time step was chosen to be equal to 0.5 fs.

Before starting the deposition process, substrate was kept at a given temperature for 0.5 ps in order to make structural relaxation. The neutral bombarding atoms were randomly placed in x and y directions above the substrate as near as possible, but not closer to any other atom than the cutoff distance of the potential. The initial velocities of bombarding atoms were directed to the substrate with given kinetic

energy. There is no thermal equilibrium so initial velocities were chosen using the $v = \sqrt{\frac{2E_{beam}}{m}(1.2 - 0.4 \times p)}$ simple relation, where p is a uniformly distributed random number between 0 and 1. Directions were determined by $\theta = 120^\circ + 60^\circ \times p$ and $\phi = 360^\circ \times p$, where θ and ϕ are the polar angles and p is again a random number.

The frequency of the atomic injection was $f = 1/125$ fs^{-1} on average: in every MD time step a random number was generated and was compared to a given number (in the present case it was 0.004), to see if it is greater or lower. In case of the latter, a new particle is "created" and it started its motion bombarding the substrate. It means that on average in every $0.004^{-1} = 250$th MD step, the random number was smaller than 0.004. The time step was equal to 0.5 fs, i.e. 250×0.5 fs = 125 fs was the average time period to put a new atom into the atomic current. This flux is in the orders of magnitude larger than the deposition rate usually applied in real experiments. We found, however, that even at such a high flux the overheating effect of the surface (see, e.g., [kau92]) can be negligible and the low-energy evaporation can be modeled. The lower substrate temperatures applied in our simulations results in faster energy dissipation, which compensates for the high deposition rate. The initial kinetic energies of the atoms in the beam were dissipated by interacting with the surface atoms, whereas their trajectories were followed with full dynamics. We note here that some atoms were scattered back and needed to be cut from the system. This kind of backscattering can be found in the experiments as well.

2.2.4 Energy dissipation

In the experiments the magnitude of the atom flux in the atom-by-atom deposition techniques is 10^{14} cm^{-2}s^{-1}. It means, that on average one atom bombards the approximately 10×10 Å^2 substrate surface in one second. Computers cannot perform simulations in the above time scale. The typical time step chosen is around 1 fs and the calculations over several picoseconds last several weeks (months) for systems having 100−200 atoms and if the interatomic potential is described by quantum mechanical treatment. Due to the problems mentioned above, all the details of the growth cannot be realized by the help of computer simulations. However, the short time processes, like energy loss and local thermalization can be simulated, as these processes are in picosecond range. It is an approximation that the growth process can be simulated with the above time step, when the frequency of bombarding is close to $1/125$ fs^{-1}. Kaukonen and Nieminen [kau92] reported that an overheating effect can sometimes be observed. To decide weather it plays an important role in our quantum mechanical treatment of the problem, we performed computer simulations with only one bombarding atom over the 80 atoms substrate surface with 100 K. The time step Δt equal to 0.1 fs was chosen. A carbon atom was placed 2.75 Å over the substrate. The initial kinetic energy of the bombarding carbon atom was chosen to 10 eV and has only z-directional velocity. We performed simulation placing the carbon atom in

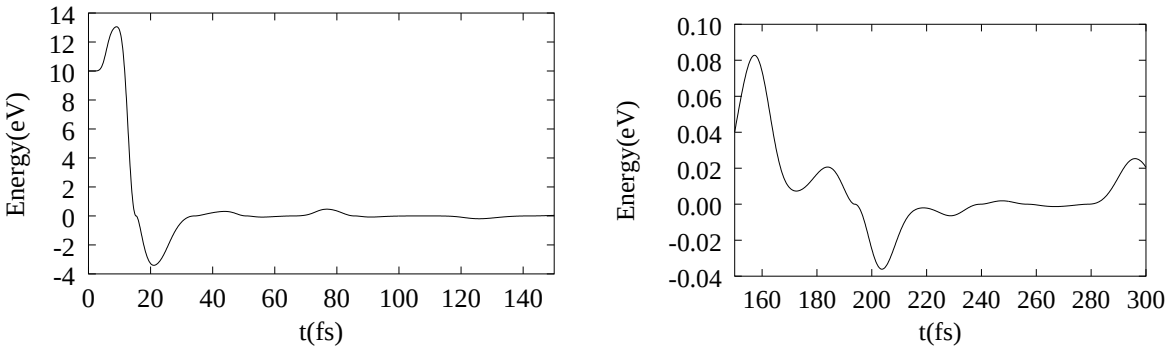

Figure 2.2: The z-component kinetic energy of the bombarding atom. In the figure on the left the time interval 0−150 fs, while in the figure on the right the interval 150−300 fs can be seen.

high symmetrical points over the surface and one general place. The Fig. 2.2 shows the z component kinetic energy changes for the bombarding atom. It can be seen that the carbon atom bounced back after 15 fs and loses its initial kinetic energy after 40 fs. Then oscillations of kinetic energy around 0 eV with 0.1 eV deviations can be found, as it is clear from the Fig. 2.2. This shows that the 1/125 fs^{-1} flux is acceptable in our computer simulations.

2.2.5 Structural properties and discussion

Six different structures were made by our method (see section 2.2.3): models constructed with 25 ps and 40 ps (denoted by L) injection times, and with average kinetic energy E_{beam} = 1 eV and 5 eV at T_{sub} = 100 K substrate temperature (e1T100, e5T100, e1T100L and e5T100L) and two other models by 25 ps injection, E_{beam} = 1 and 5 eV energy with substrate temperature of 300 K (e1T300, e5T300). In all cases the structures were relaxed for 5 ps after the deposition, i.e. a bombarding atom no longer appeared in the system. The final structures of larger models (e1T100L and e5T100L) made by different bombarding energies consist of almost the same number of atoms (177 and 172), with a thickness of 12.65 Å and 10.98 Å. Models e1T100, e5T100, e1T300 and e5T300 have 126−129 atoms. Typical central processing unit (CPU) times of simulations are about 50−70 days on DEC-Alpha workstations. Snapshots of two films (e5T100L and e5T300) are shown in Fig. 2.3 and 2.4 after growth and relaxation. The substrate at T_{sub} = 100 K remained similar to crystal lattice, while atoms left their position and the topological order became broken during growth at T_{sub} = 300 K. An atom (open circle) in the middle of the amorphous part in Fig. 2.4 originally belonged to the substrate.

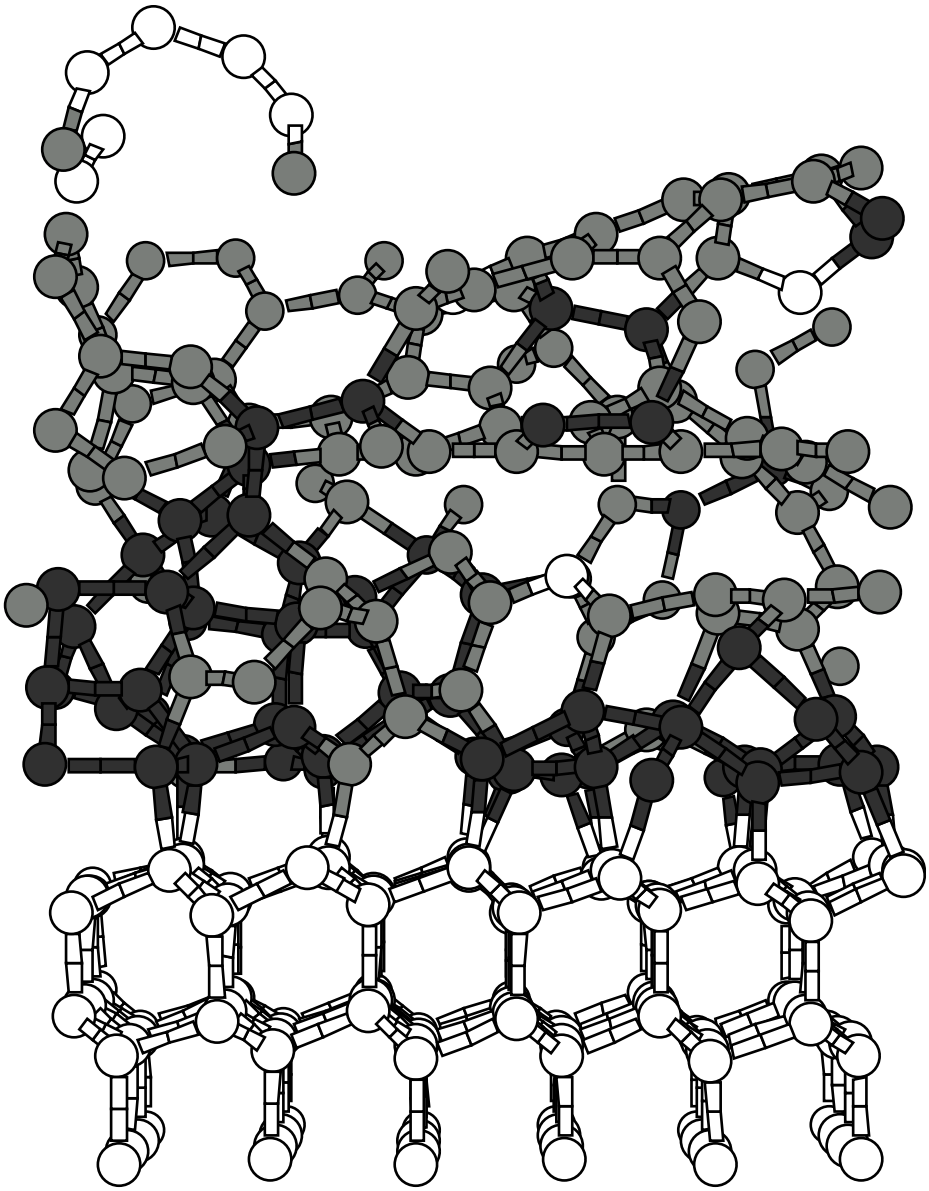

Figure 2.3: A snapshot of the e5T100L model is shown after growth and relaxation. The substrate (open circles at the bottom) at $T_{sub} = 100$ K remained similar to the crystal lattice during growth. Black and grey atoms are fourfold and threefold coordinated, respectively. The rest of the open circles correspond to twofold and one onefold coordinated atoms. For a color version see: http://www.phy.bme.hu/∼kohary/aCfigures.html

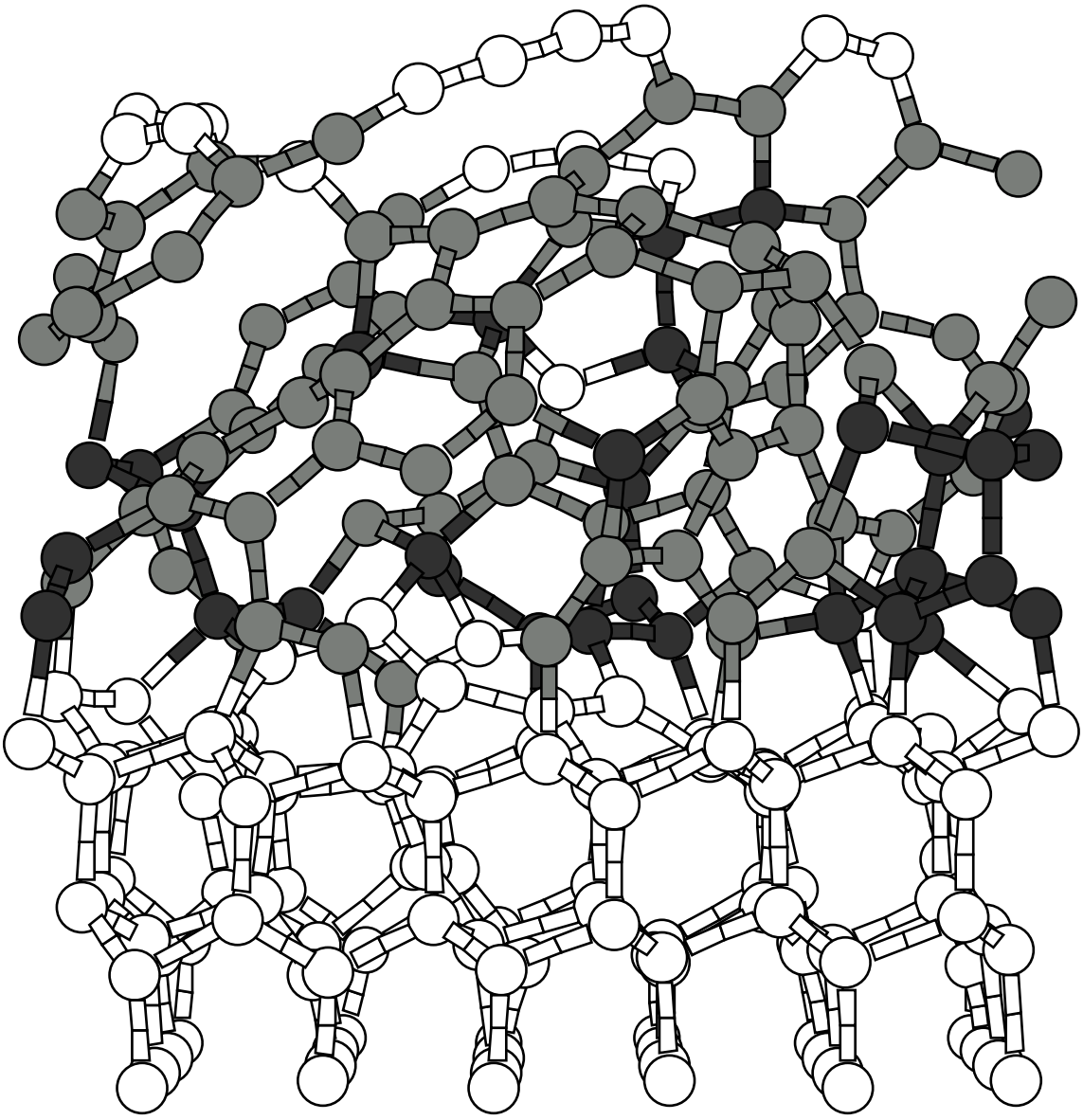

Figure 2.4: A snapshot of the e5T300 is shown after growth and relaxation. The substrate at T_{sub} = 300 K lost even the topological structure of a perfect crystal during growth. An atom (open circle) in the middle of the amorphous part in figure originally belonged to the substrate. For a color version see: http://www.phy.bme.hu/~kohary/aCfigures.html

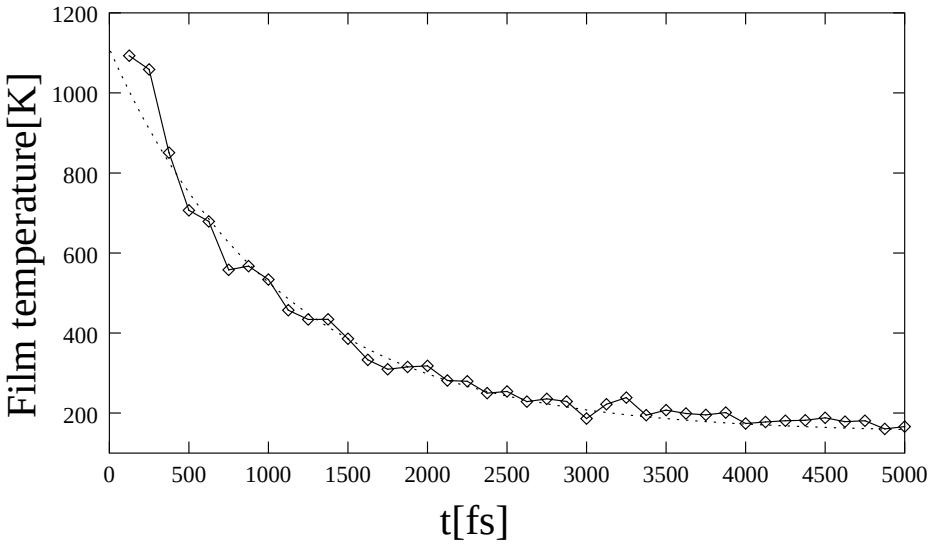

Figure 2.5: The temperature versus time during relaxation of e1T100L model is shown. The fit is described by $T_{film} = (\exp(t[fs]/1069.03 + 6.8) + 150)$ K, which has an incorrect asymptotic behavior.

Time development of relaxations

After the growth process the films relaxed with full dynamics for 5 ps. During this period the substrate was kept at constant temperature while the deposited networks were cooling down. The temperature versus time relation of this non-equilibrium process is exponential function in the interval [0:5000] fs as shown in Fig. 2.5 for e1T100L model.

The best fit was done according to $T_{film}(t) = c + \exp(a \cdot t + b)$ K. The constant $c = 150$ K was chosen rather than 100 K, which has a false asymptotic behavior, but it gave a better fit. Fitting parameters are a = -0.935 ps^{-1} and $b = 6.8671$ and $c = 150$ K. This means that the relaxation time $\tau = -1/a$= 1069.03 fs $\approx$ 1.07 ps.

The time dependence of bond length and bond angle deviations were also investigated. In crystals, bond lengths and bond angles only have thermal disorder components as a result of the thermal fluctuations. Non-crystalline materials have an additional broadening contribution to the bond length and bond angle distribution resulting from static disorder. First we calculated the standard deviations $\sigma(t_k)$ at discreet times t_k in the following way:

$$\sigma(t_k) = \sqrt{\frac{1}{N}\sum_{j}^{N}\left(d_j(t_k) - \frac{\sum_{i=1}^{N} d_i(t_k)}{N}\right)^2} \tag{2.7}$$

where N is the number of bonds and $d_i(t_k)$ is the ith bond distance. Values between 0.095 Å $< \sigma_b <$ 0.11 Å were obtained for bond length deviations. (The index b

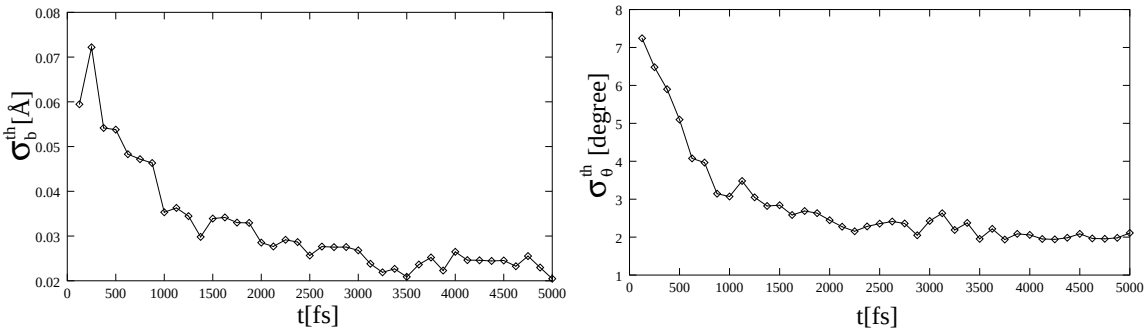

Figure 2.6: As shown, an expected σ_b^{th} and σ_Θ^{th} versus time functions have an exponential decay. At the beginning of relaxation when the temperature of the film is about 1000 K the thermal part of the fluctuation is important while at the end it plays only a minor role.

is for bond length.) Similar calculations for bond angle deviations provided $\sigma_\Theta(t_k)$ within an interval of 11.7°-12.8°. The contribution to standard deviation of thermal fluctuation was also studied as a function of time using the following term:

$$\sigma^{th}(t_k) = \sqrt{\frac{1}{N}\sum_i^N \left(d_i(t_k) - \langle d_i \rangle\right)^2} \tag{2.8}$$

where time average $\langle d_i \rangle$ of bond d_i is used instead of $d_i(\mathrm{T} = 0\ \mathrm{K})$.

As expected σ_b^{th} and σ_Θ^{th} versus time functions have an exponential decay as shown in Fig. 2.6. At the beginning of relaxation, when the temperature of the film is about 1000 K, the thermal part of the fluctuation is important. At the end it plays only a minor role. The σ_b^{th} and σ_Θ^{th} values as a function of temperature show linear relationships, as displayed in Fig. 2.7. Straight lines do not intersect origin because usually $\langle d_i \rangle \neq d_i(\mathrm{T} = 0\ \mathrm{K})$.

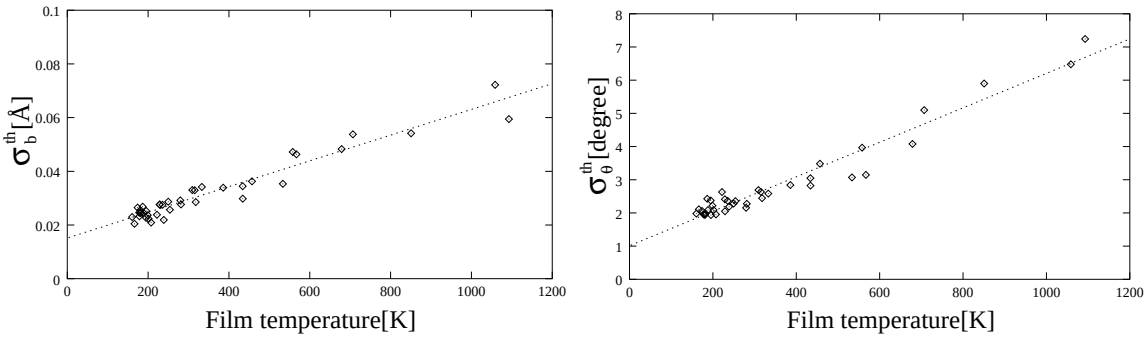

Figure 2.7: The σ_b^{th} and σ_Θ^{th} in function of temperature show linear relationships. Straight lines do not intersect origin because usually $\langle d_i \rangle \neq d_i(T = 0)$.

Table 2.1: It contains the number of atoms (No.), the percentage of atoms with different coordination numbers (Z), the average coordination number $\langle Z \rangle$, the thickness z_d, and the density ρ of different models. The two rows belong to bulk (top) and to total (lower) sample, respectively. For bulk models the densities are always larger than for the total sample.

Model	No.	Z=2	Z=3	Z=4	$\langle Z \rangle$	z_d(Å)	$\rho(g/cm^3)$
e1T100	113	0.9	59.3	39.8	3.4	6.5	3.0
	129	7.0	56.6	34.9	3.2	9.5	2.3
e5T100	124	4.8	58.1	37.1	3.3	7.7	2.7
	129	7.0	55.8	35.7	3.3	10.7	2.0
e1T300	121	5.8	71.9	21.5	3.1	9.8	2.0
	130	7.7	70.8	20.0	3.1	12.8	1.6
e5T300	92	0.0	68.5	31.5	3.3	6.3	2.3
	126	11.1	64.3	24.6	3.1	9.3	2.1
e1T100L	160	5.0	65.0	30.0	3.2	11.0	2.4
	177	9.0	62.1	27.1	3.1	14.0	2.1
e5T100L	151	2.0	55.6	42.4	3.4	9.4	2.7
	172	4.7	56.4	38.4	3.3	12.4	2.3

Density

For density calculations, two different volumes were defined: we will refer to them as cells for the total sample and for the bulk. The bottom of the cells were 0.77 Å lower than the bottom carbon atom in the amorphous network. This is almost at half bond distance of bonds between the substrate atoms and the bottom carbon atoms in the film. The top of the cells were determined differently. For the total sample the top of the cell was the highest z-coordinate that occurs for atoms in the network. For the bulk, this z coordinate was decreased by 3 Å. The x and y size of the cell was determined according to two-dimensional periodic boundary conditions. Table 2.1 contains the densities of different models. Each row is divided into further two rows. The upper rows constantly refer to the bulk and the lower rows refer to the total sample. For bulk models the densities are always larger than for the total sample. At $T_{sub} = 100$ K bulk densities are between 2.7 and 3.0 g/cm^3 except for model e1T100L where the density is equal to 2.4 g/cm^3. The reason for lower density is that on the top of the network a void appeared, thus drastically decreasing the local density. At $T_{sub} = 300$ K the structures are less dense (2.0−2.3 g/cm^3).

In Fig. 2.8 density profiles of two networks (e1T100 and e1T300) are displayed perpendicular to the substrate surface. The arrows represent the layer positions in a perfect diamond crystal. The difference in temperature between two substrates

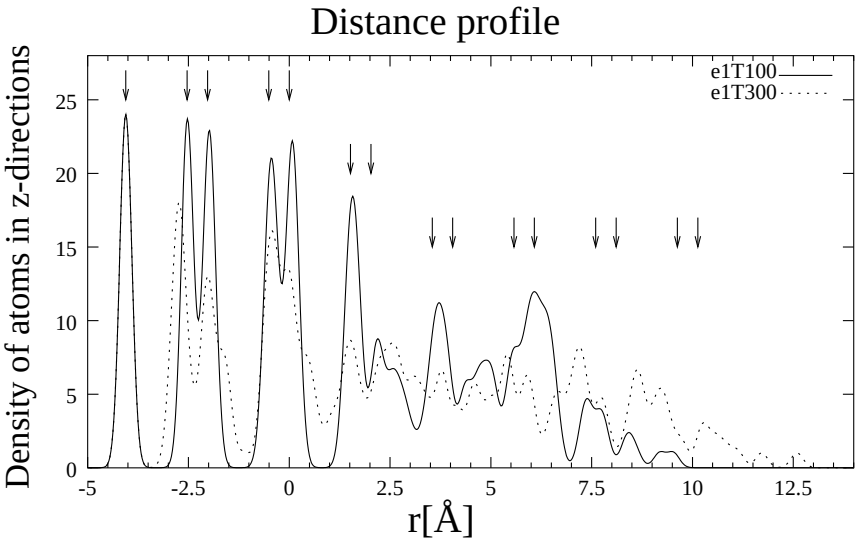

Figure 2.8: Density profiles of two films, e1T100 (solid line) and e1T300 (dotted line), are displayed perpendicular to the substrate surface. Arrows represent the layer positions in a perfect diamond crystal. The difference in temperature between the two substrates causes a difference between memory effects.

causes a difference between memory effects. The structure on the surface at 100 K has a more pronouncing layering effect than the other network on substrate at room temperature. In the first 3−4 Å thick layers over the [111] surface the sp^3 content is high due to the memory effect. In the rest of the bulk the sp^2 content is dominant.

Radial distribution function

The two radial distribution functions of model e1T100L are displayed in Fig. 2.9. The solid line shows the first and second neighbor contributions to RDF before relaxation, while the dashed line belongs to these contributions after relaxation. Peaks in the final structure seem to be a bit narrower and in the interval of 1.6−2.2 Å there are less bond lengths after relaxation. Numerical analysis provides the same conclusion. In Fig. 2.10 partial distribution functions $J_{i,j}$ of e1T100L can be seen, where i and j denote the coordination numbers of the connected atoms. Table 2.2 contains the average bond distances which are 1.43 Å, 1.52 Å, and 1.59 Å, for $J_{3,3}$, $J_{3,4}$ and $J_{4,4}$, respectively.

Coordination number

For bond counting we used a value of 1.85 Å as an upper limit of bond length inside the first coordination shell. Table 2.1 shows the percentage of different coordinations. There is no fivefold atom in the structures. More than half of the atoms have the sp^2

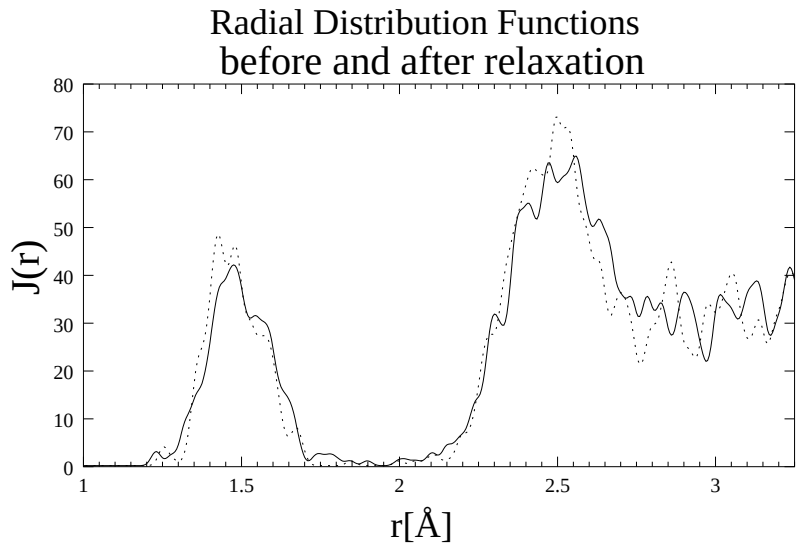

Figure 2.9: Two radial distribution functions of model e1T100L are displayed here. The solid line shows the first and second neighbors contributions to RDF before relaxation, while the dashed line shows these contributions after relaxation. First and second neighbor peaks in the final structure are a bit narrower.

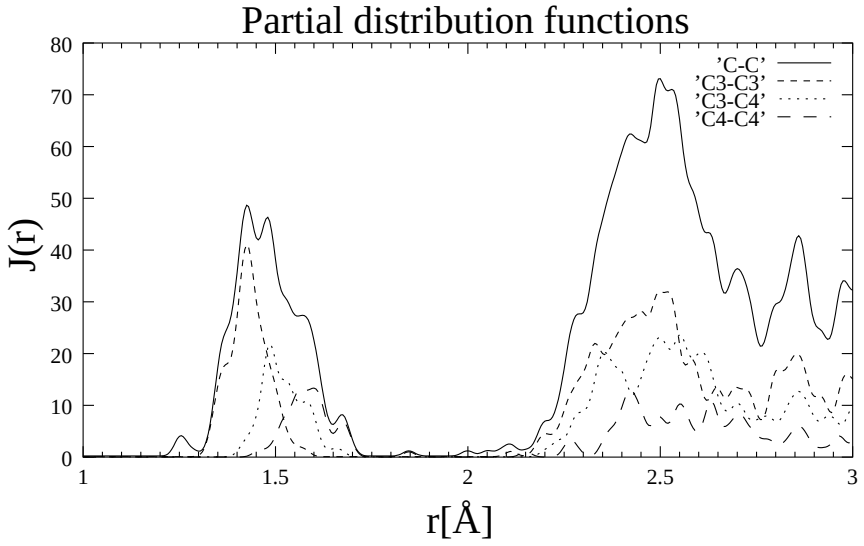

Figure 2.10: The total (C−C) and partial (C3−C3, C3−C4 and C4−C4) distribution are shown in e1T100L model. The '3' and '4' denote the coordination number three and four. The average bond distances are 1.43 Å, 1.52 Å, and 1.59 Å for C3−C3, C3−C4 and C4−C4, respectively.

Table 2.2: Average bond distance statistics

Model	C−C distance(Å)							
	C−C	σ_{C-C}	C3−C3	σ_{C3-C3}	C3−C4	σ_{C3-C4}	C4−C4	σ_{C4-C4}
e1T100	1.51	0.09	1.41	0.04	1.53	0.05	1.60	0.07
	1.50	0.10	1.41	0.04	1.53	0.05	1.60	0.07
e5T100	1.50	0.09	1.44	0.05	1.53	0.05	1.58	0.06
	1.50	0.09	1.44	0.05	1.53	0.05	1.58	0.06
e1T300	1.48	0.09	1.43	0.05	1.54	0.06	1.58	0.09
	1.48	0.09	1.43	0.05	1.55	0.06	1.58	0.09
e5T300	1.50	0.09	1.43	0.05	1.54	0.06	1.58	0.06
	1.48	0.09	1.43	0.05	1.54	0.06	1.58	0.06
e1T100L	1.49	0.09	1.43	0.05	1.52	0.05	1.59	0.07
	1.49	0.09	1.43	0.05	1.52	0.05	1.59	0.07
e5T100L	1.52	0.09	1.44	0.06	1.54	0.06	1.59	0.06
	1.51	0.09	1.44	0.05	1.54	0.06	1.59	0.06

bonding configuration in the models as shown in Table 2.1. The average coordination numbers in the bulk were slightly over the graphite coordination. The dominating part of fourfold coordinated atoms is near the substrate and the contribution of twofold coordinated atoms is due to the atoms at the top of the amorphous network (see Fig. 2.3 and 2.4). The e5T100L model contains a onefold coordinated carbon atom at the end of a chain. When we compare the average coordination numbers there are no drastic differences among the simulated models. A MD simulation of Kaukonen and Nieminen [kau92], using the classical empirical potential of Tersoff, shows the same portion of sp^2 but the sp^1:sp^2:sp^3 ratio is slightly different at T_{sub} = 300 K. At the E_{beam} = 1 eV beam energy 5.8:71.9:21.5 is the ratio in the e1T300 model, while it is 19.0:73.2:6.7 in their case. Our sample has a higher portion of diamond-like atoms and less twofold coordinated carbon atoms at the same condition.

Bond angle distribution

The angles can be analyzed in detail according to the coordination numbers of the neighbors and the center (e.g. C3−C4−C3, C4−C4−C4, etc.) From diffraction data this causes more difficulties. In Fig. 2.11 we display the bond angle distribution of model e1T100L, where the central atoms are threefold (C−C3−C) and fourfold coordinated (C−C4−C). In graphite-like crystal and in diamond lattice these angles are 120° and 109.47°, respectively.

The average values of partial bond angle distributions and deviations are gathered in Table 2.3 and Table 2.4. Atoms with sp^3 local arrangements have nearly the same

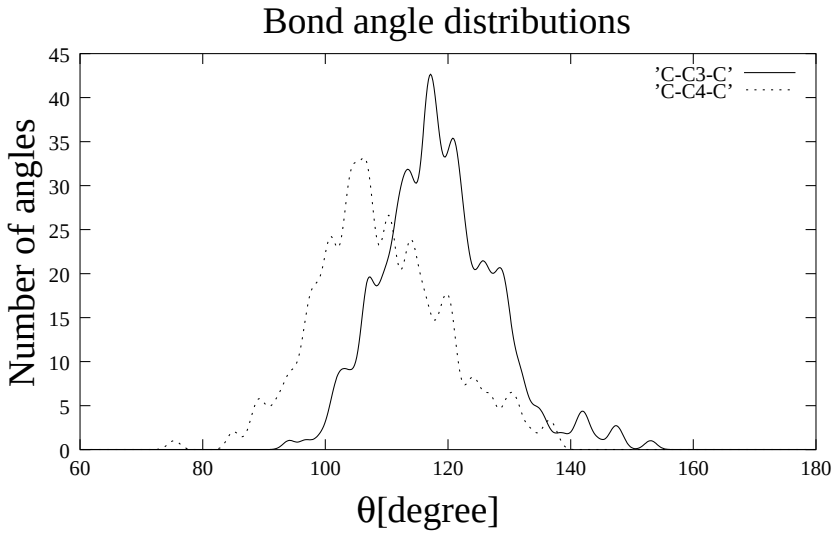

Figure 2.11: The bond angle distribution of model e1T100L, where the central atoms are threefold (C−C3−C) and fourfold coordinated (C−C4−C).

average values in the C3−C4−C3, C3−C4−C4, and C4−C4−C4 cases, which are around the tetrahedral angle. Clear differences are observed for sp^2 configurations. C4−C3−C4 angles have much less average values than the others. The latter average bond angles are close to 120°. It means that threefold coordinated central atoms with at least two C3 first neighbors are always near planar structures even if the third one is C4. We have not investigated dihedral angle distribution because it is not so characteristic at a−C than at amorphous silicon or germanium.

Ring statistics

In our analysis the definition of the ring is a closed path, which starts from a given atom walking only on the first neighbor bonds. Every atom is visited only once. The size of the ring is the number of atoms forming the closed path. The ring statistics for our models are displayed in Table 2.4. A fourfold ring was found in the sample made with $E_{beam} = 1$ eV at $T_{sub} = 100$ K substrate temperature but there was no threefold ring in our simulation. In the graphitic and diamond network, sixfold, eightfold, etc. rings are present. In our models even-numbered as well as odd-membered rings can be found. It seems to be clear from the Table 2.4 that lower beam energy results in less 4−7 membered rings than at a higher bombarding energy.

Table 2.3: The average values of partial bond angle distributions and deviations.

Model	C−C3−C							
	CC_3C	σ	$C_3C_3C_3$	σ	$C_3C_3C_4$	σ	$C_4C_3C_4$	σ
e1T100	118.1	9.8	118.3	9.6	118.3	10.2	113.5	7.3
	118.1	9.5	118.3	9.3	118.3	10.1	113.5	7.3
e5T100	118.0	10.5	117.7	11.1	119.9	9.9	110.8	8.0
	118.0	10.5	117.7	11.1	119.9	9.9	110.8	8.0
e1T300	118.3	9.5	119.4	9.4	116.4	9.0	113.9	11.1
	118.3	9.6	119.3	9.6	116.4	9.0	113.9	11.1
e5T300	118.1	10.0	119.5	9.3	118.0	10.4	109.9	7.3
	118.2	9.4	119.3	8.9	117.8	10.2	110.0	7.1
e1T100l	118.6	9.4	119.1	9.2	118.1	9.9	114.9	9.9
	118.6	9.4	119.0	9.2	118.1	9.9	114.9	9.9
e5T100l	117.9	10.4	120.2	10.3	115.9	9.1	112.7	14.7
	117.8	10.2	119.5	10.2	115.7	9.1	112.7	14.7

Model	C−C4−C							
	CC_4C	σ	$C_3C_4C_3$	σ	$C_3C_4C_4$	σ	$C_4C_4C_4$	σ
e1T100	108.9	11.1	107.1	8.8	110.2	11.2	108.1	11.1
	108.9	11.1	107.1	8.8	110.2	11.2	108.1	11.1
e5T100	109.1	9.7	110.6	9.8	110.3	10.7	108.1	8.8
	109.1	9.7	110.6	9.8	110.3	10.7	108.1	8.8
e1T300	109.2	9.7	109.2	11.4	108.3	9.2	111.1	9.1
	109.2	9.7	109.2	11.4	108.3	9.2	111.1	9.1
e5T300	109.0	10.0	108.8	9.5	109.3	10.6	108.9	9.4
	109.1	9.8	109.0	9.3	109.1	10.4	108.8	9.3
e1T100l	109.0	10.6	107.8	10.3	110.3	10.9	107.9	10.6
	109.0	10.6	107.8	10.3	110.3	10.9	107.9	10.6
e5T100l	109.1	9.8	105.9	11.5	111.3	9.9	108.3	9.3
	109.1	9.8	106.2	11.7	111.3	9.9	108.3	9.3

Table 2.4: The average values of partial bond angle distributions and deviations.

Model	C−C−C		Ring statistics			
	C−C−C	σ	4	5	6	7
e1T100	112.8	11.5				
	113.5	12.2	1	21	40	37
e5T100	113.3	11.4				
	113.6	12.1	0	26	43	42
e1T300	115.3	11.3				
	115.6	11.7	0	25	21	17
e5T300	113.8	10.9				
	115.2	12.2	0	18	32	20
e1T100l	114.1	11.2				
	114.6	12.1	1	31	50	40
e5T100l	112.6	10.9				
	113.0	11.2	0	44	54	58

2.2.6 Summary

In summary, low energy molecular dynamics simulations of atomic beam growth on a diamond [111] surface were carried out using two different average carbon beam energies E_{beam} = 1 and 5 eV and two different substrate temperatures T_{sub} = 100 and 300 K during 30 ps. To obtain larger structures the simulations were prolonged by 15 ps at T_{sub} = 100 K. Six networks were prepared by atom deposition with periodic boundary conditions in two dimensions and the most important structural parameters were compared. Our aim was to construct large scale amorphous carbon models of over 100 atoms by quantum-mechanical treatment. The atomic interactions were described by a well-tested tight-binding potential. The structures were grown by atom-by-atom deposition onto substrates. The growing process was described as in real experiments without any artificial model of energy dissipation [kau92, koh00], however, the deposition rate was much higher than is usually applied in experiments. Other studies on the growth process use similar rates. On the basis of our time development investigation we expect that much lower deposition rates do not cause a significant difference in our models. The influence of our lower substrate temperature is that the energy dissipation is faster and this slightly compensates for the high deposition rate. Unfortunately, it is clear that real experimental rates cannot be implemented in computer simulation in the near future, even if less time-consuming classical empirical potentials are employed.

Bibliography

[all90] M.P. Allen and D.J. Tildesley, *Computer Simulation of Liquids* (Oxford Science Publications, Oxford, 1990).

[bar96] G.T. Barkema, N. Mousseau, Phys. Rev. Lett. **77**, 4358 (1996).

[bre90] D.W. Brenner, Phys. Rev. B **42**, 9458 (1990), Phys. Rev. B **46**, 1948 (1992).

[car85] R. Car and M. Parrinello, Phys. Rev. Lett. **55**, 2471 (1985).

[chu99] Chu-Chun Fu and M. Weissmann, Phys. Rev. B **60**, 2762 (1999).

[dav93] C.A. Davis, Thin Solid Films **226**, 30 (1993).

[don98] J. Dong and D.A. Drabold, Phys. Rev. B **57**, 15591 (1998).

[dra91] D.A. Drabold, R. Wang, S. Klemm, O.F. Sankey, and J.D. Dow, Phys. Rev. B **43**, 5132 (1991).

[dra94] D.A. Drabold, P.A. Fedders and P. Stumm, Phys. Rev. B **49**, 16415 (1994).

[dra94] D.A. Drabold, P. Stumm, P.A. Fedders, Phys. Rev. Lett. **72**, 2666 (1994).

[els98] M. Elstner, D. Porezag, G. Jungnickel, J. Elsner, M. Haugk, Th. Frauenheim, S. Suhai, and G. Seifert, Phys. Rev. B **58**, 7260 (1998).

[fra00] Th. Frauenheim, G. Seifert, M. Elsterner, Z. Hajnal, G. Jungnickel, D. Porezag, S. Suhai, R. Scholz, phys. stat. sol.(b) **217**, 41 (2000).

[gal89] G. Galli, R.M. Martin, R. Car, M. Parrinello, Phys. Rev. Lett. **62**, 555 (1989).

[gas91] P.H. Gaskell, A. Saeed, P. Chieux, and D. R. McKenzie, Phys. Rev. Lett. **67**, 1286 (1991).

[gil95] K. W. R. Gilkes, P. H. Gaskell, and J. Robertson, Phys. Rev. B **51**, 12303 (1995).

[jäg00] H.U. Jäger, K. Albe, J. Appl. Phys. **88**, 1129 (2000).

[jun94] G. Jungnickel, T. Frauenheim, D. Porezag, P. Blaudeck, U. Stephan, and R. J. Newport, Phys. Rev. B **50**, 6709 (1994).

[kak60] J. Kakinoki, K. Katada, T. Hanawa, and T. Ino, Acta Cryst. **13**, 171 (1960).

[kau92] H.-P. Kaukonen and R.M. Nieminen, Phys. Rev. Lett. **68**, 620 (1992).

[kau00] H.-P. Kaukonen and R.M. Nieminen, Phys. Rev. B **61**, 2806 (2000).

[kel93] P.C. Kelires, Phys. Rev. B **47**, 1829 (1993).

[koh98a] K. Koháry, S. Kugler, I. László J. Non-Cryst. Solids **227-230**, 594 (1998).

[koh98b] K. Koháry, Diploma Thesis, Budapest, 1998.

[koh00] K. Kohary, and S. Kugler, J. Non-Cryst. Solids **266-269**, 746 (2000).

[koh01] K. Kohary, and S. Kugler, Phys. Rev. B **63**, 193404 (2001).

[köh95] Th. Köhler, Th. Frauenheim, and G. Jungnickel, Phys. Rev. B **52**, 11837 (1995).

[kug93] S. Kugler, K. Shimakawa, T. Watanabe, K. Hayashi, I. László, and R. Bellissent, J. Non-Cryst. Solids **164-166**, 831 (1993).

[kug98] S. Kugler, K. Koháry and I. László: Proceedings of N2M Workshop, Grenoble, France, 1998. AIP Conference Proceedings 479. p64-69.

[kug99] S. Kugler, I. Laszlo, K. Kohary, K. Shimakawa, Functional Materials, **6**, 459 (1999).

[las98] I. László, Europhysics Letter **44**, 741 (1998); J. of Mol. Struct.: THEOCHEM **463**, 181 (1999).

[li90] F. Li. and J.S. Lannin, Phys. Rev. Lett. **65**, 1905 (1990).

[lif89] Y. Lifshitz, S.R. Kasi, and J.W. Rabalais, Phys. Rev. Lett. **62**, 1290 (1989).

[lif90] Y. Lifshitz, S.R. Kasi, and J.W. Rabalais, Phys. Rev. B **41**, 10468 (1990).

[mar96a] N.A. Marks, D.R. McKenzie, B.A. Pailthorpe, Phys. Rev. B **53**, 4117 (1996).

[mar96b] N.A. Marks, D.R. McKenzie, B.A. Pailthorpe, M. Bernasconi and M. Parrienello, Phys. Rev. B **54**, 9703 (1996).

[mcc00] D.G. McCulloch, D.R. McKenzie and C.M. Goringe, Phys. Rev. B **61**, 2349 (2000).

[mcg88] R.L. McGreevy and L. Pusztai, Molec. Sim. **1** 369 (1988).

[mil82] D.F.R. Mildner and J.M. Carpenter, J. Non-Cryst. Solids **47**, 381 (1982).

[mil00] W.I. Milne: "Preparation and structural properties of tetrahedrally bonded amorphous carbon"; in *Properties and Applications of Amorphous Materials*, Edited by M.F. Thorpe and L. Tichý, NATO Science Series II/9

[por95] D. Porezag, Th. Frauenheim, Th. Koehler, G. Seifert and R. Kaschner, Phys. Rev. B **51**, 12947 (1995).

[rap95] D.C. Rapaport, *The Art of Molecular Dynamics Simulation* (Cambrige University Press, Cambrige, 1995).

[rob93] J. Robertson, Diam. Rel. Mat. **2**, 984 (1993); **3**, 361 (1994).

[san89] O.F. Sankey and D.J. Niklewski, Phys. Rev. B **40**, 3979 (1989).

[shi91] K. Shimakawa, K. Hayashi, T. Kameyama. T. Watanabe, and K. Morigaki, Phil. Mag. Lett. **64**, 375 (1991).

[sla54] J.C. Slater and G.F. Koster, Phys. Rev. **94**, 1498 (1954).

[tan96] M.S. Tang, C.Z. Wang, C.T. Chan, and K.M. Ho, Phys. Rev. B **53**, 979 (1996).

[ter88] J. Tersoff, Phys. Rev. Lett. **61**, 2879 (1988).

[ter89] J. Tersoff, Phys. Rev. B **39**, 5566 (1989), Phys. Rev. B **41**, 3248 (1990).

[uhl98] S. Uhlmann, Th. Frauenheim, Y. Lifshitz, Phys. Rev. Lett. **81**, 641 (1998).

[wal98] J.K. Walters, K.W.R. Gilkes, J.D. Wicks and R.J. Newport, Phys. Rev. B **58**, 8267 (1998).

[wan89] C.Z. Wang, C.T. Chan and K.M. Ho, Phys. Rev. B **39**, 8586 (1989).

[wan93a] C.Z. Wang, K.M. Ho and C.T.Chan, Phys. Rev. Lett. **70**, 611 (1993).

[wan93b] C.Z. Wang, K.M. Ho, Phys. Rev. Lett. **71**, 1184 (1993).

[wan94] C.Z. Wang, K.M. Ho, Phys. Rev. Lett. **72**, 2667 (1994).

[xu92] C.H. Xu, C.Z. Wang, C.T. Chan and K.M. Ho, J. Phys. Condens. Matter **4**, 6047 (1992).

[zha92] B.L. Zhang, C.H. Xu, C.Z. Wang, C.T. Chan and K.M. Ho, Phys. Rev. B **46**, 7333 (1992).

Chapter 3

Atomistic simulation of the bombardment process during the BEN phase of diamond CVD

In this chapter the detailed examination of C_xH_y projectile bombardments onto hydrogenated amorphous carbon (a−C:H) is studied by means of computer simulations. This is the first work addressing these kind of processes with a reasonable quantum mechanical treatment. We investigated the conditions of hydrocarbon ion bombardments in an amorphous carbon layer. This involves the penetration depth study of different ion species by different bombarding energies. Special attention was paid to the critical energy needed for penetration and to the structural rearrangements in the amorphous carbon layer caused by the bombardment. We present here the first simulation with realistic conditions for bias enhanced nucleation microwave plasma assisted chemical vapor deposition of diamond used by Kátai *et al.* [kát99, kát00a, kát00b].

3.1 Introduction

3.1.1 The bias enhanced nucleation CVD growth of diamond

Chemical vapor deposition (CVD) techniques are frequently used to prepare different (hydrogenated) amorphous carbon films, as well as diamond layers. Bias enhanced nucleation (BEN) is used to achieve a higher nucleation density in the latter case. It can be assumed, that during the deposition, the different projectile ions and their kinetic energy with which they arrive at the surface, play an important role. The identification of the most abundant ionic species and the measurement of their energy distributions under typical microwave plasma enhanced CVD diamond nucleation conditions are still an important issue to be addressed if one attempts to validate any model of the nucleation process. Kátai *et al.* reported a detailed mass selective

energy analysis of the incoming ions during BEN nucleation of chemical vapor deposition of diamond [kát99, kát00a, kát00b]. They measured the different ion energies and fluxes as a function of bias voltage at 25 mbar and 800 °C. The total flux of hydrogen species (about 0.17×10^{16} $cm^{-2}s^{-1}$) was considerably less than for hydrocarbons (around 1.1×10^{16} $cm^{-2}s^{-1}$). At zero bias voltage ions have energies between 5 and 10 eV and the average ion energy increases for most species with increasing bias voltage in a linear way in the low bias regime. The overall ion flux, which is integrated over the energy distribution and summed for all ion species, increases with ascendant bias voltage almost exponentially. However, the fluxes of several species show a maximum versus bias voltage between 0 and 200 V. It was shown that about 85% of the total hydrocarbon flux is determined by C^+, CH^+, CH_2^+, CH_3^+, $C_2H_2^+$, $C_2H_3^+$ species, with average kinetic energies between 50 and 70 eV. The full width at half of the maximum energy distributions were between 20 and 30 eV. It was manifested that the lower limit for nucleation is around 100 V bias voltage, and the optimum is around 200 V. It was observed that among C_1H_y (y = 1, 2, 3) projectiles, the flux versus energy of CH_3^+ distribution is broader and shifted to lower energies with a total flux only marginally lower than those of CH_{0-2}^+. The $C_2H_2^+$ had the highest total flux of all hydrocarbon species. Finally, the above mentioned experiment supported the subplantation model proposed by Lifshitz *et al.* [lif89, lif90].

3.1.2 Proposed model for the formation of diamond nuclei in the BEN process

A speculative model to explain the formation of the heteroepitaxial alignment of diamond nuclei with the underlying substrate in the BEN process was proposed on the basis of results from *in situ* plasma analytical measurements, the results from surface analytical measurements and from literary data [kát00b]. Here we will give just a short summary of this model.

In the initial phase of BEN a polycrystalline β-SiC 3−4 nm thick layer is formed. It is epitaxially oriented with respect to the underlying silicon substrate. This silicon-carbon layer is not always observed in the experiments. However, from the point of view of the proposed model, its presence or absence is of no importance. In the next step of a typical BEN process, an amorphous carbon layer forms on the surface of this silicon-carbon layer. The thickness of the amorphous carbon layer is controlled by the balance between simultaneous growth and the etching of the hydrocarbon and the hydrogen species. The thickness of this layer was found to be around 5−8 Å.

The penetration depth of ions below the surface during the BEN process depends on their energy. Uhlmann *et al.* [uhl97, uhl98] executed molecular dynamics simulations to study the penetration of carbon atoms in diamond like amorphous carbon films, which are frequently referred to as tetrahedrally bonded amorphous

carbon (ta−C). It was shown for carbon atoms having kinetic energies bigger than 30 eV that the deposition is a subplantation process, where the carbon atom species penetrate and occupy subsurface positions. The penetration depth was found to be energy dependent. The results of these computer simulations permit the assumption that bombarding hydrocarbon ion species having a larger kinetic energy than 30−40 eV in BEN, penetrate 4−8 Å below the amorphous carbon surface. Consequently, hydrocarbon species penetrate into the vicinity of the epitaxially oriented silicon-carbon layer (or the silicon surface), but they do not damage its structure, as the amorphous carbon layer is sufficiently thin to give protection. However, a large fraction of hydrocarbon ions appears close to the interface of silicon-carbon and the a−C layer, increasing the local density in that region of the amorphous carbon layer.

Following this, the formation of diamond nuclei starts. The proposed model for the BEN process did not give a qualitative explanation of this mechanism, but two main points were emphasized. The diamond nucleation occurs close to the interface of SiC layer and a−C layer, and the silicon-carbon layer is protected from ion damage, thus it can provide orientation information. After the nuclei is formed, the kinetic energies for almost all of the ions are below the displacement energy of diamond (80 eV) and they do not damage the nuclei.

In this chapter, we concentrate on the incubation period of nucleation. We study the penetration characteristics of hydrocarbon ion species by means of computer simulations. For this, molecular dynamics simulations were performed by a reasonable quantum mechanical treatment. First, a realistic surface model of hydrogenated amorphous carbon (a−C:H) film is prepared. Then the bombardments of different hydrocarbon ions is studied by different energies. This involves the penetration depth study of different ion species by different bombarding energies. Special attention was paid to the critical energy needed for penetration and to the possible description of the formation of diamond nuclei. Finally, we present here the first simulation with realistic conditions for BEN as used in experiments.

3.2 Surface model of hydrogenated amorphous carbon

3.2.1 Generation of the surface model

The surface for our molecular dynamics (MD) simulations was generated from a hydrogenated amorphous carbon bulk supercell with an original density of 2.2 g/cm^3. This structure was prepared by long time annealing of randomly distributed 128 carbon and 69 hydrogen atoms [fra93, fra94, jun94]. The final arrangement of this model has 1.6%, 53.1%, 2.3% and 41.4% fraction of sp^1, sp^2, sp^{2+x} and sp^3 bonded carbon

atoms, respectively.[†] The average first neighbor coordination number is 2.88 in the cubic cell with an edge equal to 10.66 Å. For bond counting we used the value of 1.85 Å as an upper limit of bond length inside the first coordination shell. We followed previous works [don98, uhl98] to prepare a surface for C_xH_y ion bombardments. First, this structure was doubled in one direction, which we refer to as the z-axis. Then to model the surface, we broke the periodic continuation along the z direction to transform the periodically extended cube into an infinite slab with two free surfaces. One labeled as the "top" surface and the other as the "bottom" surface. We then cut the sample along the z-axis, 15 Å below the top layer, and the atoms below this were removed from the sample. In other words, we had a new bottom surface. Henceforth, it shall be referred to as the bottom surface. The cut of periodic continuation leads to dangling bonds on the surfaces. We chose the top surface as the target for bombardments. For the determination of the low energy structure of this film we undertook the following. The broken σ bonds at the bottom were saturated by hydrogen atoms to retain the electronic structure there. To achieve local rearrangement on the top surface (similar to the surface reconstruction in crystals), the sample was treated under an annealing process at 2000 K over about 1 ps, with time step Δt equal to 41 a.u. ($\approx$ 1.0 fs). This equilibrated structure was then subsequently cooled down to 30 K within about 1 ps. Then the sample relaxed with conjugent gradient method. Finally, this low energy structure was annealed at 1000 K for about 1 ps to prepare the substrate for C_xH_y projectile bombardment. Our purpose was to do simulations with realistic conditions for BEN experiments where the temperature is around 800 °C.

3.2.2 Properties of the model

The final structure of our surface a−C:H film contained 182 carbon and 107 hydrogen atoms, 16 of the latter replace the broken σ bonds at the bottom. We chose a 11.1 Å thick moveable part from the top, which contained 190 atoms. It is sufficient to model the bombardment experiments because the deepest penetration length is estimated to be around 10 Å for the projectiles having kinetic energy lower than 100 eV. The rest of the slab at the bottom, with a thickness 4 Å, were fixed in all simulations. The density of the sample was 1.98 g/cm^3. The bulk density was equal to ρ_{bulk} = 2.05 g/cm^3. We will refer to the bulk, as the structure 3 Å below the highest z coordinated atom and we will refer to the surface, as the structure above the bulk. We used periodic boundary conditions in plane, with the original cell size equal to 10.66 Å. The bonding arrangement contained 6.6%, 48.4%, 5.5% and 38.5% fraction of sp^1, sp^2, sp^{2+x} and sp^3 bonded carbon atoms, respectively. The mass profile in

[†]The introduction of sp^{2+x} hybrid denotes a carbon atom with a coordination equal to three, but the geometry of the bond having a similar structure to the sp^3 hybrid with one "dangling bond" in the fourth direction.

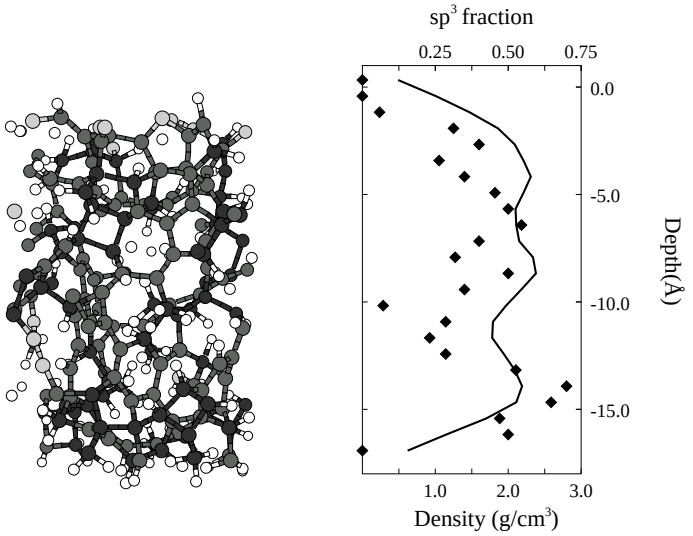

Figure 3.1: The substrate structure: sp^3 fraction, and mass density profile. The black atoms show carbon atoms with a coordination equal to four (Z = 4). Grey atoms have Z = 3, while light grey atoms have lower coordinations. The white circles show hydrogen atoms. The color version of the structure can be found at http://www.physik.uni−marburg.de/∼kohary/CxHybomb.html. The solid line in the figure on the right shows the density of the film and the filled diamonds show the sp^3 fraction.

Fig. 3.1 shows that there is not an important deviation from the average density, the minimum is about 1.8 g/cm^3 at 11 Å and the maximum is about 2.4 g/cm^3 at 8 Å below the surface.

In Fig. 3.2 the total and partial bond length distributions can be seen. The partial distributions are centered at 1.42, 1.54, 1.57 Å, for C3−C3, C3−C4 and C4−C4 respectively. (Ci−Cj means the distribution of distances between carbon atoms with coordination number i and j). The bond length distributions for the first neighbor distance show wide fluctuations around the crystalline graphite (1.42 Å) and diamond (1.54 Å) bond lengths.

3.3 C_xH_y projectile bombardments. The simulation details

In our work we aimed to study the ion bombardment in an sp^2-rich a−C:H structure by means of computer simulations [koh_sub]. We were interested *(a)* in the determination of average penetration depths, *(b)* in the examination into the possible decay of the projectiles, and *(c)* in the structural change of the target substrate. We studied the effects of the bombardment by different bombarding energies and atomic contents

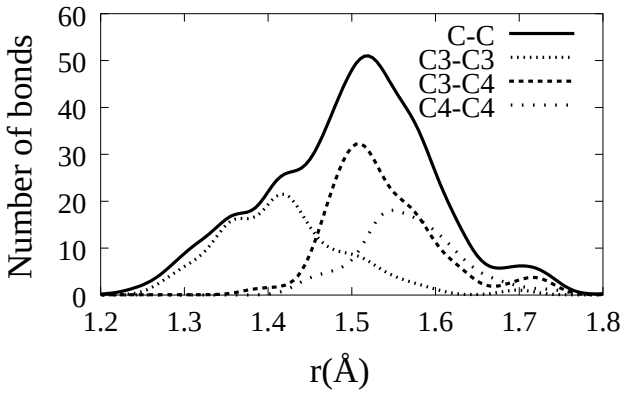

Figure 3.2: Total (C−C) and partial (Ci−Cj) bond length distribution for the substrate film. (The i and j denote the coordination of the carbon atoms.)

of projectiles. The experimental results showed that the most important ions during the bias enhanced nucleation (BEN) are C^+, CH^+, CH_2^+, CH_3^+, C_2H^+, $C_2H_2^+$ and $C_2H_3^+$ [kát99]. In fact, $C_2H_2^+$ has the highest total flux among hydrocarbon ions, with two or three times larger flux compared to any hydrocarbon and carbon ions.

We report here, the incubation period of the bias enhanced microwave plasma assisted CVD (BEN MW−CVD) phase of diamond nucleation growth. We studied the ion bombardment with two relevant projectiles: acetylene (C_2H_2) and methyl (CH_3). The interaction between the atoms was described by the density functional tight-binding (DFTB) method [els98, fra00], which was effective to describe the ground state geometries and physical properties of different carbon systems [köh95, fra95] and was also applied in the previous carbon bombardment simulations [uhl97, uhl98]. In the work of Uhlmann *et al.* the effect of neutral carbon atoms on a−C substrate was studied [uhl98]. However, in those simulations the conditions were different to ours. They simulated the carbon atom bombardment which resulted in creating a diamond like amorphous carbon (DLC or ta−C), which has a high percentage of sp^3 carbon atoms (even near to 100%). We were however interested in finding a realistic simulation for BEN MW−CVD nucleation of diamond and checking the validity of the model for the description of heteroepitaxial alignment for diamond nuclei in the BEN process, as proposed by Kátai *et al.* [kát00b].

The simulation details are the following. In the first *collision stage*, which describes the penetration and the energy loss of the species, a projectile with given kinetic energy was directed towards the substrate. Random numbers were used for determination of the coordinates of the mass center and for the local configurations of the species. The lowest atom of the projectile was placed consistently 4 Å over the substrate, where the interatomic potential almost vanishes. Simulations with three different kinetic energies were done (20, 40 and 80 eV) for C_2H_2 and with 20 and

40 eV for CH_3 to study the energy dependences of ion bombardment. The choice of these two projectiles and the kinetic energies were governed by experimental results [kát99, kát00a, kát00b]. The $C_2H_2^+$ projectile has the largest flux among hydrocarbon species. It can be predicted from previous single carbon projectile bombardments that 30−40 eV kinetic energy will be the critical energy for penetration of different ion species under the surface. We have chosen 20, 40 and 80 eV kinetic energies according to the above assumptions. The 20 eV energy bombardment describes the effects of low energy projectiles, whose energy is much lower than the energy needed for nucleation processes. The nucleation starts at 100 V bias voltage. The C_2H_2 projectiles have approximately 40 eV and CH_3 ion species have around 35 eV kinetic energy in this case. At 200 V bias, at the optimal voltage for nucleation, the CH_3 projectiles still have kinetic energy around 40 eV, but the C_2H_2 ions species, which possess the highest flux amongst all hydrocarbon ions, have kinetic energy close to 80 eV [kát99]. This energy is the displacement energy in diamond as well. From $C_1H_y^+$ projectiles CH_3 was chosen because its flux is just slightly lower than those of $C_1H_{0-2}^+$. Furthermore, $C_1H_y^+$ projectiles with low hydrogen content ($y \leq 2$) will warrant similar effects to single carbon bombardment, which was simulated earlier, but at different conditions [uhl98]. The collision stage was simulated for 7500 a.u. ($\approx$ 182 fs). During this period the kinetic energy of the substrate was rescaled according to 1000 K by a velocity rescaling method which simulates the constant temperature in the sample. For the different kinetic energy ion implantations, different time steps were used: Δt equal to 15, 10 and 5 a.u., for E_{kin} = 20, 40 and 80 eV, respectively. We studied four independent orientations of the bombarding species as it is shown in Fig. 3.3. The first orientation of C_2H_2 is called POINT, as the top view shows the projectile as a point. The second orientation of C_2H_2 is called LINE. In the case of CH_3 projectile, two different orientations were called PLANE and EDGE, according their orientation towards the surface at the start of the bombardments. The reason for choosing these orientations is because they are the extreme cases. In experiments projectile orientations are a mixture of these extremes. In Fig. 3.4 the time dependence of the kinetic energy of the POINT projectile starting with 80 eV can be seen. The carbon atoms have approximately 37 eV kinetic energy, which decreases to 1−5 eV after 400 MD steps, when the species arrives to the maximal penetration depth in the film. The time step for this case was 5 a.u. ($\approx$ 0.125 fs). The hydrogen atoms already have low kinetic energy at the start (t = 0).

In the second *thermalization stage*, the local structure relaxes and the ion energy dissipates into the lattice. The projectile atoms become part of the substrate, their velocities were also rescaled according to the substrate temperature (1000 K) for approximately 0.5 ps (Δt $\approx$ 0.5 fs). The trajectories of the next projectile were started over this final substrate. In summary, ten different projectiles were started over the initial substrate for all different orientations and energies. We note here that

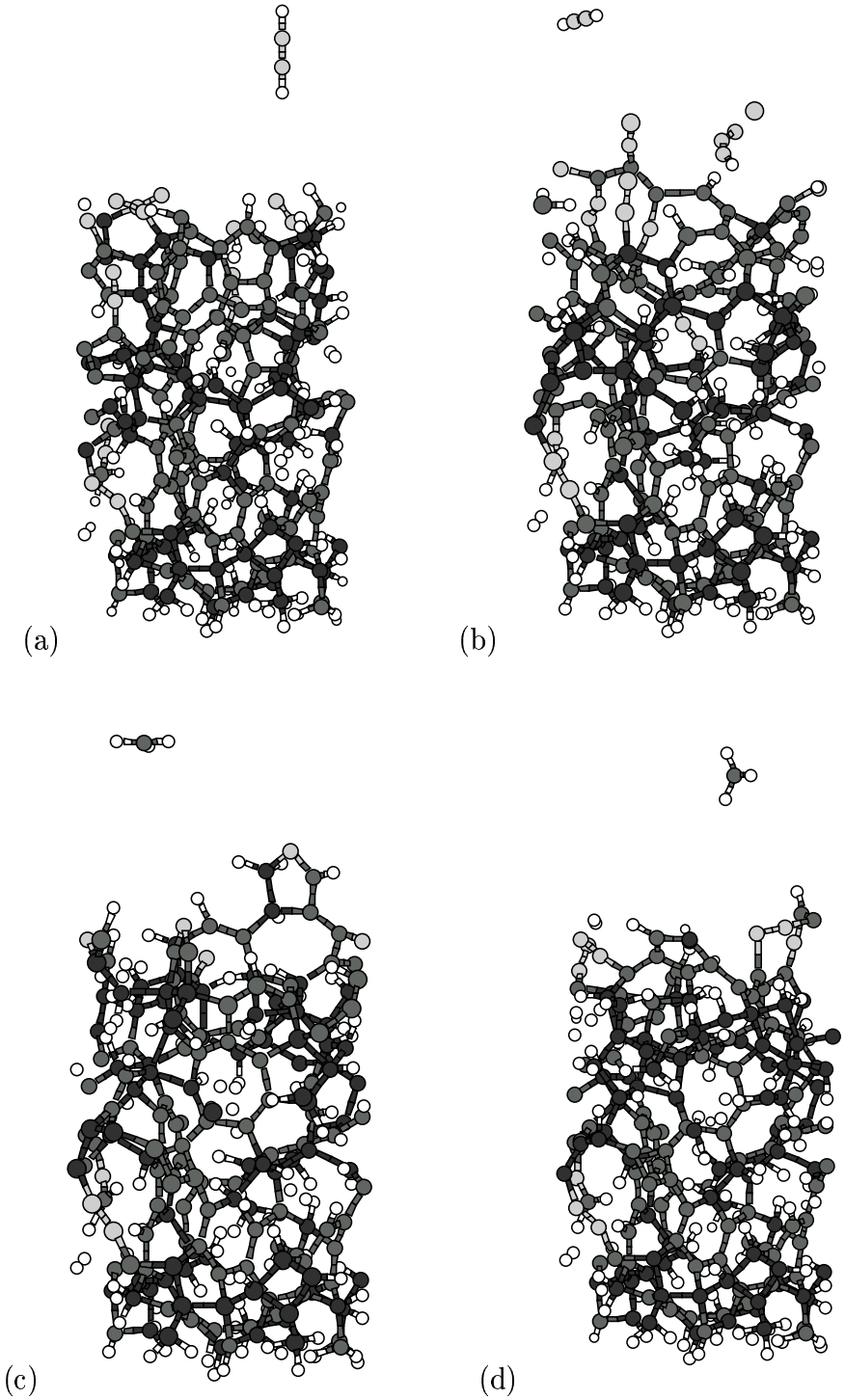

Figure 3.3: The four different projectile orientations. The names are (a) POINT, (b) LINE, (c) PLANE, (d) EDGE. We used the same coordination scheme as in Fig. 3.1. For a color version see: http://www.physik.uni−marburg.de/∼kohary/CxHybomb.html

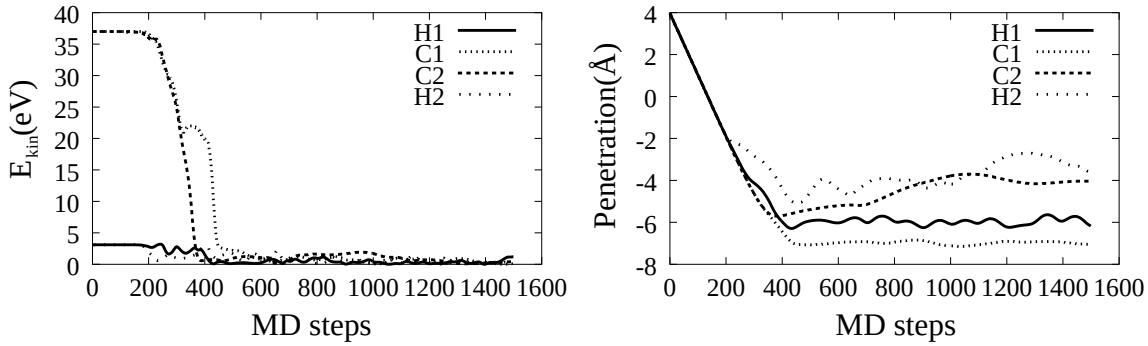

Figure 3.4: In the figure on the left, the kinetic energy versus time for the LINE projectile starting with 80 eV kinetic energy is shown. The carbon atoms have initially approximately 37 eV kinetic energy, while hydrogens have much lower energy. One MD step is equal to 5 a.u. in this case. In the figure on the right, the penetration of the atoms of the projectile is shown. The surface of the film is at 0 Å.

some projectile atoms were scattered back and some hydrogen atoms were jostled out from the film as well. In Fig. 3.3 we demonstrate projectiles over the final (i.e. after ten bombarding events) structures for EDGE40, PLANE40, LINE80 and POINT80. The central processing unit (CPU) time for the simulations was 12−15 weeks on HP ALPHA workstations.

3.4 Results

3.4.1 Dissociation of the projectiles

One of the main interests of our computer experiments was the time evolution study of the species. Monitoring the trajectories of the projectiles showed that their dissociations are the function of their kinetic energy (see Table 3.1). For acetylene the carbon-carbon bond was almost never broken at low energies (20, 40 eV). That bond was dissociated only twice for LINE orientation at 40 eV. At large bombarding energies (80 eV), the carbon-carbon bond was broken nine times for LINE orientation and only five times for POINT orientation. Yet, in the experiments the C_2H_2 projectiles have random orientations when they arrive at the substrate surface. This implies the fact that at high energies (around 80 eV) the carbon-carbon bond in C_2H_2 is broken between 50 and 90%. The number of broken hydrogen-carbon bonds in the projectiles increased with the bombarding energy. One can estimate from Table 3.1 that more than 60% of these kinds of bonds are broken in the experiments. It was also evident from the simulations, that after the dissociation, the hydrogen atoms like to form H_2 molecules, particularly in the case of CH_3. The final configurations of the projectile carbon atoms in the film can be seen in Table 3.2. They mostly have sp^{1+x} and sp^2

Table 3.1: The number of broken bonds during the implantation of the projectiles. H1 (C1) is the deepest hydrogen (carbon) atom in C_2H_2 species (POINT orientation). H1, H2, H3 are the three hydrogen atoms in the CH_3 projectile.

C_2H_2	E(eV)	H1−C1	C1−C2	C2−H2
LINE	20	3	0	3
	40	6	2	8
	80	8	9	8
POINT	20	1	0	3
	40	6	0	8
	80	9	5	10

CH_3	E(eV)	C−H1	C−H2	C−H3
EDGE	20	1	7	5
	40	8	9	9
PLANE	20	7	3	5
	40	7	7	8

hybrids. For methyl species, usually one hydrogen atom stays in a bond with the carbon atom. Also, for acetylene, for lower energy bombardment (20 and 40 eV) the hydrogen atoms stay bonded with the projectile carbon atom. We conclude from the data that when all the bonds are broken in the projectile during the collision phase, i.e. when the carbon atoms become naked, they have a lower coordination number in contrast to projectile carbon atoms, when not all the bonds are broken.

3.4.2 Penetration of the projectiles

It is important to study the penetration of the projectile atoms to retrieve information about processes during nucleations. In our computer simulations 10 Å was found to be the deepest penetration length in the sample under the surface. This demonstrates that our choice of 11 Å as the moveable part of the film was reasonable. The average of the maximum penetration depths are orientation, energy and projectile dependent. Table 3.3 shows that higher energy provides a deeper penetration depth. There is a significant difference between the implantation depth for POINT and LINE projectiles, if the average final penetration depth is considered. This distance hardly changes for the orientation LINE increasing the subplantation energy from 20 to 40 eV. However, in the same conditions, there are significant changes for POINT orientation. We declare here, that orientation has a decisive role in the penetration behavior of the projectiles, however, in experiments the species arrive with random orientations to the surface.

Table 3.2: The final orientations of the projectile carbon atoms in the films. C1 (C2) is the deeper (higher) carbon atom in C_2H_2 species (POINT orientation).

	LINE						PLANE	
	20 eV		40 eV		80 eV		20 eV	40 eV
	C1	C2	C1	C2	C1	C2	C	C
sp^0	2	2	1	2	3	3	3	1
sp^1	2	1	1		2	3		1
sp^{1+x}		1	3	1	2	2	1	3
sp^2	3	2	3	4	3	2	1	3
sp^{2+x}			1	1			1	
sp^3	3	4	1	2			4	2

	POINT						EDGE	
	20 eV		40 eV		80 eV		20 eV	40 eV
	C1	C2	C1	C2	C1	C2	C	C
sp^0	1	1	2	3	1	1		2
sp^1	2	2	2	2	1			2
sp^{1+x}	4	3	3	2	2	5	5	1
sp^2	3	4	3	3	3	2	2	3
sp^{2+x}						1	2	1
sp^3					2	1	1	1

Table 3.3: The average maximal penetration depths for the projectile carbon atoms. The average final penetration depths can be seen in the brackets. For the latter case only projectile atoms under the original surface were considered.

C_2H_2	E(eV)	C1(Å)	C2(Å)	Mass Center(Å)
LINE	20	-2.40 (-1.31)	-2.64 (-1.48)	-2.38 (-1.41)
	40	-2.83 (-2.17)	-2.73 (-1.98)	-2.50 (-2.05)
	80	-5.83 (-5.52)	-4.71 (-4.96)	-4.83 (-3.98)
POINT	20	-2.71 (-1.77)	-2.81 (-2.31)	-2.61 (-2.02)
	40	-4.76 (-4.80)	-4.89 (-4.61)	-4.51 (-4.32)
	80	-6.24 (-6.09)	-5.80 (-4.59)	-5.59 (-4.73)

CH_3	E(eV)	C(Å)	Mass Center(Å)
EDGE	20	-2.84 (-2.07)	-2.74 (-2.13)
	40	-3.93 (-2.93)	-3.30 (-2.02)
PLANE	20	-2.74 (-1.83)	-2.45 (-1.59)
	40	-3.43 (-3.19)	-2.84 (-2.17)

We now turn to the question which was raised by the proposed model for the description of diamond nuclei growth in the BEN process [kát00b]. In that model it was assumed that the hydrocarbon ion species having kinetic energies bigger than 30−40 eV, penetrate under the amorphous carbon surface in the vicinity of the silicon-carbide layer. In the experiments, the thickness of the amorphous carbon layer was found to be around 5−8 Å, depending on the balance between simultaneous growth and the etching of hydrocarbon and hydrogen species. From Table 3.3 it can be asserted that for low energy bombardments (with 20 eV), the penetration of the projectile ions take place in surface regions. It seems reasonable to affirm that penetration in deeper regions starts at around 30−40 eV. For bigger kinetic energies (80 eV), the penetration depths of the projectiles are close to 4−8 Å, i.e. in the vicinity of the silicon-carbon substrate in the experiments.

3.4.3 Structural rearrangement

The bombardment of the projectile atoms cause structural rearrangements in the substrate and contribute to the formation of diamond nuclei. In the model describing the bias enhanced microwave plasma assisted CVD of diamond nuclei, the formation of diamond nuclei was not explained because it was beyond of scope of that model [kát00b]. It is assumed in the model that the presence of silicon-carbon or silicon substrate contribute to the formation of diamond nuclei, as it has orientation information. It is beyond the work of our computer simulation to report on this process

here, due to the fact that we did not have a silicon substrate. In this section we will give a possible explanation of the initial process into the formation of diamond nuclei, which involves the occurrence of increasing fraction of sp^3 atoms in deeper regions after the bombardments.

Taking into consideration the changes in the total film, our results show that the thickness of films have grown by 1−3 Å in z direction after ten subsequent bombardments for all different cases. The sp^3 content in the films increased with 1−5%, while the sp^2 content decreased by the same magnitude. There are no significant changes in the total density of the films and on average partial first neighbor distances.

Here, we concentrate on the changes in the different depths of the film. It was reported in a similar study by Uhlmann *et al.* [uhl98] that the carbon bombardments form an sp^2 rich defective surface layer, whose thickness scales with ion energy. Below that layer an sp^3 rich layer was found. This was one of the main results in their study, which supports the subplantation model in the physical vapor deposition method of diamond like amorphous carbon films. Nevertheless, the conditions in the BEN process are different. The temperature is around 1000 K compared to the typically low temperature (T $<$ 150 K) usually applied during the preparation of diamond-like carbon. Furthermore, the plasma contains several different hydrocarbon species in BEN, contrary to diamond-like carbon growth, where single monoenergetic particles (mostly single carbon ions) are used. However, our computer simulations of bombardments with C_2H_2 and CH_3 projectiles show similar conclusions to the work of Uhlmann *et al.* [uhl98]. In Fig. 3.5 the mass density difference and the discrepancy in the sp^2, sp^3 fraction for the final and initial films can be seen for all cases. Structural rearrangements even for low bombarding energy with 20 eV can be seen. The main contribution is close to the surface in the region between -4.0 Å and -2.0 Å, measured from the top of the initial substrate. The sp^3 content increases with 20−30% and the sp^2 content decreases by the same magnitude after ten bombardment events. For 40 eV the changes are significant at the deeper region between -6.0 Å and -3.0 Å. The change in the sp^2 and sp^3 content is broader compared to the change at 20 eV. At 80 eV, for C_2H_2 projectile bombardment, the penetration regime moves deeper and can be found between -10.0 Å and -5.0 Å. In all cases the structural rearrangement occurs together with the mass density changes. The effect is the largest at 80 eV. We note here that the mass density increase over the top of the initial surface comes from the slow growth of the top surface. Therefore, changes in Fig. 3.5 over 0 Å are irrelevant.

It is known from the experiments of Kátai *et al.* [kát99] that CH_3 projectiles have 40 eV kinetic energy at 200 V bias, whereas for, C_2H_2 it is 80 eV. Nevertheless, the kinetic energies of the carbon atoms in the projectiles are the same. It is around 37 eV for CH_3 ion species with 40 eV kinetic energy and approximately the same for C_2H_2 projectile. Yet the latter one has two carbon atoms in one projectile. If one

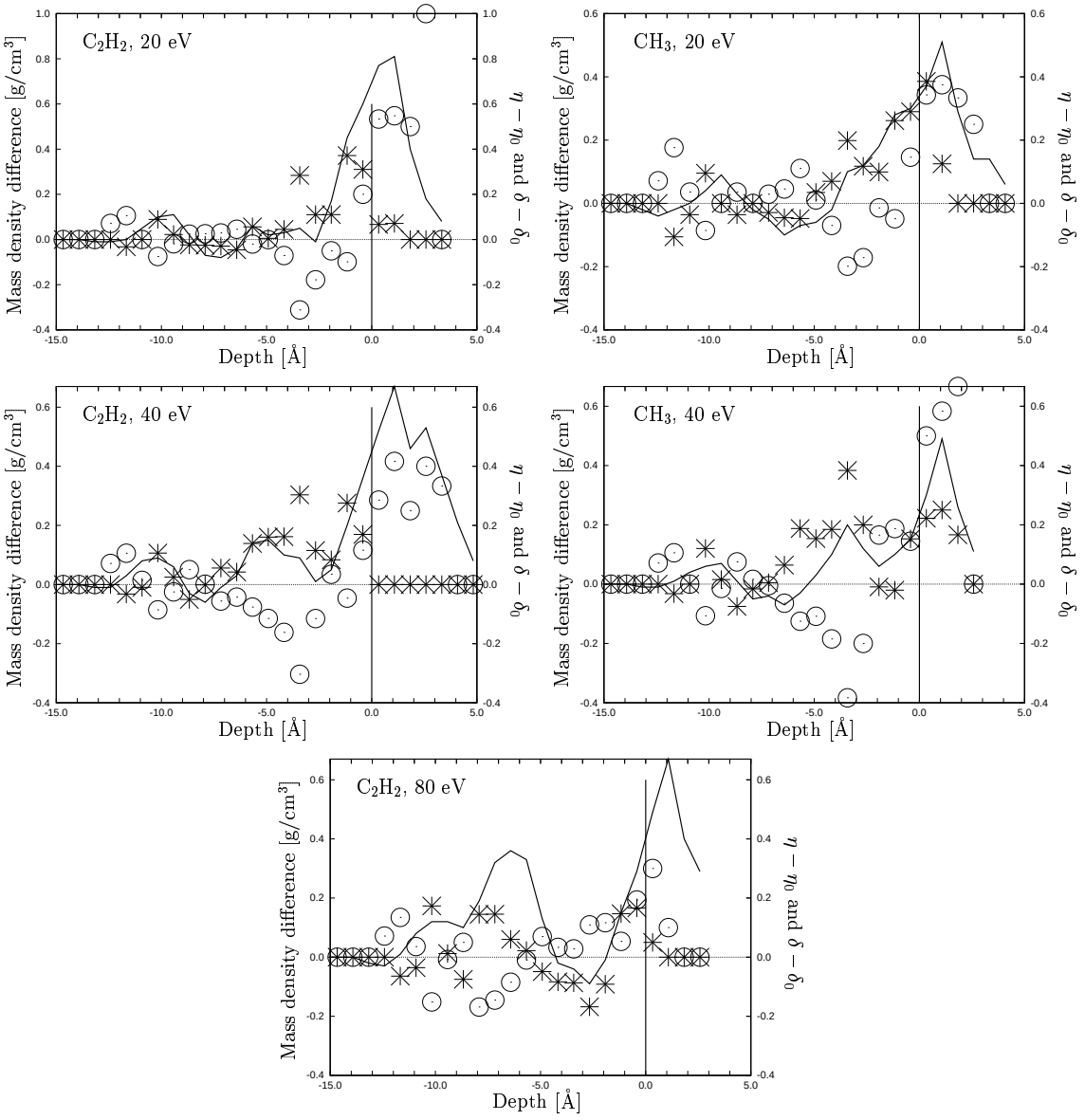

Figure 3.5: The depth profiles for amorphous carbon films after ten bombardment events. The solid line show the mass density difference profile between the final and the initial films. The circles and stars denote the sp^2 and sp^3 fraction differences, respectively ($\eta - \eta_0$ and $\delta - \delta_0$). The vertical straight lines show the original top of the initial film.

compares the effects of these two projectiles at the optimal bias voltage (200 V) for the nucleation process, considerable discrepancies are noticeable. The penetration of C_2H_2 projectiles occurs in deeper regions. In addition, the effects of caused structural rearrangements are different. The changes are in deeper regions for C_2H_2 ion species in contrast to CH_3 projectiles. We can state here that C_2H_2 projectiles which has the largest flux among the hydrocarbon species, strongly contributes to the local density increase and structural rearrangement in the 4−8 Å region under the surface. The increase of the content of sp^3 hybrids at the optimal 200 V bias voltage for diamond nucleation in the region 4−8 Å under the surface – which is the vicinity of silicon substrate and has orientation information in the experiments – can cause the possible formation of diamond nuclei in a "percolated way". This suspicion should be verified by computer simulation and it is our main goal in the future.

3.5 Summary

The structural rearrangements in a−C:H films were investigated under bombardments with C_xH_y projectiles. Special attention was paid to the study of different projectiles at different bombarding energies. Larger kinetic energies produce deeper subplantations and lead to a higher probability of the dissociation of the projectiles. For acetylene the carbon-carbon bond is hardly ever broken at low energies (20, 40 eV) and it is broken in 50−90% of cases for larger energies (80 eV). The computer experiments showed that around 60% of projectile hydrogen-carbon bonds are broken during the subplantation. Usually, one of the hydrogen-carbon bond are not broken for CH_3 and the other two hydrogens form H_2 molecules. At the typical 200 V bias voltage, which is optimal for diamond nuclei formation in BEN, the C_2H_2 projectiles have 80 eV and CH_3 ion species 40 eV kinetic energy. There are significant differences in their effects on the structural rearrangements in the films. For C_2H_2 projectiles, the penetration is deeper and these species cause changes in deeper regions, than for CH_3 projectiles. Whereas, the CH_3 projectiles do not contribute to the deep changes and cause structural rearrangements only in surface regions. The structural changes in the film showed that larger kinetic energy ionic species under the average deposition depth generate a thicker sp^3 rich film whilst the surface mostly consists of atoms with sp^2 hybrids. The border between these two regimes descend with larger deposition energies. The results support the subplantation model. It will definitely be a fascinating task in the future to do simulations over a silicon substrate and to study the effect of this crystalline layer on the formation of diamond nuclei in the amorphous film.

Bibliography

[don98] J. Dong and D.A. Drabold, Phys. Rev. B **57**, 15591 (1998).

[els98] M. Elstner, D. Porezag, G. Jungnickel, J. Elsner, M. Haugk, Th. Frauenheim, S. Suhai, and G. Seifert, Phys. Rev. B **58**, 7260 (1998).

[fra93] Th. Frauenheim, P. Blaudeck, U. Stephan and G. Jungnickel, Phys. Rev. B **48**, 4823 (1993).

[fra94] Th. Frauenheim, G. Jungnickel, U. Stephan, P. Blaudeck, and S. Deutschmann, M. Weiler, S. Sattel, K. Jung, and H. Erhardt, Phys. Rev. B **50**, 7940 (1994).

[fra95] Th. Frauenheim, G. Jungnickel, Th. Koehler and U. Stephan, J. Non-Cryst. Solids **182**, 186 (1995).

[fra00] Th. Frauenheim, G. Seifert, M. Elsterner, Z. Hajnal, G. Jungnickel, D. Porezag, S. Suhai, R. Scholz, phys. stat. sol.(b) **217**, 41 (2000).

[jun94] G. Jungnickel, T. Frauenheim, D. Porezag, P. Blaudeck, U. Stephan, and R. J. Newport, Phys. Rev. B **50**, 6709 (1994).

[kát99] Sz. Kátai, Z. Tass, Gy. Hárs and P. Deák, J. Appl. Phys. **86**, 5549 (1999).

[kát00a] Sz. Kátai, A. Kováts, I. Maros and P. Deák, Diam. Relat. Mat. **9**, 317 (2000).

[kát00b] Sz. Kátai, PhD Thesis, München, 2000.

[koh_sub] K. Kohary, S. Kugler, Z. Hajnal, Th. Köhler, Th. Frauenheim, Sz. Kátai, and P. Deák, (submitted).

[köh95] Th. Köhler, Th. Frauenheim, and G. Jungnickel, Phys. Rev. B **52**, 11837 (1995).

[lif89] Y. Lifshitz, S.R. Kasi, and J.W. Rabalais, Phys. Rev. Lett. **62**, 1290 (1989).

[lif90] Y. Lifshitz, S.R. Kasi, and J.W. Rabalais, Phys. Rev. B **41**, 10468 (1990).

[por95] D. Porezag, Th. Frauenheim, Th. Koehler, G. Seifert and R. Kaschner, Phys. Rev. B **51**, 12947 (1995).

[uhl97] S. Uhlmann, dissertation, Technische Universität Chemnitz, 1997, http://archiv.tu-chemnitz.de/pub/1997/0031/

[uhl98] S. Uhlmann, Th. Frauenheim, Y. Lifshitz, Phys. Rev. Lett. **81**, 641 (1998).

Chapter 4

Growth of amorphous silicon. Low energy molecular dynamics simulation of atomic bombardment

In this chapter the growth of amorphous silicon thin films was studied using the tight-binding molecular dynamics technique. The atomic deposition program code, which had been developed for studying the growth of amorphous carbon structures and which was reported in chapter 2, was applied.

4.1 Introduction

Amorphous silicon (a−Si) has been the subject of numerous experimental and theoretical works in recent decades [mor99]. Several diffraction measurements were employed on a−Si samples in order to retrieve information about the atomic arrangement [moss70, bar77, for89, kug89, cic90, kug93], i.e. the radial distribution function (RDF), which contains integrated information about the amorphous structures. The results of these experiments suggest that the covalently bonded amorphous silicon are not completely disordered. The bonds between atoms and the coordination numbers are very similar to the crystalline phase. First and second neighbor peaks are broadened, but the positions are the same as in the crystalline structure, while the third peak disappears in the measured RDF. The absence of the third peak confirms that there is no characteristic dihedral angle.

In 1985, a continuous random network model of amorphous silicon (WWW model) was constructed by Wooten *et al.* [woo85] who carried out Monte Carlo (MC) simulations using the classical empirical potential of Keating [kea66]. This defect-free network includes fivefold and sevenfold rings in addition to the sixfold rings of the diamond structure. Since then, several computer generated models have been constructed using classical empirical potentials [kel88, lue89, ish97] or applying different

quantum mechanical methods [sti91, tót94, hen96, her00], but still the WWW model is considered to be the best three-dimensional atomic scale representation of the amorphous silicon network. Dangling bonds or even floating bonds (if they exist) are believed to be very rare in this condensed phase of silicon atoms and are not included in the WWW model. Recently, an accurate X−ray diffraction measurement [laa99] was published in the wide Q range of 0.03−55 $Å^{-1}$. The most important conclusion of this measurement, apart from confirming earlier results, is that the coordination number is less than four in implanted a−Si sample, which is controversial with the WWW model of amorphous silicon.

An alternative to MC simulations is molecular dynamics (MD). On the basis of the Car–Parrinello density functional theory (DFT) method, MD structural simulation was carried out for a−Si having 54 atoms [sti91]. Larger systems are needed for investigating complex dynamics processes, such as, for example those involved in growth. A frequently applied method is to find convenient tight-binding (TB) models, which could be employed over a hundred atoms and could be less time consuming than DFT. In our simulations the TB Hamiltonian of Kwon *et al.* [kwo94] was applied to describe the interaction between silicon atoms. This group developed an excellent TB potential for carbon systems and we successfully applied it to the amorphous carbon growth [koh01]. All the parameters and functions of the interatomic potential for silicon were fitted to the results of local density functional calculations. This TB potential reproduces energies of different cluster structures, elastic constants, the formation energies of vacancies and interstitials in crystalline silicon. According to the authors' article, the only disadvantage of this TB model is that the bond lengths inside small clusters are a bit longer than those derived from *ab initio* calculations or from the experiments.

4.2 Simulation details

Rapid cooling of the liquid phase is frequently applied to construct amorphous and glassy structures [sti91, hen96, ish97, yan98]. The system is cooled down to room temperature at a rate of 10^{11} – 10^{16} K/s. Another possible approach for constructing an amorphous structure [kug_tbp] is motivated by the fact that amorphous silicon is usually grown by different vapor deposition techniques in laboratories. We have developed a MD computer code (see section 2.2.3) to simulate the real preparation procedure of an amorphous structure, which is grown by atom-by-atom deposition on a substrate. In our recent work [koh01], the growth of amorphous carbon films were simulated by this method. A brief summary of our simulation technique is described here (for details, see reference [koh01] or section 2.2.3). A rectangular diamond lattice cell containing 120 silicon atoms was employed to mimic the substrate. There were 16 fixed atoms at the bottom. The remaining atoms could move with full dynamics.

The simulation cell was open along the [111] direction (positive z-axis) and periodic boundary conditions were applied in planar x, y directions. The kinetic energy of the atoms in the substrate were rescaled at every time step ($\Delta t = 0.5$ fs) in order to keep the substrate at a constant temperature. First, the substrate was kept at a given temperature for 0.5 ps to enable structural relaxation. In the deposition process the frequency of the atomic injection was on average 1/125 fs^{-1}. This flux is orders of magnitude higher than the deposition rate commonly applied in experiments. However, the low substrate temperatures (100 and 300 K) during simulations cause quick energy dissipation and this may compensate the high deposition rate.

In our first set of simulations the initial kinetic energies of the atoms in the above case were dissipated by the interaction with surface atoms. To speed up the energy dissipation, we have developed a different simulation method as well. The velocities of the atoms in the atomic beam were modified by the following procedure. If a bombarding silicon atom arrived closer than the "*critical distance*" to any substrate atom, it became part of the "group" of substrate atoms. In other words, their total kinetic energy was rescaled in every time step to a given (substrate) temperature. If the next bombarding atom arrived in the neighborhood of any of the atoms in this group, the similar procedure was employed. The chosen critical distance was 15% larger than the bond length in crystalline silicon (2.36 Å). This is a simple model to speed up the inelastic collision between bombarding and target atoms and a plausible interpretation of the phenomena. Nine different structures have been constructed by the methods mentioned above:

(*i*) Six models constructed with 25 ps injection time, and with average kinetic energy E_{beam} = 1 eV and 5 eV, at T_{sub} = 100 K substrate temperature (e1T100R5, e5T100R5, e1T100R10, e5T100R10, e1T100R20, and e5T100R20). R5, R10, and R20 indicate different relaxation times (5, 10, and 20 ps, respectively) for both structures after 25 ps injection.

(*ii*) Three models (e1T300, e5T300, e10T300) were constructed at T_{sub} = 300 K substrate temperature using our model for quick energy dissipation. Average kinetic energies of bombarding atoms were E_{beam} = 1 eV, 5 eV, and 10 eV, respectively. The simulation time was 5 ps for these three models. Due to the preparation method the temperature of the films remained 300 K, therefore no relaxation was applied.

(*iii*) In order to retrieve information on the difference between rapid cooling [sti91, hen96, ish97] and atom-by-atom deposition on a substrate (melt-quenching and vapor-quenching), we prepared an additional, tenth model (e1T100Q; Q is for quenching) in the following way. The temperature of the film e1T100R20 was increased to 3500 K. Considering this, as an initial state, the trajectories of the silicon atoms were followed by full dynamics for 7.5 ps. The substrate temperature was kept at 100 K again, which leads to the cooling of the film above the substrate. After 7.5 ps, the temperature of the film decreased into the region at around 200 K. This technique can be considered

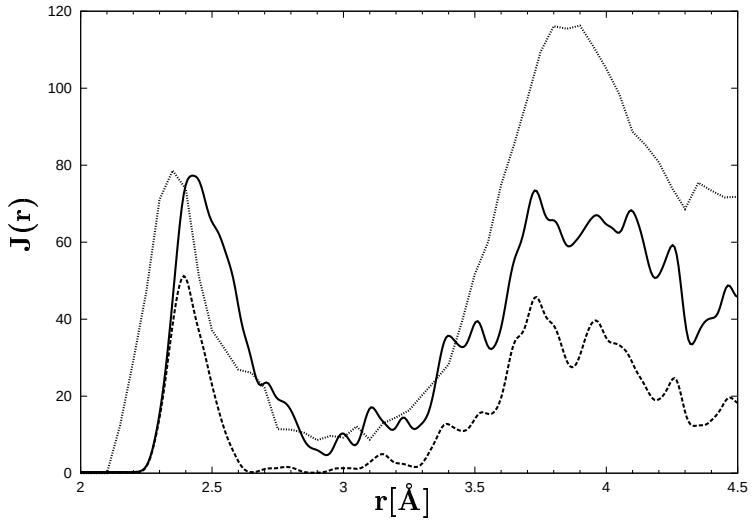

Figure 4.1: The first and second neighbor peaks in the radial distribution functions for e1T100Q model (solid line). The dotted line shows the experimental silicon RDF, reported in [kug93]. It is clear that there is not a determined distance, which can be considered as the border for the first neighbor shell, and the first and second neighbor peaks overlap. In addition, it can be seen that the model potential applied in these simulations overestimates the first neighbor distances. The dashed line represents the $J_{4,4}$ partial radial distribution function, which belongs to distances between Z = 4 coordinated silicon atoms, taking the first neighbor shell to 2.6 Å.

as the computer simulation of splat cooling, where small droplets of melt are brought into contact with the chill-block.

The main goal of our work was to simulate amorphous silicon structures.

4.3 Structural properties

The final structures of different models consist almost of the same number of atoms (between 162 and 177), with a thickness of about 13 Å (see Table 4.1). In Fig. 4.1 the first and second neighbor peaks are shown in e1T100Q model. Contrary to carbon systems (see section 2, fig. 2.9), there is not a clear, determined distance, which can be considered as a border for the first neighbor shell in case for a−Si. We have chosen 2.6, 2.7, 2.82 and 3.0 Å as a limit for the first neighbor shell to calculate the statistics of the models. Snapshots of films e1T100R20 and e1T100Q are shown in Fig. 4.2, taking the first neighbor shell to 2.6 Å. The substrates with T_{sub} = 100 K remained similar to crystal lattice.

Table 4.1: The tables below contain the number of silicon atoms (No.) in the films, in addition to the percentage of atoms with different coordination numbers (Z), the average coordination number $\langle Z \rangle$, the thickness z_d and the density ρ of the films. Two rows belong to bulk (top) and to total (lower) sample, respectively. The numbers in the top table (Table A) were calculated by taking the first neighbor shell to 2.6 Å, and in the bottom table (Table B) by taking 2.82 Å.

Table A (2.6 Å)	No.	Z=2	Z=3	Z=4	Z=5	Z=6	$\langle Z \rangle$	z_d(Å)	$\rho(g/cm^3)$
e1T100R5	140	7.1	10.7	70.0	7.1	0.0	3.7	10.1	2.5
	166	9.6	15.7	62.7	8.6	0.0	3.6	13.1	2.2
e1T100R10	134	3.0	14.9	67.9	12.7	0.7	3.9	9.8	2.4
	166	3.6	18.7	62.7	14.9	0.7	3.8	12.8	2.2
e1T100R20	134	3.0	12.7	71.6	10.4	1.5	3.9	9.8	2.4
	166	6.6	18.7	63.3	11.2	1.5	3.8	12.8	2.2
e5T100R5	151	7.9	23.8	51.7	10.6	0.0	3.5	10.6	2.3
	162	9.9	24.1	50.0	10.6	0.0	3.5	13.6	1.9
e5T100R10	152	5.9	23.0	50.0	20.4	0.7	3.9	10.7	2.3
	162	6.2	24.1	49.4	21.1	0.7	3.8	13.7	1.9
e5T100R20	152	4.6	18.4	51.3	23.0	2.0	4.0	10.7	2.3
	162	4.3	19.8	51.2	23.7	2.0	4.0	13.7	1.9
e1T300	151	7.9	16.6	53.6	15.2	2.6	3.8	10.8	2.4
	177	11.3	18.6	48.0	15.9	2.6	3.6	13.8	2.2
e5T300	135	6.7	19.3	47.4	20.0	3.0	3.9	9.4	2.8
	171	12.3	22.8	40.9	20.7	3.0	3.6	12.4	2.5
e10T300	142	7.0	19.7	52.1	19.7	0.7	3.9	9.7	2.7
	175	11.4	24.0	45.7	20.4	0.7	3.7	12.7	2.4
e1T100Q	122	1.6	13.9	74.6	8.2	0.0	3.9	9.1	2.4
	166	4.2	22.3	63.3	8.2	0.0	3.6	12.1	2.3

Table B (2.82 Å)	No.	Z=2	Z=3	Z=4	Z=5	Z=6	$\langle Z \rangle$	z_d(Å)	$\rho(g/cm^3)$
e1T100R5	140	0.0	0.7	55.0	31.4	11.4	4.6	10.1	2.5
	166	0.0	3.0	51.2	39.3	13.6	4.6	13.1	2.2
e1T100R10	134	0.0	1.5	53.0	29.9	11.9	4.6	9.8	2.4
	166	0.0	3.6	47.0	39.6	16.4	4.7	12.8	2.2
e1T100R20	134	0.0	1.5	53.7	28.4	15.7	4.6	9.8	2.4
	166	0.0	3.6	50.0	35.1	20.1	4.6	12.8	2.2
e5T100R5	151	0.0	6.0	31.8	43.7	15.9	4.8	10.6	2.3
	162	0.0	5.6	32.7	47.0	16.6	4.8	13.6	1.9
e5T100R10	152	0.0	2.6	34.9	40.1	15.8	4.9	10.7	2.3
	162	0.0	3.1	34.6	42.8	17.1	4.9	13.7	1.9
e5T100R20	152	0.0	2.6	35.5	43.4	15.8	4.8	10.7	2.3
	162	0.0	2.5	35.8	46.1	17.1	4.8	13.7	1.9
e1T300	151	0.0	3.3	32.5	40.4	21.9	4.9	10.8	2.4
	177	0.0	7.9	33.3	45.0	21.9	4.7	13.8	2.2
e5T300	135	0.0	0.7	27.4	39.3	23.7	5.2	9.4	2.8
	171	0.6	1.2	30.4	47.4	28.9	5.1	12.4	2.5
e10T300	142	0.0	0.7	28.2	45.8	19.7	5.0	9.7	2.7
	175	0.6	2.9	30.9	52.8	21.8	4.9	12.7	2.4
e1T100Q	122	0.0	0.8	56.6	28.7	12.3	4.6	9.1	2.4
	166	0.0	0.6	54.8	41.0	17.2	4.6	12.1	2.3

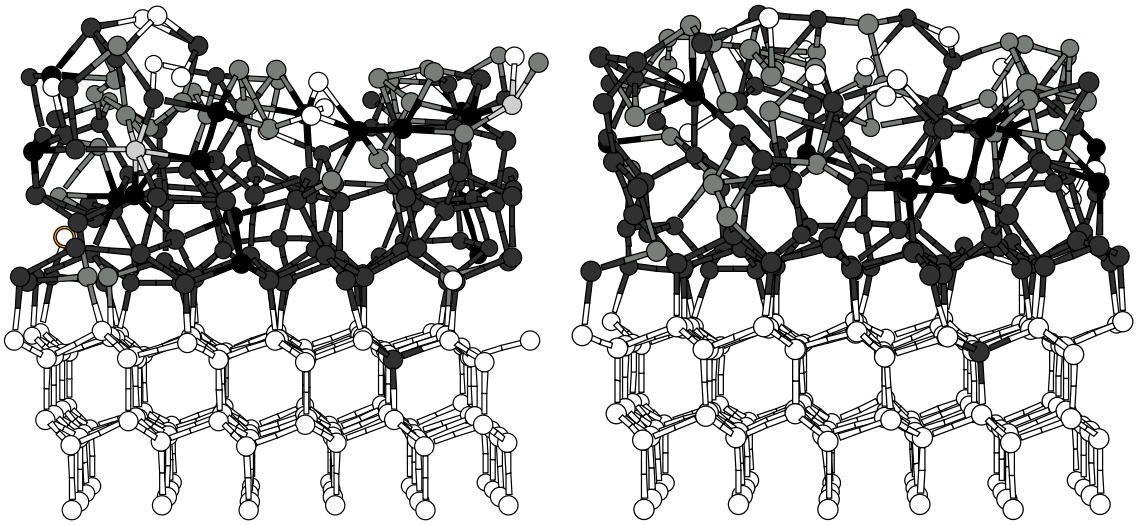

Figure 4.2: Snapshots of e1T100R20 (on the left side) and e1T100Q (on the right side) models are shown after growth and relaxation. The substrates (open circles at the bottom) with T_{sub} = 100 K remained similar to the crystal lattice during growth. Light grey, grey and black atoms are threefold, fourfold and fivefold-coordinated, respectively. The rest of the open circles correspond to twofold- and one one-fold coordinated atoms. For a color version see: http://www.physik.uni−marburg.de/∼kohary/aSifigures.html

4.3.1 Time development of relaxations

After the growth process, when there was no more injected bombarding atoms over the network, the films relaxed with full dynamics for 20 ps. The deposited networks, which have a temperature gradient in the z direction released a considerable amount of heat. This is attributable to the influence of the substrate kept at a constant temperature. Anomalous relaxation has been observed during quenching. Temperature versus time function of this non-equilibrium process shows a stretched-exponential form, $T_{film}(t) = c + \exp\left(at^{\beta} + b\right)$ K.

In the case of the e1T100Q model the fitting parameters are a = -0.46 (t is measured in fs) and b = 7.57 and c = 100 K (substrate temperature). The β is equal to 0.95 (< 1), producing stretched exponential relaxation. For the e1T100R20 model, if the fit is done in the [0:10] ps interval, we obtain similar fitting parameters; β = 0.88, a = -0.49, b = 7.54, and for e5T100R20 β = 1.00, a = -0.41, b = 7.79. The fits are shown in Fig. 4.3. We note here that the search for the best fit is not a well-defined problem in our case. A slight modification in the parameter list can give qualitatively almost the same fit.

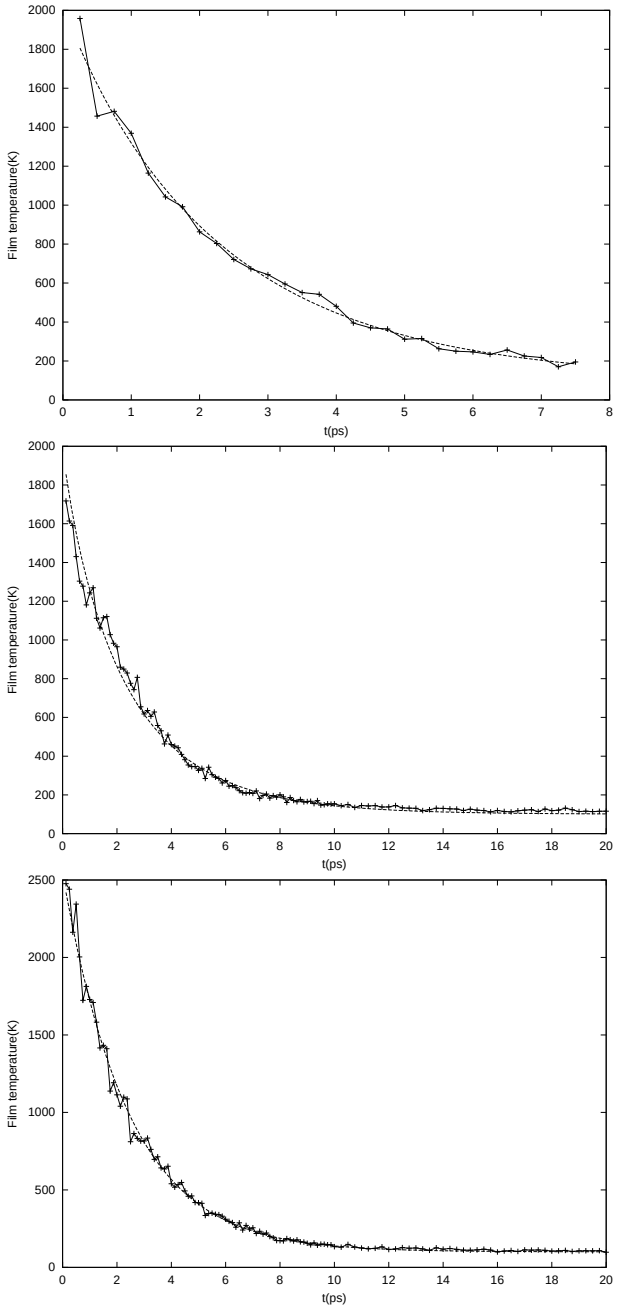

Figure 4.3: The observed stretched exponential functions for temperature relaxations in films e1T100Q (top), e1T100R20 (middle) and e5T100R20 (bottom). The best fit was retrieved according to $T_{film}(t) = c + \exp\left(at^{\beta} + b\right)$ K Fitting parameters are a = -0.46, -0.49, -0.41 fs^{-1}; b = 7.57, 7.54, 7.79; β = 0.95, 0.88, 1.00 and c = 100 K, for e1T100Q, e1T100R20 and e5T100R20, respectively. The $\beta \leq 1$ in all cases, producing stretched exponential relaxation.

4.3.2 Density

To ignore the effect of the rough surface on the top side of the grown film we identified two different cells: bulk and total sample (see section 2 and [koh01]). The bottom of the latter was 0.77 Å lower than the lowest z coordinate; and the top of the cell was the largest z coordinate, among silicon atoms in the amorphous network. For the bulk, this definition was slightly modified, by simply decreasing the z coordinate of the top of the cell by 3 Å. The x and y size of the cell was determined according to two-dimensional periodic boundary conditions. Table 4.1 contains the densities of different models. Each row is divided further into two rows. The upper ones always refer to the bulk and the second rows refer to the total sample. For realistic density calculations one should consider only the "bulk densities", which are always larger than for the total sample. At T_{sub} = 100 K bulk densities are between 2.3−2.5 g/cm^3, while in the quick energy dissipation models (T_{sub} = 300 K) the structures possess higher densities (2.4−2.8 g/cm^3). For crystalline silicon the density is equal to 2.33 g/cm^3, which is lower than the values we obtained for a−Si, i.e. our tight-binding molecular dynamics simulation provided more dense structures. There was no significant changing in density during relaxations.

4.3.3 Ring statistics

A surprising result was found in ring statistics. We defined a ring as a closed path, which starts from a given atom walking only on the first neighbor bonds. Every atom is visited only once and bonds can exist only between adjacent atoms. The size of the ring is the number of atoms forming a closed path. We considered only ring sizes smaller or equal to eight but there are not any eightfold rings in the networks. The ring statistics are displayed in Table 4.2. Networks prepared by our models have a significant number of three membered rings, i.e. triangles are present in the atomic arrangement. Furthermore, squares can also be found. Most of the theoretical models for a−Si do not contain such fractions of the structure. It seems to be an important result although a neutron diffraction measurement carried out on a pure evaporated amorphous silicon sample, and evaluated by reverse Monte Carlo method had a similar conclusion [kug93]. Nevertheless, the systematic analysis of the structural data of the Cambridge Structural Database suggests that the equilateral triangles and near planar squares can also be natural local configurations inside the atomic arrangements of a−Si [kug01]. All of the three independent pieces of evidence support the existence of triangles in a−Si structures.

Significant differences can be found in ring statistics between samples constructed by rapid quenching and by atom-by-atom deposition. From Table 4.2 it can be seen that for the model e1T100Q (rapid quenching) the number of rings is much lower than for e1T100R20 and for e1T100Q, i.e. models prepared by different techniques have

Table 4.2: Ring statistics, for different first neighbor shells 2.6, 2.7, 2.82 and 3.0 Å, respectively.

Model	Ring statistics (2.59 Å)				
	3	4	5	6	7
e1T100R5	12	10	50	86	95
e1T100R10	25	10	61	85	93
e1T100R20	9	14	68	89	102
e5T100R5	11	9	51	45	65
e5T100R10	14	21	74	84	96
e5T100R20	18	20	78	103	116
e1T300	13	9	33	36	46
e5T300	13	8	44	31	33
e10T300	7	8	16	19	12
e1T100Q	6	13	63	72	86

Model	Ring statistics (2.82 Å)				
	3	4	5	6	7
e1T100R5	63	35	115	138	202
e1T100R10	73	37	122	169	232
e1T100R20	66	35	121	160	248
e5T100R5	62	53	151	163	247
e5T100R10	75	58	152	184	265
e5T100R20	81	36	128	162	229
e1T300	63	45	84	87	97
e5T300	92	55	102	132	169
e10T300	54	43	71	60	82
e1T100Q	75	29	109	129	181

Model	Ring statistics (2.7 Å)				
	3	4	5	6	7
e1T100R5	39	26	83	111	157
e1T100R10	53	20	91	134	155
e1T100R20	53	24	95	142	188
e5T100R5	38	36	119	120	199
e5T100R10	38	35	118	133	173
e5T100R20	53	28	107	130	165
e1T300	37	26	61	67	84
e5T300	56	33	78	91	131
e10T300	34	25	48	33	41
e1T100Q	35	26	75	98	130

Model	Ring statistics (3.0 Å)				
	3	4	5	6	7
e1T100R5	80	45	120	174	235
e1T100R10	91	50	135	181	273
e1T100R20	82	56	137	177	276
e5T100R5	95	84	169	230	323
e5T100R10	102	66	170	197	307
e5T100R20	95	58	157	188	293
e1T300	81	55	87	95	118
e5T300	123	72	136	158	277
e10T300	72	47	85	69	92
e1T100Q	96	41	140	147	222

different medium range order. We can also conclude that for the latter model the number of rings has decreased compared to the initial e1T100R20 model. With the exception of the ring statistics which were different, all the other structural parameters of these models were similar.

4.3.4 Coordination number

It is known from diffractions that the first neighbor coordination number in amorphous silicon is approximately four. We have found that this number can only be provided in our models if we choose 2.6 Å for the first neighbor shell. Nevertheless, the densities of our models are bigger than in crystalline silicon. This means, our amorphous models do not have big voids, indicating that the model potential shows

more or less properties of amorphous and liquid silicon systems at the same time. In the case of taking the first neighbor shell to 2.82 and 3.0 Å, we received coordination numbers close to five, which is between the average coordination number in amorphous ($\langle Z \rangle \approx 4$) and liquid ($\langle Z \rangle \approx 6$) silicon.

Figure 4.1 illustrates the first neighbor distances. It is clear that in the case of 2.6 Å first neighbor shells, the lowest first neighbor distances are dominated by $Si_{Z=4}$−$Si_{Z=4}$ distances (dashed line). The distances between other coordinated silicon atoms only contribute to larger distances than the interatomic separation in crystalline silicon (2.36 Å) and do not contribute to lower distances, which can be seen in the experimental curve (dotted line) in Fig. 4.1.

To our present knowledge, there is no silicon tight-binding model potential, which can more accurately describe the amorphous phase. Vink *et al.* proposed a modified Stillinger-Weber classical empirical potential very recently [vin01], which they believe can be used to describe the structure of amorphous silicon.

4.3.5 Radial distribution and bond angle distribution functions

In Fig. 4.1 the first and second neighbor peaks of e1T100Q model can be seen. All the other models show similar radial distribution functions. The tight-binding potential applied in our computer experiments overestimates the first neighbor distance. However, if the potential would provide only silicon atoms with a coordination equal to four, the position of the peak for the first neighbor shell would be in the right position.

The main contribution to the bond angle distribution arises from angles between 95° and 125°. We found a large amount of triangles in our samples, there is therefore a significant contribution from bond angles close to 60°. We believe this causes the average bond angle to be smaller than 109°, which is the tetrahedral angle in diamond structures, in our systems.

4.4 Summary

We have developed a tight-binding molecular dynamics computer code to simulate the preparation procedure of amorphous silicon, which are grown by a vapor deposition technique. Nine structures were simulated by this method. An additional tenth model (e1T100Q) was prepared by rapid cooling in order to make a comparison between the atom-by-atom deposition on a substrate and melt-quenching preparation techniques.

The most important difference we have found between the models prepared in varied conditions, is in the ring statistics, i.e. in medium range order. In our simula-

tions triangles are present in the atomic arrangement. Two other independent pieces of evidence support the existence of triangles in a−Si structures. Nevertheless, the fragments like equilateral triangles have never been considered at electronic density of states calculations or with unsolved problems such as the breaking of weak bonds by prolonged illumination, which is the major mechanism for the light-induced defect creation [shi95].

The tight-binding model potential used in our computer experiments slightly overestimates the bond distances, giving values which were observed previously in liquid forms [ish96]. A more important problem is that the TB potential provides overcoordinated atomic sites (five- even sixfold coordinated atoms) during the amorphous silicon simulations. The sixfold coordinated atoms we obtained can be found in the liquid phase of silicon instead of in the amorphous structure. The well-known Stillinger-Weber classical empirical potential for amorphous silicon had a similar difficulty, yet this has recently been successfully modified [vin01]. A possible future aim is to improve this TB potential by a similar process.

Bibliography

[bar77] A. Barna, P. B. Barna, G. Radnoczi, L. Toth, and P. Thomas, phys. stat. sol.(a) **41**, 81 (1977).

[cic90] A. Di Cicco, A. Bianconi, C. Coluzza, P. Rudolf, P. Lagarde, A.M. Flank and A. Marcelli, J. Non-Cryst. Solids **116**, 27 (1990).

[for89] J. Fortner and J. S. Lannin, Phys. Rev. B **39**, 5527 (1989).

[hen96] H. Hensel, P. Klein, H. M. Urbassek, and T. Frauenheim, Phys. Rev. B **53**, 16497 (1996).

[her00] C. P. Herrero, J. Phys.: Condens. Matter **12**, 265 (2000).

[ish96] M. Ishimaru, K. Yoshida, T. Kumamoto, and T. Motooka, Phys. Rev. B **54**, 4638 (1996).

[ish97] M. Ishimaru, Sh. Munetoh, and T. Motooka, Phys. Rev. B **56**, 15133 (1997).

[kea66] P.N. Keating, Phys. Rev. **145**, 637 (1966).

[kel88] P.C. Keriles and J. Tersoff, Phys. Rev. Lett. **61**, 562 (1988).

[koh01] K. Kohary and S. Kugler, Phys Rev. B **63**, 193404 (2001).

[kug89] S. Kugler, G. Molnar, G. Peto, E. Zsoldos, L. Rosta, A. Menelle and R. Bellissent, Phys. Rev. B **40**, 8030 (1989).

[kug93] S. Kugler, L. Pusztai, L. Rosta, P. Chieux, R. Bellissent, Phys. Rev. B **48**, 7685 (1993).

[kug01] S. Kugler and Z. Várallyay, Phil. Mag. Lett. **81**, No.8 (2001). (in press)

[kug_tbp] S. Kugler, Z. Várallyay, and K. Kohary, (to be published).

[kwo94] I. Kwon, R. Biswas, C.Z. Wang, K.M. Ho and C.M. Soukoulis, Phys. Rev. B **49**, 7242 (1994).

[laa99] K. Laaziri, S. Kycia, S. Roorda, M. Chicoine, J. L. Robertson, J. Wang and S. C. Moss, Phys. Rev. B **60**, 13 520 (1999).

[lue89] W.D. Luedtke and U. Landman, Phys. Rev. B **40**, 11733 (1989).

[mor99] K. Morigaki, *Physics of Amorphous Semiconductors*, (World Scientific Publishing Co. 1999.)

[moss70] S.C. Moss and J. F. Graczyk, Proc. 10th Int. Conf. Physics of Semiconductors, Cambridge, Massachusetts, USA, edited by S. P. Keller, J.C. Hesnel, and F. Stern (USAEC, 1970), p658.

[shi95] K. Shimakawa, A. Kolobov and S.R. Elliott, Adv. in Phys. **44**, 475 (1995).

[sti91] I. Stich, R. Car and M. Parrinello, Phys. Rev. B **44**, 11092 (1991).

[tót94] G. Tóth and G. Náray-Szabó, J. Chem. Phys. **100**, 3742 (1994).

[vin01] R.L.C. Vink, G.T. Barkema, W.F. van der Weg, N. Mousseau, J. Non-Cryst. Solids, **282**, 248 (2001).

[woo85] F. Wooten, K. Winer, and D. Weaire, Phys. Rev. Lett. **54**, 1392 (1985).

[yan98] R. Yang, J. Singh, J. Non-Cryst. Solids **240**, 29 (1998).

Chapter 5

One-dimensional hopping in disordered organic solids

5.1 Introduction

Transport of charge carriers in disordered organic solids, such as molecularly doped polymers, conjugated polymers and organic glasses has been the subject of intensive experimental and theoretical study for about 20 years [bäs93]. In recent years particular attention has been devoted to the columnar discotic liquid–crystalline glasses due to their potential technical applications for electrophotography and as transport materials in light-emitting diodes [bac97, chr97a]. Dielectric measurements have clarified that charge transport in most of such materials is extremely anisotropic [bod95] so that it is reasonable to describe the transport of charge carriers as a one–dimensional process [ble99]. Moreover, experimentally observed dependences of the conductivity on the frequency, on the strength of the applied electric field and on the temperature evidence that an incoherent hopping process is the dominant transport mechanism in such materials [bod95, ble99, och99a, och99b]. It has been found reasonable to describe the transport of charge carriers as a hopping process via molecules arranged in spatially ordered one–dimensional chains [ble99]. The energy levels which are responsible for charge transport are usually characterized by a Gaussian density of states (DOS) [bäs93, dun96, ble99, och99a]:

$$g(\epsilon) = \frac{1}{\sqrt{2\pi\sigma^2}} \exp\left(-\frac{\epsilon^2}{2\sigma^2}\right). \tag{5.1}$$

The origins of the energy disorder characterized by parameter σ could be fluctuations in the polarization energy as well as dipolar interactions or impurity molecules [ble99]. Such systems represent an excellent field to test various theoretical approaches. These approaches differ from each other, for example, with respect to the choice of transition rates for single hopping events. The choice of transition rates is of course limited as

they must fulfill the detailed balance condition to be physically reasonable in thermal equilibrium. The most plausible transition probabilities for the hopping of charge carriers via localized states were suggested by Miller and Abrahams [mil60, bäs93, ble99]: the jump rate from an occupied localized state i to an empty state j separated by distance $R_{i,j}$ is the product of a prefactor Γ_1, overlap of the wave functions of states i and j, and the Boltzmann factor for jumps upward in energy [mil60],

$$\Gamma_{i,j} = \Gamma_1 \exp\left(-\frac{2R_{i,j}}{\alpha}\right) \exp\left(-\frac{\epsilon_j - \epsilon_i + \mid \epsilon_j - \epsilon_i \mid}{2kT}\right). \tag{5.2}$$

Here α is the decay length of the carrier wave function in the localized states and k is the Boltzmann constant. Allowing only hops to nearest neighbors and assuming that chains of localized states are spatially regular we omit the R-dependence of the transition probabilities and use the Miller-Abrahams transition rates in the form

$$\Gamma_{i,j} = \nu_0 \exp\left(-\frac{\epsilon_j - \epsilon_i + \mid \epsilon_j - \epsilon_i \mid}{2kT}\right) \tag{5.3}$$

with prefactor $\nu_0 = \Gamma_1 \exp(-2b/\alpha)$, b being the distance between the neighboring sites on the conduction chain. Nearest–neighbor hopping within the model described by Eq. (5.1) and Eq. (5.3) has been recently studied by computer simulations [ble99]. Other forms of transition probabilities have also been considered in the literature. For example, a symmetric form was recently used in order to analyze analytically the field and temperature dependences of the hopping conductivity in one–dimensional systems [dun96]:

$$\Gamma_{i\pm1,i} = \nu_0 \exp\left(-\frac{\epsilon_{i\pm1} - \epsilon_i}{2kT}\right). \tag{5.4}$$

Two models have been discussed in the literature with respect to the space-energy correlations of localized states responsible for transport. In the so-called Gaussian disorder model (GDM), such correlations are neglected [bäs93, ble99]. In the correlated disorder model (CDM), it is assumed that energy distributions for spatially close sites are correlated, for example, due to dipole or quadrapole interactions [dun96, gar95, nov98a, nov98b].

The drift mobility of carriers in organic disordered media usually demonstrates exponential dependences on temperature T and electric field E in the form

$$\mu \propto \exp\left[-\left(\frac{T_0}{T}\right)^2\right] \exp\left[\sqrt{\frac{E}{E_0}}\right], \tag{5.5}$$

where T_0 and E_0 are parameters. Much attention has been paid in recent years to the dependence of the mobility on electric field [dun96, gar95, nov98a, nov98b] and it has been claimed that in three–dimensional (3D) systems the observed field dependence

in a wide range of electric fields can be explained only by the CDM. We check below whether this is true for a one–dimensional (1D) system.

As far as the dependence of the mobility on temperature is concerned, the situation is widely believed to have been cleared up many years ago. Computer simulations [sch81] and analytical calculations [gru84, mov86] in 3D case were carried out giving the dependence

$$\mu \propto \exp\left[-\left(C\frac{\sigma}{kT}\right)^2\right] \tag{5.6}$$

with $C \approx 2/3$. This expression is widely believed to be universal for the above model and it is often used to determine disorder parameter σ of assumed Gaussian DOS in various materials from the experimental measurements [och99a, ném96]. However, it is necessary to emphasize that there is no agreement among researchers concerning the magnitude of the coefficient C for one–dimensional systems. Ochse *et al.* [och99a] used the 3D value $C = 2/3$ for columnar systems with one–dimensional transport, while Bleyl *et al.* [ble99] obtained $C \approx 0.9$ in their computer simulations for 1D case with asymmetric transition probabilities. The analytic calculations of Dunlap *et al.* [dun96] for symmetric probabilities predict $C = 1$ in 1D case.

In this chapter the temperature dependence in Eq. (5.6) will be studied in order to clarify this dependence for the GDM and the CDM. This chapter concentrates on the contribution of the author in that field, i.e. in computer simulations [koh01]. However, the work was done together with the analytical work performed by Dr. Harald Cordes [cor01]. The analytical results will be summarized in section 5.2 and may occasionally be mentioned together with the computer simulation results as well. In section 5.3 the results of Monte Carlo simulations will be gathered.

5.2 Analytic theory

The steady–state drift velocity of carriers in one–dimensional periodic systems can be written exactly using the general solution found by Derrida [der83],

$$v = \frac{Nb\left[1 - \prod_{k=0}^{N-1}\frac{\Gamma_{k+1,k}}{\Gamma_{k,k+1}}\right]}{\sum_{k=0}^{N-1}\frac{1}{\Gamma_{k,k+1}}\left[1 + \sum_{i=1}^{N-1}\prod_{j=1}^{i}\frac{\Gamma_{k+j,k+j-1}}{\Gamma_{k+j,k+j+1}}\right]}, \tag{5.7}$$

where N is the periodicity of the system and b is the distance between nearest neighbor sites. This formula was recently used by Dunlap *et al.* [dun96] to study the field dependence of the drift mobility in a one–dimensional system with symmetric transition rates [dun96]. The drift mobility μ is related to the steady–state velocity as

$$\mu = \frac{v}{E}. \tag{5.8}$$

However in experiments, the drift mobility is usually obtained by the time–of–flight technique. Here charge carriers pass only once through a sample of finite thickness [ble99, och99a] and drift mobility is calculated by dividing the sample length Nb by the mean transit time $\bar{t}_{0N}$ and electric field E:

$$\mu = \frac{Nb}{\bar{t}_{0N} E}. \tag{5.9}$$

Murthy and Kehr [mur90] have derived the analytical expression for the mean transit time of carriers through a given chain of $N+1$ sites

$$\bar{t}_{0N} = \sum_{k=0}^{N-1} \frac{1}{\Gamma_{k,k+1}} + \sum_{k=0}^{N-2} \frac{1}{\Gamma_{k,k+1}} \sum_{i=k+1}^{N-1} \prod_{j=k+1}^{i} \frac{\Gamma_{j,j-1}}{\Gamma_{j,j+1}}. \tag{5.10}$$

This formula gives the transit time for a charge carrier that starts on site 0 and finishes on site N. The time is averaged over many transit times through the same chain with given values of transition probabilities Γ_{ij}.

One should be cautious with the application of Eqs. (5.9) and (5.10) at low electric fields. Even without an applied electric field carriers starting at site 0 will pass through the system solely due to a diffusion process. At low fields, diffusion dominates the motion of carriers and it would be wrong to use Eq. (5.9). In such cases it would be more appropriate to estimate the mobility via the diffusion formula

$$\mu = \frac{e}{kT} \frac{b^2 N^2}{2\bar{t}_{0N}}. \tag{5.11}$$

which presumes the validity of the Einstein relation.

Note that Eqs. (5.7), (5.8) and Eqs. (5.9), (5.10) are valid for any type of nearest–neighbor hopping of noninteracting carriers in one–dimensional systems.

5.2.1 Drift mobility in the random-barrier model

We start our analysis with a simple random-barrier model (RBM). In the RBM, all sites have equal energies being separated by energy barriers. Transition probabilities in the presence of electric field E are given by expressions

$$\Gamma_{k,k+1} = \nu_0 \exp\left(-\frac{\Delta_k - \frac{1}{2}ebE + |\Delta_k - \frac{1}{2}ebE|}{2kT} \right) \tag{5.12}$$

and

$$\Gamma_{k+1,k} = \nu_0 \exp\left(-\frac{\Delta_k + \frac{1}{2}ebE + |\Delta_k + \frac{1}{2}ebE|}{2kT} \right), \tag{5.13}$$

where Δ_k is the energy barrier between sites k and $k+1$.

In the limit of long periods (long chains), $N \gg 1$, calculation of the drift mobility via Eqs. (5.7), (5.8) or Eqs. (5.9), (5.10) for any chain with a given distribution of transition rates is equivalent to the averaging of Eq. (5.7) or Eq. (5.10) over all possible distributions of transition rates determined by disorder. In the following we will call this "averaging over disorder". Within the RBM, the averaging over disorder is given by [der83, mur90]

$$v = b\left[1 - \left\langle \frac{\Gamma_{k+1,k}}{\Gamma_{k,k+1}} \right\rangle\right] \Big/ \left\langle \frac{1}{\Gamma_{k,k+1}} \right\rangle, \tag{5.14}$$

where $\langle \ldots \rangle$ denotes the averaging over the distribution of barrier heights $p(\Delta)$. Note that Eq. (5.14) can be derived by both equations, Eq. (5.7) and Eq. (5.10). The explicit expressions for the averaging in the RBM are

$$\left\langle \frac{1}{\Gamma_{k,k+1}} \right\rangle = \nu_0^{-1} \int_0^{ebE/2} d\Delta\ p(\Delta) + \nu_0^{-1} \int_{ebE/2}^{\infty} d\Delta\ p(\Delta) e^{\frac{\Delta - ebE/2}{kT}} \tag{5.15}$$

and

$$\left\langle \frac{\Gamma_{k+1,k}}{\Gamma_{k,k+1}} \right\rangle = \int_0^{ebE/2} d\Delta\ p(\Delta) e^{-\frac{\Delta + ebE/2}{kT}} + \int_{ebE/2}^{\infty} d\Delta\ p(\Delta) e^{-\frac{ebE}{kT}}. \tag{5.16}$$

Assuming a Gaussian distribution of barriers,

$$p(\Delta) = \frac{2}{\sqrt{2\pi\sigma^2}} \exp\left(-\frac{\Delta^2}{2\sigma^2}\right), \tag{5.17}$$

one obtains for the drift mobility

$$\mu = \frac{b\nu_0}{E}\ \frac{1 - e^{\frac{\sigma^2}{2(kT)^2} - \frac{ebE}{2kT}} \left[\mathrm{erf}\left(\frac{ebE}{\sqrt{8}\sigma} + \frac{\sigma}{\sqrt{2}kT}\right) - \mathrm{erf}\left(\frac{\sigma}{\sqrt{2}kT}\right)\right] - e^{-\frac{ebE}{kT}} \left[1 - \mathrm{erf}\left(\frac{ebE}{\sqrt{8}\sigma}\right)\right]}{\mathrm{erf}\left(\frac{ebE}{\sqrt{8}\sigma}\right) + e^{\frac{\sigma^2}{2(kT)^2} - \frac{ebE}{2kT}} \left[1 - \mathrm{erf}\left(\frac{ebE}{\sqrt{8}\sigma} - \frac{\sigma}{\sqrt{2}kT}\right)\right]}, \tag{5.18}$$

where $\mathrm{erf}(x) = \frac{2}{\sqrt{\pi}} \int_0^x \exp(-y^2) dy$ is the error function. In Fig. 5.1 the calculated field dependences of the drift mobility are shown for parameters $b = 3.6$ Å, $\sigma = 50$ meV, $kT = 25$ meV. The solid line represents the exact solution for infinite chain given by Eq. (5.18). All points in the figure correspond to mobilities for finite chains of $N = 500$ sites averaged over 1000 different chains. Circles were obtained via Eqs. (5.9), (5.10) while squares via Eqs. (5.10), (5.11). Results of our Monte Carlo computer simulation are shown by crosses to demonstrate the excellent agreement of the simulation results with the analytical theory. At low fields, drift approximation (Eqs. (5.9), (5.10))

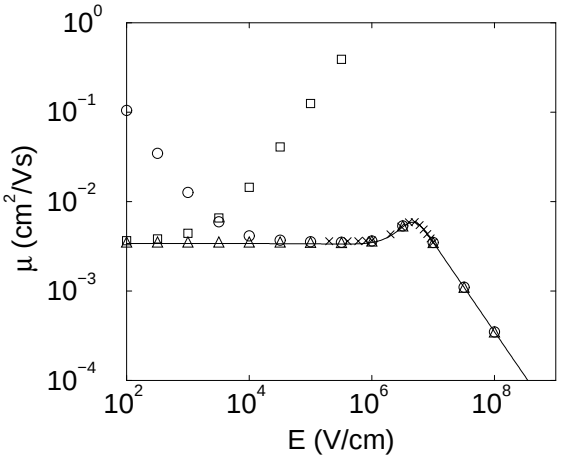

Figure 5.1: Field dependence of the carrier mobility in the RBM for Gaussian distribution of barrier heights with the width $\sigma = 50$ meV at temperature $kT = 25$ meV. The solid line represents exact solution for the infinite chain. Data shown by circles and squares were calculated via Eq. (5.10) using drift and diffusion relation, respectively. Data shown by triangles were calculated via Eq. (5.7), while those shown by crosses were obtained by Monte Carlo simulations presented in the section 5.3. The chain length N was 500 and averaging was performed over $c = 1000$ chains.

for finite systems leads to the increase of the calculated mobility with decreasing field strength. Similar results are obtained for all considered models of disorder and various forms of the transition probabilities between neighboring sites. This result simply reflects the fact that charge carriers can penetrate through a finite system via diffusion motion even in the absence of an external electric field. By using Eq. (5.9) one overestimates the mobility at low fields. The same happens with using Eq. (5.11) at higher fields. Comparison of Eqs. (5.9) and (5.11) reveals the strength of the electric field at which a transition from the diffusion-controlled to the drift-controlled transit times takes place: $E \simeq 2kT/eNb$.

At low fields, transition time $\bar{t}_{0N}$ does not depend on the strength of the electric field E being determined mostly by diffusion. Using Eq. (5.9) one artificially obtains an increasing drift mobility at decreasing field E. In numerous publications experimental results were reported that evidence the decrease of the drift mobility with increasing electric field [pel88, sch92, abk92]. This was always observed at high temperatures at which diffusion can really dominate the motion of charge carriers. Experimental evidence for decreasing mobility with increasing field is usually obtained using equations similar to Eq. (5.9), where the drift mobility is determined via the measured transit time by dividing the sample length by the value of this time and by the value of the field strength. We believe that this calculation is not appropriate and a diffusion equation similar to Eq. (5.11) should be used at low fields and

high temperatures. In 3D case, this equation should be slightly modified, though the conclusion is the same: decreasing of the drift mobility with increasing field strength at low fields is an artifact caused by using the wrong equation [similar to Eq. (5.9)] for evaluation of the mobility on the basis of the measured transit time. In our 1D calculations we illustrate this idea by using Eq. (5.11) instead of Eq. (5.9) for finite systems at low electric fields. The result is shown by squares in Fig. 5.1. The excellent agreement with the exact calculation for the infinite system at low fields confirms our conclusion. For the chosen parameters, the linear transport regime with the mobility independent of the electric field is valid up to the field strength of approximately 10^6 V/cm, where a nonlinear regime starts with the mobility increasing with electric field. The latter regime is valid in a rather narrow range. At higher electric fields it is replaced by the trivial regime in which electric field eliminates the energy barriers between the sites of the chain and the transit time becomes field independent. In such a case mobility decreases proportionally to $1/E$.

In Fig. 5.2 the field dependence of the drift mobility is shown for a lower temperature $kT = 15$ meV for the same system as in Fig. 5.1 with $\sigma = 50$ meV and $b = 3.6$ Å. Clear mesoscopic effects are seen in this figure as evidenced by the difference in the results obtained by averaging the mobilities (open symbols) and those obtained by averaging the transit times or the inverse mobilities (solid symbols). In all cases, averagings were performed over 1000 different chains, each chain consisting of 500 sites. The difference in the results of the two different averaging procedures reflects the presence of "fast" and "slow" chains. Averaging of times corresponds to the successive arrangement of chains where slow electron transitions over untypically high energy barriers determine the transport coefficients. On the contrary, the averaging of the mobilities corresponds to the parallel arrangement of chains, in which the fastest chains with untypically low energy barriers provide fast transit times of charge carriers. In the next section, we show that qualitatively the same effects are also inherent for the more realistic random-energy model.

5.2.2 Drift mobility in the random-energy model without correlations

In this section we consider a random–energy model with a Gaussian DOS described by Eq. (5.1), presuming that there are no correlations between spatial positions of chain sites and their energies. This model is called in the literature a Gaussian disorder model (GDM). It has recently been suggested for the transport of charge carriers in discotic columnar liquid crystalline glasses with transition rates described by Eq. (5.3) and it was studied by computer simulations [ble99]. The exact analytic results for this model based on Eqs. (5.7) and (5.10) will be presented below.

In Eq. (5.3), site energies ϵ_k depend on the strength of the electric field E. They

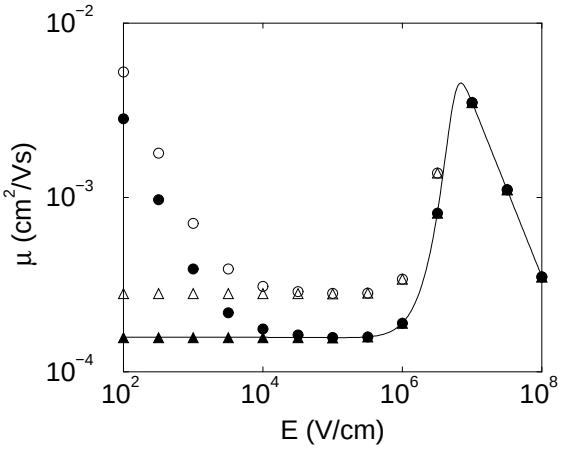

Figure 5.2: Field dependence of the carrier mobility in the RBM. Chain length $N = 500$, number of chains $c = 1000$, width of barrier height distribution $\sigma = 50$ meV, temperature $kT = 15$ meV. Open circles and open triangles show the data obtained by averaging over chain mobilities calculated by Eq. (5.10) and Eq. (5.7), respectively. Solid symbols give the data obtained by the corresponding averaging over the inverse mobilities.

are related to the zero field site energies ϕ_k as $\epsilon_k = \phi_k - ekbE$. In accordance with Eq. (5.3), the ratio of forward $\Gamma_{k,k+1}$ and backward $\Gamma_{k+1,k}$ hopping rates for any pair of neighboring sites is

$$\frac{\Gamma_{k+1,k}}{\Gamma_{k,k+1}} = \exp\left(\frac{\epsilon_{k+1} - \epsilon_k}{kT}\right) \tag{5.19}$$

equivalent to the condition of the detailed balance, which recently [keh96] has been used to determine the diffusion coefficient in thermal equilibrium for any form of the transition rates.

Inserting relation (5.19) into Eq. (5.7), one obtains

$$v = \frac{bN\left[1 - \exp\left(-\frac{NebE}{kT}\right)\right]}{\sum\limits_{k=0}^{N-1} \frac{1}{\Gamma_{k,k+1}} + \sum\limits_{k=0}^{N-1} \exp\left(-\frac{\phi_k}{kT}\right) \sum\limits_{i=1}^{N-1} \frac{\exp\left(-\frac{iebE}{kT}\right)}{\exp\left(-\frac{\phi_{k+i}}{kT}\right)\Gamma_{k+i,k+i+1}}}. \tag{5.20}$$

The only random variables in Eq. (5.20) are the zero field site energies ϕ_k and the forward transition rates $\Gamma_{k+i,k+i+1}$, which in turn depend only on neighboring site energies ϕ_{k+i} and ϕ_{k+i+1}. Since in all products appearing in the second term of the denominator, ϕ_k is not correlated with ϕ_{k+i} or $\Gamma_{k+i,k+i+1}$, averaging over disorder can be carried out for $\exp(-\phi_k/kT)$ and $\exp(\phi_{k+i}/kT)\Gamma^{-1}_{k+i,k+i+1}$ separately. Therefore the steady-state velocity and the mean transit time of carriers through long chains, $N \gg 1$ are given by

$$v = b\left(\left\langle\frac{1}{\Gamma_{k,k+1}}\right\rangle + \left\langle\frac{\left\langle\exp\left(-\frac{\phi_k}{kT}\right)\right\rangle}{\exp\left(-\frac{\phi_k}{kT}\right)\Gamma_{k,k+1}}\right\rangle\frac{\exp\left(-\frac{ebE}{kT}\right)}{1-\exp\left(-\frac{ebE}{kT}\right)}\right)^{-1}, \tag{5.21}$$

$$\frac{\bar{t}_{0N}}{N} = \left\langle\frac{1}{\Gamma_{k,k+1}}\right\rangle + \left\langle\frac{\left\langle\exp\left(-\frac{\phi_k}{kT}\right)\right\rangle}{\exp\left(-\frac{\phi_k}{kT}\right)\Gamma_{k,k+1}}\right\rangle\frac{\exp\left(-\frac{ebE}{kT}\right)}{1-\exp\left(-\frac{ebE}{kT}\right)}. \tag{5.22}$$

The relation $v = bN/\bar{t}_{0N}$ provides the equivalence of Eq. (5.22) and (5.21) in long chains as should be expected. Note that Eqs. (5.21) and (5.22) are exact for all kinds of nearest–neighbor hopping rates fulfilling Eq. (5.19). Thus they can as well be applied to the symmetric transition rates given by Eq. (5.4).

The results of the averaging over Gaussian disorder for various terms in Eqs. (5.21), (5.22) are:

$$\left\langle e^{-\frac{\phi_k}{kT}}\right\rangle = \exp\left[\frac{1}{2}\left(\frac{\sigma}{kT}\right)^2\right], \tag{5.23}$$

$$\left\langle\frac{1}{\Gamma_{k,k+1}}\right\rangle = \frac{1}{2\nu_0}\left\{1+\operatorname{erf}\left(\frac{ebE}{2\sigma}\right)+\exp\left[\left(\frac{\sigma}{kT}\right)^2\right]\exp\left(-\frac{ebE}{kT}\right)\left[1+\operatorname{erf}\left(\frac{\sigma}{kT}-\frac{ebE}{2\sigma}\right)\right]\right\} \tag{5.24}$$

and

$$\left\langle\frac{1}{\exp\left(-\frac{\phi_k}{kT}\right)\Gamma_{k,k+1}}\right\rangle = \frac{e^{\frac{\sigma^2}{2(kT)^2}}}{2\nu_0}\left\{1+\operatorname{erf}\left(\frac{\sigma}{2kT}+\frac{ebE}{2\sigma}\right)+e^{-\frac{ebE}{kT}}\left[1+\operatorname{erf}\left(\frac{\sigma}{2kT}-\frac{ebE}{2\sigma}\right)\right]\right\}. \tag{5.25}$$

Thus in the one–dimensional GDM the drift mobility of carriers on an infinite chain is

$$\mu = \frac{2\nu_0 b}{E}\left(1+\operatorname{erf}\left(\frac{ebE}{2\sigma}\right)+e^{\frac{\sigma^2}{(kT)^2}-\frac{ebE}{kT}}\left[1+\operatorname{erf}\left(\frac{\sigma}{kT}-\frac{ebE}{2\sigma}\right)\right]+\right.$$
$$\left.\frac{e^{\frac{\sigma^2}{(kT)^2}-\frac{ebE}{kT}}}{1-e^{\frac{ebE}{kT}}}\left\{e^{-\frac{ebE}{kT}}\left[1+\operatorname{erf}\left(\frac{\sigma}{2kT}-\frac{ebE}{2\sigma}\right)\right]+1+\operatorname{erf}\left(\frac{\sigma}{2kT}+\frac{ebE}{2\sigma}\right)\right\}\right)^{-1} \tag{5.26}$$

At low electric fields this exact expression can be approximated by

$$\mu \simeq \frac{\nu_0 b}{2E}\exp\left(-\frac{\sigma^2}{(kT)^2}\right)\left[\exp\left(\frac{ebE}{kT}\right)-1\right], \tag{5.27}$$

while at high fields $\mu \simeq \nu_0 b/E$. Interpolation of both approximations gives

$$\mu \simeq \frac{\nu_0 b}{E}\left[1+\frac{2\exp\left(\frac{\sigma^2}{(kT)^2}\right)}{\exp\left(\frac{ebE}{kT}\right)-1}\right]^{-1}. \tag{5.28}$$

Field dependences of the drift mobility are shown in Fig. 5.3 for $b = 3.6$ Å, $\sigma = 50$ meV, $kT = 25$ meV. The solid line represents the exact solution for an infinite chain given by Eq. (5.26). Dashed lines show approximations via Eqs. (5.27) and $\mu \simeq \nu_0 b/E$, respectively. The dotted line illustrates the interpolation formula [Eq. (5.28)] which appears to be in excellent agreement with the exact solution. Circles and triangles in the figure show the calculated results for finite systems of 2000 sites averaged over 1000 different chains once using the averaging of inverse transit times (circles) and once using the averaging of inverse velocities (triangles). Qualitatively, the results for the random-energy model in Fig. 5.3 resemble those for the random-barrier model from Figs. 5.1 and 5.2 and we refer the reader to the corresponding parts of the previous section, where the latter results were discussed. In Fig. 5.4, the field dependences of the drift mobility are shown in the Poole-Frenkel representation ($\ln\mu$ versus $\sqrt{E}$) for two different temperatures and two different averaging procedures. The figure clearly shows that in the chosen model the analytic solution of the carrier mobility hardly can be described by the Poole-Frenkel law $\ln\mu \propto \sqrt{E}$. This conclusion is in agreement with previous studies of Gartstein and Conwell [gar95], Dunlap *et al.* [dun96] and of Novikov *et al.* [nov98a, nov98b]. Following these authors we consider in the next section the field dependence of the drift mobility in the model of correlated disorder (CDM). In the rest of this section we concentrate on the temperature dependence of the drift mobility at low electric fields in the Gaussian disorder model (GDM).

The low field mobility for a finite chain is given by Eqs. (5.20) and (5.8) in the limit of $E \to 0$:

$$\mu = \frac{eb^2}{kT}\left[\frac{1}{N}\sum_{k=0}^{N-1}\exp\left(-\frac{\phi_k}{kT}\right)\times\frac{1}{N}\sum_{k=0}^{N-1}\frac{1}{\exp\left(-\frac{\phi_k}{kT}\right)\Gamma_{k,k+1}}\right]^{-1}. \tag{5.29}$$

For the infinite chain this expression is equal to

$$\mu = \frac{eb^2}{kT}\Bigg/\left\langle\frac{\left\langle\exp\left(-\frac{\phi_k}{kT}\right)\right\rangle}{\exp\left(-\frac{\phi_k}{kT}\right)\Gamma_{k,k+1}}\right\rangle. \tag{5.30}$$

With hopping rates described by Eq. (5.3) low field mobility in the GDM is exactly given by

$$\mu = \frac{\nu_0 eb^2}{kT}\exp\left[-\left(\frac{\sigma}{kT}\right)^2\right]\left[1+\mathrm{erf}\left(\frac{\sigma}{2kT}\right)\right]^{-1}. \tag{5.31}$$

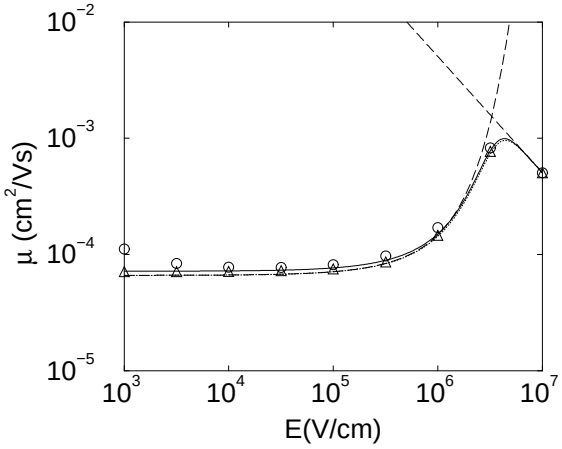

Figure 5.3: Field dependence of the carrier mobility for nearest neighbor hopping with Miller–Abrahams rates between sites with Gaussian energy distribution. The solid line shows the exact solution for an infinite chain. Dashed lines correspond to the low-field and high-field approximations, while the dotted line gives the interpolation between them. Circles show the averaged mobilities of $c = 1000$ chains with $N = 2000$ sites each calculated according to Eq. (5.10) and Eq. (5.9). Triangles represent the results obtained by averaging the inverse mobilities for the same chains calculated by Eq. (5.20) and Eq. (5.8). Temperature and the width of the energy distribution were chosen as $kT = 25$ meV and $\sigma = 50$ meV.

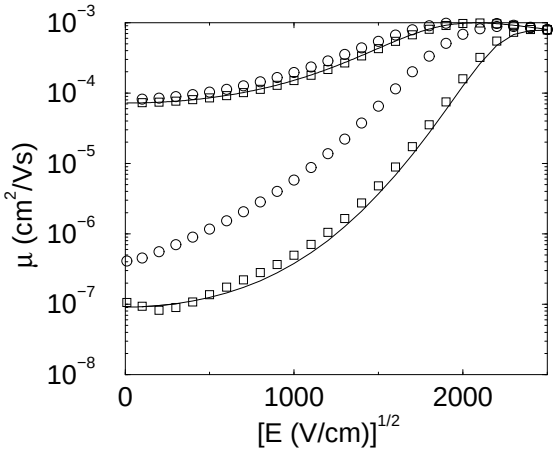

Figure 5.4: Poole–Frenkel plots for carrier mobilities at $kT = 25$ meV (upper curves) and $kT = 15$ meV (lower curves). Circles show the averaged mobilities calculated by Eq. (5.20), squares show the corresponding results obtained by averaging of inverse mobilities. Number of chains was $c = 10000$ with $N = 500$ sites each.

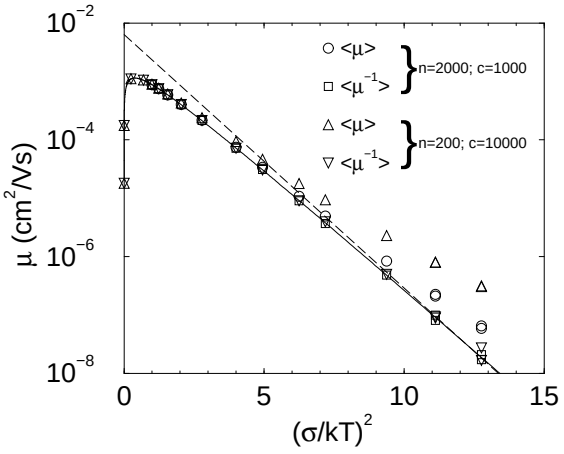

Figure 5.5: Temperature dependence of the low-field mobility for $\sigma = 50$ meV. Solid line represents the solution for the infinite chain given in Eq. (5.33). Circles and squares show the results obtained by averaging of mobilities and averaging of inverse mobilities calculated by Eq. (5.31), respectively, with averaging over $c = 1000$ chains of $N = 2000$ sites. Upward and downward triangles are the corresponding values for $c = 10000$ and $N = 200$. The dashed line indicates for illustration the temperature dependence with the slope equal to -1.

This equation is valid for the infinite chain. The corresponding temperature dependence of the low–field mobility is shown by the solid line in Fig. 5.5. The slope of $\ln \mu$ vs. $(\sigma/kT)^2$ in this curve differs slightly from -1, due to the temperature dependence of the preexponential factor in Eq. (5.31). This result is in good agreement with the recent computer simulations of Bleyl *et al.* [ble99] and with the analytic calculations of Dunlap *et al.* [dun96], although the latter analytic calculations have been carried out for correlated systems with symmetric transition rates described by Eq. (5.4). This shows that in 1D systems Eq. (5.6) with $C \simeq 1$ is correct and even stable against the choice of the form of transition rates.

The temperature dependences of the low–field drift mobility in finite systems calculated according to Eq. (5.29) are also shown in Fig. 5.5. These results are really striking. They clearly show that the temperature dependence of the mobility is related to the size of the system. This is a manifestation of the mesoscopic character of the hopping transport problem which is mostly pronounced in 1D systems. As has been already discussed with respect to the RBM, the averaging of transit times or inverse mobilities over various finite chains corresponds to the calculation of the mobility in a long system consisting of all these chains connected sequentially one after another. On the contrary, the averaging of the mobilities over various finite chains corresponds to the calculation of the carrier mobility in the system in which these chains are arranged in parallel to each other. In the latter case, the "fast" chains with

untypically short transit times strongly contribute to the averaged value of the carrier mobility and they dominate the transport of carriers. This is the very essence of the mesoscopic effects [rai91]. Having in mind an application of our results to discotic organic disordered systems where many quasi–1D current channels are connected in parallel being perpendicular to the sample surface, one should conclude that the temperature dependence of the electrical current in such systems does change with the thickness of the samples. For example, a comparison between the data obtained by the averaging of mobility values for chains with $N = 2000$ sites and chains with $N = 200$ sites suggests that for shorter chains and hence for the thinner samples the temperature dependence of the low–field drift mobility should be weaker than that for thicker samples. Of course, it would be desirable to verify our prediction experimentally.

We now turn to the question how decisive for our results is the choice of the Miller-Abrahams transition probabilities described by Eq. (5.3) and used for the above calculations. For comparison, one can insert into described mathematical apparatus symmetrical transition probabilities described by Eq. (5.4). One straightforwardly comes via Eqs. (5.21) and (5.8) to the result

$$\mu = \frac{\nu_0 b}{E} \times \frac{e^{\frac{ebE}{2kT}} e^{-\frac{\sigma^2}{4(kT)^2}}}{1 + e^{\frac{\sigma^2}{2(kT)^2}} \left[e^{\frac{ebE}{kT}} - 1\right]^{-1}} \tag{5.32}$$

In Fig. 5.6 we compare the field dependence of the mobility given by Eq. (5.32) with that for Miller-Abrahams rates. After an appropriate scaling of the results for symmetric rates the mobilities in both cases (symmetric and Miller-Abrahams hopping probabilities) are the same at low electric fields. This confirms the conclusion of Dunlap *et al.* [dun96] that the form of transition probabilities is not essential for the field dependence of the drift mobility at low fields, provided the detailed balance is fulfilled. Dunlap *et al.* [dun96] obtained this result for correlated systems (CDM), while we confirm their conclusion for the uncorrelated Gaussian model (GDM). In the non-linear regime at higher fields ($E \sim 10^6$ V/cm) deviations between the results for symmetric and for Miller-Abrahams hopping probabilities are seen in Fig. 5.6.

5.2.3 Drift mobility in the random-energy model with correlated disorder

So far we have considered the hopping transport of charge carriers along regular chains of sites with Gaussian distribution of site energies and without correlations between the spatial positions of sites and their energies. Such a model has recently been suggested by Bleyl *et al.* [ble99] for transport of charge carriers in columnar discotic liquid–crystalline glasses. Bleyl *et al.* treated this model by computer simulations

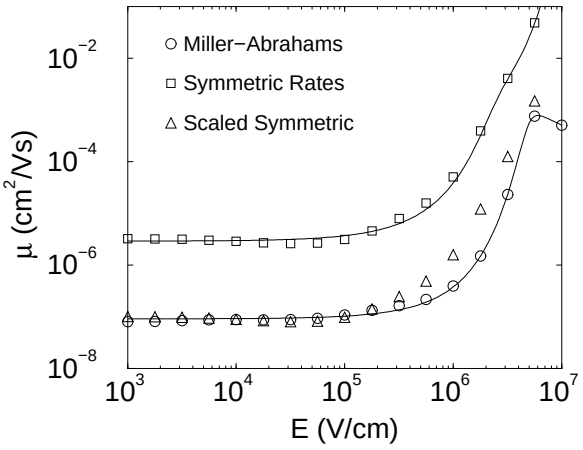

Figure 5.6: Influence of hopping rates on the field dependence of the carrier mobility. Circles show the results calculated by Eq. (5.20) with Miller–Abrahams rates defined in Eq. (5.3). Squares display the mobilities calculated with symmetric hopping rates defined in Eq. (5.4). Above data were obtained for 1000 chains each containing 500 sites. Solid lines show the corresponding analytic solutions for infinite chains. For a better comparison, triangles are plotted indicating the mobilities with symmetric hopping rates scaled by factor $\frac{1}{2}\exp[\sigma^2/(2kT)^2]$.

and obtained results similar to our exact analytic results from the previous section. We then analyzed whether or not the assumption on the uncorrelated distribution of site energies is essential for these results. Such a question was raised by Gartstein and Conwell [gar95], by Dunlap *et al.* [dun96] and by Novikov *et al.* [nov98a, nov98b]. Using a model similar to that of Gartstein and Conwell, we present below, exact analytic solutions for the drift mobility of charge carriers in systems with correlated disorder (CDM).

In order to construct a model with correlated disorder (CDM) we first generate provisional site energies ψ_k. The zero-field energy ϕ_k of a charge carrier on site k is then determined by the arithmetic average of provisional energies ψ of neighboring sites:

$$\phi_k = \lambda^{-1} \sum_{j=-m}^{m} \psi_{k+j} \tag{5.33}$$

Here $\lambda = 2m + 1$ is the correlation length in units of the intersite separation b. To ensure that the resulting site energies ϕ_k have a Gaussian distribution with variance σ we distribute energies ψ according to

$$g(\psi) = \frac{1}{\sqrt{2\pi\lambda\sigma^2}} \exp\left(-\frac{\psi^2}{2\lambda\sigma^2}\right). \tag{5.34}$$

Due to the correlations, two site energies at zero field ϕ_k and ϕ_{k+i} are not independent as long as $i \leq \lambda$. This prevents the possibility to carry out the averaging over disorder in the style as it was done above on the way from Eq. (5.20) to Eq. (5.21). Instead we have to split the sum in the second term of the denominator in Eq. (5.20) into two terms:

$$v = \frac{bN\left[1-\exp\left(-\frac{NebE}{kT}\right)\right]}{\sum\limits_{k=0}^{N-1}\frac{1}{\Gamma_{k,k+1}} + \sum\limits_{k=0}^{N-1} e^{-\frac{\phi_k}{kT}} \sum\limits_{i=\lambda}^{N-1} \frac{e^{-\frac{iebE}{kT}}}{e^{-\frac{\phi_{k+i}}{kT}}\Gamma_{k+i,k+i+1}} + \sum\limits_{k=0}^{N-1} e^{-\frac{\phi_k}{kT}} \sum\limits_{i=1}^{\lambda-1} \frac{e^{-\frac{iebE}{kT}}}{e^{-\frac{\phi_{k+i}}{kT}}\Gamma_{k+i,k+i+1}}}. \quad (5.35)$$

In the second term of the denominator the site energies ϕ_k are not correlated with site energies ϕ_{k+i} or with transition rates $\Gamma_{k+i,k+i+1}$. Hence here the averaging of $\exp(-\phi_k/kT)$ and $[\exp(-\phi_{k+i}/kT)\Gamma_{k+i,k+i+1}]^{-1}$ over disorder can be carried out separately. Inserting Eq. (5.33) into the last term of the denominator one obtains

$$\sum_{k=0}^{N-1}\sum_{i=1}^{\lambda-1} \frac{e^{-\frac{iebE}{kT}}}{\Gamma_{k+i,k+i+1}} e^{\frac{\phi_{k+i}-\phi_k}{kT}} = \sum_{k=0}^{N-1}\sum_{i=1}^{\lambda-1} \frac{e^{-\frac{iebE}{kT}}}{\Gamma_{k+i,k+i+1}} \prod_{j=1}^{i} e^{\frac{\psi_{k+m+j}-\psi_{k-m-1+j}}{\lambda kT}}. \quad (5.36)$$

With our choice of site energy correlation, Eq. (5.33), the energy difference between neighboring sites $k+i$ and $k+i+1$ is $\lambda^{-1}(\psi_{k+i+1+m} - \psi_{k+i-m})$. The transition rates $\Gamma_{k+i,k+i+1}$ are uncorrelated with ψ_{k+m+j} and $\psi_{k-m+1+j}$ for all j and the averaging for the corresponding terms can be performed independently. Note that for long-range correlations one has to average the entire product in Eq. (5.36). In the latter case Eq. (5.35) cannot be used and one has to solve Eq. (5.20) instead. This may prevent an exact solution. For correlations given by Eq. (5.33) we get

$$\mu = \frac{b}{E}\left[\left\langle\frac{1}{\Gamma_{k,k+1}}\right\rangle\left(1+\sum_{i=1}^{\lambda-1}\left\langle e^{\frac{\psi_k}{\lambda kT}}\right\rangle^i\left\langle e^{-\frac{\psi_k}{\lambda kT}}\right\rangle^i e^{-\frac{iebE}{kT}}\right) + \left\langle\frac{\left\langle\exp\left(-\frac{\phi_k}{kT}\right)\right\rangle}{\exp\left(-\frac{\phi_k}{kT}\right)\Gamma_{k,k+1}}\right\rangle\frac{\exp\left(-\frac{\lambda ebE}{kT}\right)}{1-\exp\left(-\frac{ebE}{kT}\right)}\right]^{-1}. \quad (5.37)$$

Averaging over disorder with using Gaussian distribution of site energies $g(\psi)$ given by Eq. (5.34) leads to the following result for the drift mobility of carriers in an infinite chain within the CDM

$$\mu = \frac{2\nu_0 b}{E}\left(\frac{1-e^{\frac{\sigma^2}{(kT)^2}-\frac{\lambda ebE}{kT}}}{1-e^{\frac{\sigma^2}{\lambda(kT)^2}-\frac{ebE}{kT}}}\left\{1+\mathrm{erf}\left(\frac{\sqrt{\lambda}ebE}{2\sigma}\right)\right. +$$

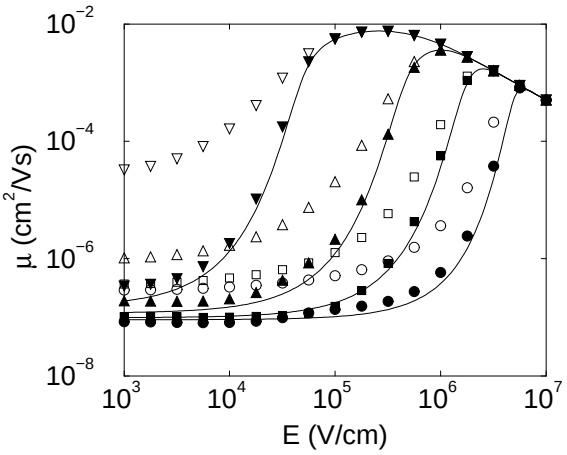

Figure 5.7: Influence of the space-energy correlations on the field dependence of the carrier mobility at $kT = 15$ meV and $\sigma = 50$ meV. The different correlation lengths are $\lambda = 1$ (circles), $\lambda = 3$ (squares), $\lambda = 11$ (upward triangles) and $\lambda = 101$ (downward triangles). Open symbols show the averaged mobilities calculated by Eq. (5.20). Solid symbols show the corresponding results obtained by averaging of the inverse mobilities for ($N = 1000, c = 1000$). Solid lines show the solutions for the infinite chain given by Eq. (5.38).

$$+ \; e^{\frac{\sigma^2}{\lambda(kT)^2} - \frac{ebE}{kT}} \left[1 + \mathrm{erf}\left(\frac{\sigma}{\sqrt{\lambda}kT} - \frac{\sqrt{\lambda}ebE}{2\sigma}\right)\right]\Bigg\} +$$
$$+ \; \frac{e^{\frac{\sigma^2}{(kT)^2} - \frac{\lambda ebE}{kT}}}{1 - e^{\frac{ebE}{kT}}} \left\{1 + \mathrm{erf}\left(\frac{\sigma}{\sqrt{\lambda}2kT} + \frac{\sqrt{\lambda}ebE}{2\sigma}\right) + \right.$$
$$\left. + \; e^{-\frac{ebE}{kT}} \left[1 + \mathrm{erf}\left(\frac{\sigma}{\sqrt{\lambda}2kT} - \frac{\sqrt{\lambda}ebE}{2\sigma}\right)\right]\right\}\Bigg)^{-1}. \qquad (5.38)$$

In Fig. 5.7 the corresponding field dependences are plotted for different correlation lengths λ for finite chains (symbols) as calculated via Eqs. (5.20), (5.8) and for the infinite chain [Eq. (5.38)]. The particular shape of the field dependence of the drift mobility in the CDM for the infinite system has been already discussed in detail by Gartstein and Conwell [gar95], by Dunlap *et al.* [dun96] and by Novikov *et al.* [nov98a, nov98b]. We would like to focus our attention here on the other aspect of the phenomenon, namely, on the increasing difference between the results obtained by averaging of mobilities and those obtained by averaging of inverse mobilities in finite systems with increasing correlation length. This trend is clearly related to the smaller number of high barriers for charge carriers in systems with longer correlation lengths. The mesoscopic effects become more pronounced in systems with longer correlation length. The increase of the correlation length in the CDM is analogous to the decrease of the total number of sites in the chain in the GDM.

5.2.4 Concluding remarks

Analytic calculations were presented for the hopping drift mobility of charge carriers in a one–dimensional regular chain of localization sites with energetic disorder. Exact results were obtained for temperature and field dependences of the mobility in systems with uncorrelated disorder (GDM) and those with a correlated disorder (CDM) for both asymmetrical and symmetrical transition probabilities. These dependences are shown to be determined by the length of the system. Therefore even the exact solutions usually obtained for infinite systems might be of low value for thin samples which are used in real devices. Focusing on the description of the transport properties of the discotic liquid–crystalline glasses, one should take into account that the real device samples usually contain only 50 to 100 sites [chr97b]. For such systems one should use the theoretical results obtained in this report for finite systems and not those derived for infinite chains.

In this section we considered only transitions of charge carriers to the nearest sites on a conducting chain. In the next section (section 5.3) it is shown by a Monte Carlo computer simulation that in a correlated system (CDM) transitions to more distant neighbors do not play an essential role while for uncorrelated systems such distant transitions can be important. Hence in the CDM our analytical results can be definitely considered as exact. In the case of uncorrelated disorder (GDM), longer electron hops can modify the results for the field and the temperature dependences of the carrier drift mobility as shown in section 5.3.

5.3 Monte Carlo simulations

In section 5.2 analytic calculations were carried out for the steady-state drift mobility of charge carriers in one-dimensional systems with taking into account hopping transitions only between the nearest localized states. Special attention was paid to the temperature and field dependences of the mobility for various hopping models. We check here the corresponding results by a Monte Carlo computer simulation and show that analytic theory works perfectly. However, this theory is unable to take into account hopping events to localized states situated further in space than the nearest-neighboring sites. We will show below that electron transitions to more distant sites decisively influence the most fundamental transport properties, such as, for example, the temperature dependence of the drift mobility. This dependence at low electric fields is described by Eq. (5.6). Such a dependence is observed experimentally and it has also been obtained in computer simulations and analytic calculations. In the three-dimensional (3D) case, coefficient C in Eq. (5.6) is believed to have the magnitude [bäs93] $C \approx 2/3$, while in the one–dimensional (1D) case the value $C \approx 1$ has been obtained for symmetric transition rates determined by Eq. (5.4) [dun96]. Equa-

tion (5.6) is widely used to determine parameter σ of the density of states (DOS) in Eq. (5.1) for various materials from experimental measurements of the $\ln(\mu)$ vs. $(1/T)^2$ dependences, in particular for the 1D hopping transport [och99a, ble99]. Therefore, the magnitude of the coefficient C is really important. This coefficient C in Eq. (5.6) cannot be universal. Equation (5.2) shows that both the energy difference between localized states involved in the carrier jump and the distance between these states determine the hopping probability. In such processes, characteristic temperature T_0 should depend on the concentration of localized states N and on the decay length of the carrier wave function in the localized states α in the combination $N\alpha$ in the 1D case and $N\alpha^3$ in the 3D case [shk84]. In the computer simulations [sch81] this parameter was taken as $N\alpha^3 = 0.001$ and it is not surprising that some particular value for coefficient C was obtained. A very close value $C \approx 2/3$ was also obtained by the effective-medium theory in the 3D case [gru84, mov86]. It is not correct to use this value for 1D systems. Concentrating on the 1D transport we emphasize that the value of the coefficient $C = 1$ obtained in the analytic calculation for Miller-Abrahams transition rates and also known from the literature for symmetric rates [dun96] can also be wrong. This value was obtained only for the nearest-neighbor hopping. Below we show that in systems with uncorrelated energetic and spatial distributions of localized states, hopping transitions to more distant sites than the nearest neighbors influence the value of the coefficient C, which is decisive for determination of the disorder parameter σ of the DOS for various materials from experimental measurements of the $\ln(\mu)$ vs. $(1/T)^2$.

5.3.1 Numerical algorithm and simulation details

In our simulations a Gaussian density of states (DOS) was assumed following the data from the literature [bäs93, dun96, och99a, ble99]. In the so-called Gaussian disorder model (GDM), the energy distribution was described by Eq. (5.1) and no correlations between energy and space positions of localized states were allowed. In the so-called correlated disorder model (CDM) [dun96, gar95, nov98a], the site energies were correlated with energies of neighboring sites. We used correlations described by Eqs. (5.33, 5.34) with m equal to 1. In the simulation procedure, c independent regular chains of localization sites, each chain containing N sites were studied simultaneously. Only one particle was considered on each chain. The simulation algorithm was the following. A charge carrier starts its motion on the beginning site of a chain (site number 1). The simulations were stopped after 90% of carriers reached the final sites of the chains (sites number N). The rate Γ_{ij} of a hopping transition from an occupied site i to an empty site j were determined by Miller-Abrahams equation (Eq. 5.2). The lifetime of a carrier at a site i was calculated as

$$t_i = \frac{\ln(x)}{\sum_j \Gamma_{ij}} \tag{5.39}$$

where x is a random number from the uniform random-number distribution between 0 and 1. The sum in Eq. (5.39) was taken over sites with numbers $j = i \pm 1$ for nearest-neighbor hopping and $j = i \pm 1, i \pm 2, i \pm 3, i \pm 4, i \pm 5, i \pm 6$ for simulations with tunneling to further neighbors.

For the fastest 10% of particles two different methods to calculate the mobility were used. In the first method, transition times for different chains were averaged and the obtained value $\langle t \rangle_{10\%}$ was used to calculate the carrier mobility via relation $\mu_{10\%}^{tav} = \frac{d}{E\langle t \rangle_{10\%}}$, where d is the length of the chains and E is the strength of the applied electric field. The other method was based on the calculation of carrier mobilities for the fastest 10% of carriers and on averaging the mobility values. The latter method in our simulations is equivalent to the averaging of the inverse transit times $\langle 1/t \rangle_{10\%}$. The averaged mobility in this method was calculated as $\mu_{10\%}^{mobav} = \frac{d\langle 1/t \rangle_{10\%}}{E}$. The same averaging procedures were performed for the 90% of charge carriers with finding the corresponding quantities $\mu_{90\%}^{tav} = \frac{d}{E\langle t \rangle_{90\%}}$, and $\mu_{90\%}^{mobav} = \frac{d\langle 1/t \rangle_{90\%}}{E}$.

Simulations were carried out for various magnitudes of the electric field E and temperature T. In order to obtain the value of the zero-field mobility μ_{zf}, the procedure suggested by Bleyl *et al.* [ble99] has been used. The data were plotted in the Poole-Frenkel (PF) representation

$$\ln(\mu) = \ln(\mu_{zf}) + \gamma\sqrt{E} \tag{5.40}$$

with the aim of finding μ_{zf} via extrapolation to zero field. To illustrate this extrapolation procedure, we show some of our results in Fig. 5.8. These particular results were obtained for the GDM with the energy scale of the DOS $\sigma = 30$ meV and the temperature range corresponds to kT between 10 meV and 30 meV. The mobility values were obtained by averaging of the inverse transit times for 90% of charge carriers. After having found μ_{zf} for various temperatures, the T dependence of this quantity was plotted as

$$\mu_{zf}\left(\frac{\sigma}{kT}\right) = \mu_0 \exp\left[-\left(C\frac{\sigma}{kT}\right)^2\right] \tag{5.41}$$

where μ_0 is a temperature-independent prefactor and C is a constant to be determined from such plots.

Obtained temperature dependence described by Eq. (5.41) is plotted in Fig. 5.9 illustrating some of our data obtained for the nearest-neighbor hopping in the GDM. A similar Monte Carlo simulation was carried out recently by Bleyl *et al.* [ble99], who obtained very similar results. Our data confirm the coefficient $C \approx 0.9$ in Eq.

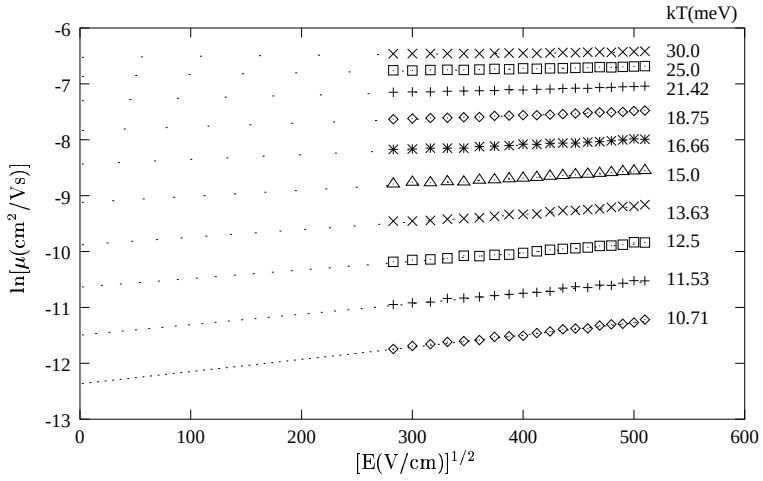

Figure 5.8: Field dependences of the carrier mobility at various temperatures in the Poole-Frenkel representation for the GDM with $\sigma = 30$ meV.

(5.41) obtained earlier by Bleyl *et al.* However, computer simulations of the nearest-neighbor hopping are not of considerable interest, as exact results for such processes can be obtained analytically for finite and infinite systems as previously shown in the analytical work (section 5.2). Hopping processes to further neighbors than the nearest ones can hardly be treated exactly by analytic theories. In this section we use computer simulations to study whether such distant hopping transitions are important for transport coefficients, like the drift mobility, or not.

In order to answer this question, we performed computer simulations of hopping processes to distant neighbors for both GDM and CDM and compared the results with those obtained only for hopping to the nearest neighbors. The results for the latter are given in section 5.3.2, while the results for distant hops are presented in section 5.3.3. Also the question will be addressed on the significance of the space-energy correlations for transport processes as given by the comparison of the results for the GDM and CDM. The latter question has recently been studied with respect to the dependence of the carrier drift mobility on the electric field [dun96, gar95, nov98a, nov98b] and it was shown that the space-energy correlations play an essential role for the field dependence of the mobility. Below we mainly consider the temperature dependence of the carrier mobility. The quantity of our main interest will be the coefficient C in Eq. (5.41). Before presenting the results, we would like to note that the extrapolation procedure according to Eq. (5.40) cannot be exact. We have found that the results for μ_{zf} can slightly depend (by less than 10%) on the chosen range of field strengths used for extrapolation. We always used the interval $9 \times 10^4 \leq E \leq 2.5 \times 10^5$ V/cm where the PF dependence seems to be valid as shown in Fig. 5.8. Moreover, the values

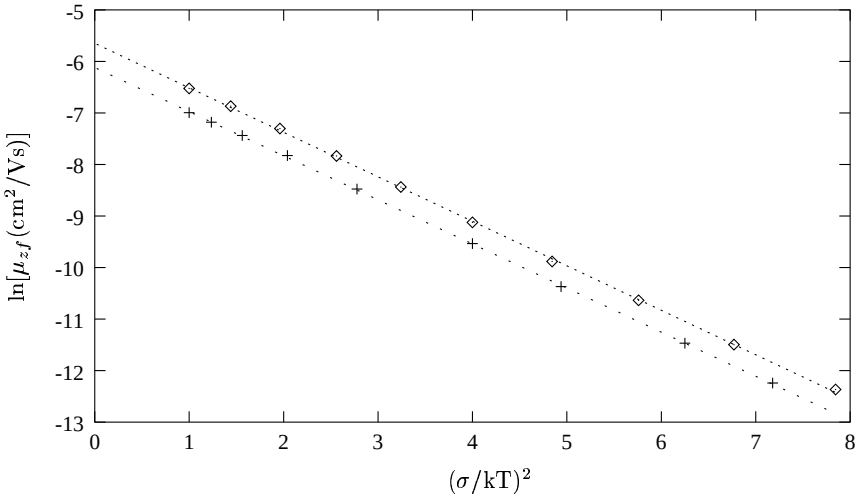

Figure 5.9: Temperature dependence of the zero-field drift mobility according to Eq. (5.41) for the GDM with $\sigma = 30$ meV (diamonds) and $\sigma = 50$ meV (crosses). Dashed and dotted lines represent Eq. (5.41) with $C = 0.928$ and $C = 0.924$ respectively.

of the determined coefficient C (by less than 10%) depend slightly on the way how parameter σ/kT was changed – by changing T with fixed σ, or by changing σ at fixed T. This is caused by the extrapolation procedure based on Eq. (5.40), because T and σ determine the field dependence of the carrier drift mobility not in the combination σ/kT which is essential for the temperature dependence of the zero-field mobility as has been clearly shown by Dunlap *et al.* [dun96]. Therefore, not the absolute values of the coefficient C, but its trends with changing the simulation parameters will be of most interest with respect to our simulation results.

5.3.2 Nearest neighbor hopping

All simulation results given below were averaged over $c = 1000$ chains, each containing $N = 2000$ sites. Following Bleyl *et al.* [ble99] only Miller–Abrahams transition rates determined by Eq. (5.3) were used. Parameters $\Gamma_1 = 1.875 \cdot 10^{14} s^{-1}$, $b = 3.6$ Å, $\alpha = 1$ Å were chosen, where b is the distance between the neighboring sites. As long as only the nearest-neighbor hopping is considered, the choice of parameters b and α cannot influence the temperature dependence of the mobility which is of prime interest in our study. In order to illustrate the simulation results, we plot in Fig. 5.10 the field dependence of the drift mobility at $kT = 25$ meV and $\sigma = 50$ meV for both GDM and CDM. Results of our computer simulation are shown by crosses for the CDM and by diamonds for the GDM. Dashed lines represent the results of the exact analytic calculations for the particular chains used in the simulation procedure

based on the methods described in section 5.2. Excellent agreement with the exact analytic results confirms the validity of our simulation procedure. In agreement with previous calculations [dun96, gar95, nov98a], one can see in Fig. 5.10 that the mobility values are higher and the field dependence starts at lower fields for the CDM than for the GDM. We also present in Fig. 5.10 the statistics for the average number of hops necessary for a carrier to penetrate through a chain containing 2000 sites. At low fields, the motion is diffusive and the number of hops is enormously larger than the number of sites indicating that charge carriers often move back and forth. This supports the conclusion of analytical calculations (section 5.2) that at low fields one should use the diffusion equation [Eq. (5.11)] rather than the drift approach [Eq. (5.9)]. Erroneous application of Eq. (5.9) at low fields leads to the artificial increase of mobility values with decreasing field strength. Unfortunately, this artifact is often treated as a true physical effect. At very high fields, the carriers mostly hop in the direction prescribed by the field as indicated by the equality between the number of hops necessary for charge carrier to penetrate through the chain and the number of chain sites ($N = 2000$). In such extreme conditions, the drift velocity does not depend on the field strength and Eq. (5.8) leads to the relation $\mu \propto 1/E$ for high fields. Performing the extrapolation and fitting procedure described in section 5.3.1, we obtained the values for the coefficient C in various conditions. These values were obtained by the four different averaging methods described in section 5.3.1. In the following, $C_{10\%}^{tav}$ for example, will denote the coefficient C corresponding to fastest 10% of charge carriers (i.e., "fastest" 10% chains) and "tav" means that the values were obtained by averaging of arrival times. Values for the coefficients μ^{mobav} were correspondingly obtained via the averaging of mobilities. Obtained results are gathered in Table 5.1, where different horizontal lines correspond to simulation results at different values of the disorder parameter σ in Eq. (5.1). Temperature values were changed so that parameter σ/kT had magnitudes between 1 and 3. In all cases, the values of the coefficient C are between 0.9 and 1, in good agreement with the results of previous computer simulations [ble99] and analytical calculations [dun96] (see also the analytical solution in section 5.2). No striking difference concerning the temperature dependence of the carrier drift mobility has been found between the GDM and CDM as can clearly be seen from Table 5.1.

5.3.3 Hopping with tunneling to further neighbors

In the previous section as well as in the analytical calculations (section 5.2), only transitions of charge carriers to the nearest-neighboring sites were considered. In such conditions, transition rates are determined by Eq. (5.3). Now we would like to check whether and at what conditions, if at all, the tunneling hops to further sites than the nearest neighbors influence the transport coefficients. In order to answer this question we repeated all simulations described in section 5.3.2, but this time al-

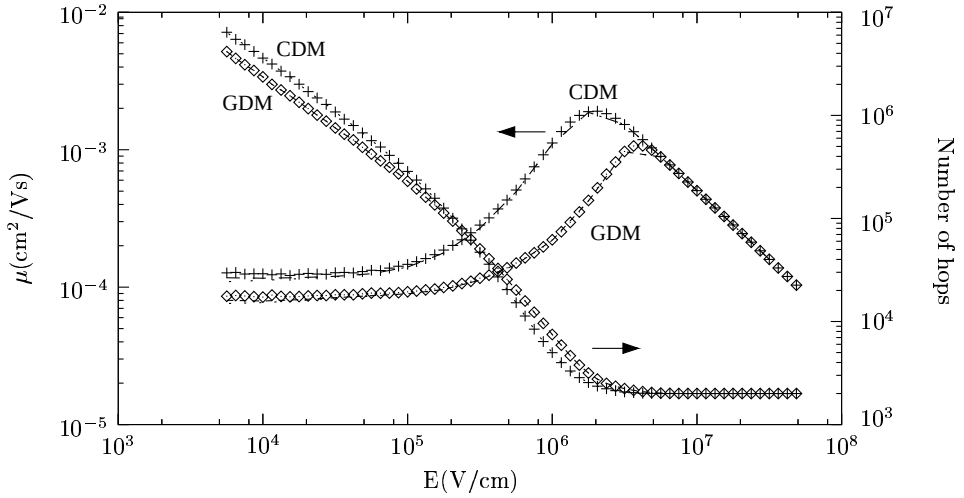

Figure 5.10: Left axis: dependences of the carrier mobility $\mu_{90\%}^{tav}$ on the electric field for the GDM and CDM. The lines show the results of the exact analytic solutions for system parameters $\sigma = 50$ meV and $kT = 25$ meV; right axis: average numbers of forward steps as functions of electric field. The chain length was equal to 2000 sites in all simulation runs.

Table 5.1: Coefficients C in Eq. (5.41) for the nearest-neighbor hopping.

model	parameter	$C_{10\%}^{tav}$	$C_{10\%}^{mobav}$	$C_{90\%}^{tav}$	$C_{90\%}^{mobav}$
GDM	$\sigma = 30meV$	0.89	0.89	0.95	0.93
	$\sigma = 40meV$	0.90	0.89	0.95	0.93
	$\sigma = 50meV$	0.90	0.90	0.94	0.92
CDM	$\sigma = 28.867meV$	0.92	0.92	0.99	0.96
	$\sigma = 40meV$	0.92	0.92	0.98	0.96
	$\sigma = 50meV$	0.91	0.91	0.96	0.94

lowing the tunneling of charge carriers to further sites. For such distant hops explicit $R-$dependent transition probabilities described by Eq. (5.2) should be taken into account instead of the simplified probabilities described by Eq. (5.3). Moreover, we carried out all simulations with changing the values of parameter α which determines the decay length of the carrier wave function in the localized states. The intersite distance was kept constant $b = 3.6$ Å, the values of α were changed between 1 Å and 3 Å. Transitions to six neighbors in each direction were allowed in the simulation procedure. We have checked that tunneling to further states than these 12 neighbors does not play any role at all sets of parameters used in the simulation runs. Results obtained for coefficient C in Eq. (5.41) at various values of α and σ and for various averaging procedures are gathered in Table 5.2. The main conclusion one can draw from this table is the following. For the CDM, i.e., for a system with correlated disorder, tunneling to further sites than the nearest neighbors do not play any essential role, while for the GDM, i.e., for uncorrelated systems these distant hopping transitions slightly influence the transport coefficients. The insignificance of distant transitions for systems with correlated disorder is unsurprising. In such systems, energies of neighboring sites are close to each other due to correlation effects. Thus the variable-range hopping is not significant for such systems, because the closest in energy and space states are chosen by carriers in their motion and these states are the nearest neighbors. The quantitative confirmation of this qualitatively clear statement is of great importance because it implies that for systems with correlated disorder one can use analytic theories described in section 5.2 and one can be sure that the restriction of the analytic theory which considers only the nearest-neighbor hopping is not at all essential for the obtained results.

For systems with uncorrelated disorder the situation is also rather optimistic with respect to the exact analytic solutions (see section 5.2). From Table 5.2 it can be seen that even for rather high value of the decay constant $\alpha = 2$ Å which makes the distant hops very favorable, the value of coefficient $C \approx 0.8$ is not that dissimilar from its value $C \approx 0.9$ for the nearest-neighbor hopping. Thus even for systems with uncorrelated disorder, exact analytic solutions (see section 5.2) taking into account only the nearest-neighbor hopping give reasonable values for transport coefficients.

5.3.4 Concluding remarks

Computer simulations of charge carrier transport in disordered 1D systems show that for systems with correlated space-energy disorder the variable-range hopping does not play an essential role, implying that exact analytic solutions (section 5.2) based on the nearest-neighbor hopping are valid for such systems without any restrictions. For systems with uncorrelated disorder the analytic results for transport coefficients from section 5.2 can be considered as an approximation. For example, taking into account the more distant hops than hops to the nearest neighbors one obtains the value of

Table 5.2: Coefficients C in Eq. (5.41) when taking into account further hopping transitions than those to the nearest-neighboring sites.

model	parameter	α(Å)	$C_{10\%}^{tav}$	$C_{10\%}^{mobav}$	$C_{90\%}^{tav}$	$C_{90\%}^{mobav}$
GDM	$\sigma = 30meV$	1.0	0.86	0.86	0.92	0.89
		2.0	0.79	0.79	0.86	0.82
		3.0	0.75	0.75	0.83	0.79
	$\sigma = 40meV$	1.0	0.87	0.87	0.92	0.90
		2.0	0.79	0.79	0.84	0.82
		3.0	0.74	0.74	0.79	0.77
	$\sigma = 50meV$	1.0	0.85	0.84	0.91	0.87
		2.0	0.77	0.77	0.82	0.80
		3.0	0.73	0.73	0.78	0.76
CDM	$\sigma = 28.867meV$	1.0	0.93	0.93	1.00	0.97
		2.0	0.91	0.91	0.98	0.96
		3.0	0.88	0.88	0.96	0.93
	$\sigma = 40meV$	1.0	0.92	0.92	0.98	0.95
		2.0	0.90	0.89	0.96	0.94
		3.0	0.87	0.87	0.93	0.91
	$\sigma = 50meV$	1.0	0.92	0.92	0.97	0.95
		2.0	0.89	0.89	0.95	0.93
		3.0	0.87	0.87	0.92	0.90

the coefficient C in Eq. (5.41) by approximately 10% different to that for only the nearest-neighbor hopping. With such an accuracy one can even use analytic results from section 5.2 for systems with uncorrelated disorder.

Bibliography

[abk92] M. A. Abkowitz, Phil. Mag. B **65**, 817 (1992).

[bac97] A. Bacher, I. Bleyl, C.H. Erdelen, D. Haarer, W. Paulus, and H.-W. Schmidt, Adv. Mater. **9**, 1031 (1997).

[bäs93] H. Bässler, phys. stat. sol.(b) **175**, 15 (1993).

[ble99] I. Bleyl, C. Erdelen, H.-W. Schmidt, and D. Haarer, Phil. Mag. B **79**, 463 (1999).

[bod95] N. Boden, R.J. Bushby, J. Clements, B. Movaghar, K.J. Donovan, and T. Kreouzis, Phys. Rev. B **52** 13274 (1995).

[chr97a] T. Christ, B. Glüsen, A. Greiner, A. Kettner, R. Sander, V. Stümpflen, V. Tsukruk, and J.H. Wendorff, Adv. Mater. **9**, 48 (1997).

[chr97b] T. Christ, F. Geffart, B. Glüsen, A. Kettner, G. Lüssem, O. Schäfer, V. Stümpflen, J. H. Wendorff and V. V. Tsukruk, Thin Solid Films **302**, 214 (1997).

[cor01] H. Cordes, S.D. Baranovskii, K. Kohary, P. Thomas, S. Yamasaki, F. Hensel, and J−H. Wendorff, Phys. Rev. B **63**, 094201 (2001).

[der83] B. Derrida, J. Stat. Phys. **31**, 433 (1983).

[dun96] D.H. Dunlap, P.E. Parris, and V.M. Kenkre, Phys. Rev. Lett. **77**, 542 (1996).

[gar95] Yu. N. Gartstein and E. M. Conwell, Chem. Phys. Lett. **245**, 351 (1995).

[gru84] M. Grünewald, B. Pohlmann, B. Movaghar, and D. Würtz, Phil. Mag. B **49**, 341 (1984).

[gil97] O. Hilt and L.D.A. Siebbeles, Chem. Phys. Lett. **269**, 257 (1997).

[keh96] K. W. Kehr and T. Wichmann, cond-mat/9602121 (1996); K. Mussawisade, T. Wichmann and K. W. Kehr, cond-mat/9610191 (1996).

[koh01] K. Kohary, H. Cordes, S.D. Baranovskii, P. Thomas, S. Yamasaki, F. Hensel, and J−H. Wendorff, Phys. Rev. B **63**, 094202 (2001).

[mil60] A. Miller and E. Abrahams, Phys. Rev. **120**, 745 (1960).

[mov86] B. Movaghar, M. Grünewald, B. Ries, H. Bässler, and D. Würtz, Phys. Rev. B **33**, 5545 (1986).

[mur90] K. P. N. Murthy and K. W. Kehr, Phys. Rev. A **40**, 2082 (1989); Erratum *ibid.* **41**, 1160 (1990).

[ném96] Á. Németh-Buhin, C. Juhasz, V.I. Arkhipov, and H. Bässler, Phil. Mag. Lett. **74**, 295 (1996).

[nov98a] S.V. Novikov, D.H. Dunlap, V.M. Kenkre, P.E. Parris, and A.V. Vannikov, Phys. Rev. Lett. **81**, 4472 (1998).

[nov98b] S.V. Novikov, D.H. Dunlap, and V.M. Kenkre, Proc. SPIE **3471**, 181 (1998).

[och99a] A. Ochse, A. Kettner, J. Kopitzke, J.H. Wendorff, and H. Bässler, Phys. Chem. Chem. Phys. **1**, 1757 (1999).

[och99b] A. Ochse, PhD Thesis, Marburg, 1999.

[pel88] A. Peled and L.B. Schein, Chem. Phys. Lett. **153**, 422 (1988).

[rai91] M.E. Raikh and I. Ruzin, in "Mesoscopic Phenomena in Solids", Eds. B.L. Altshuler, P.A. Lee, and R.A. Webb (North Holland, Amsterdam, 1991).

[sch92] L.B. Schein, Phil. Mag. B **65**, 795 (1992).

[sch81] G. Schönherr, H. Bässler, and M. Silver, Phil. Mag. B **44**, 369 (1981).

[shk84] B.I. Shklovskii and A.L. Efros, Electronic Properties of Doped Semiconductors (Heidelberg, Springer 1984)

Summary

The study of different physical properties of disordered systems by means of computer simulations was the aim of the present thesis. The incredibly huge and fast growing advances in information technology in the last decades, has allowed physicists to use computer resources more effectively. The extensive use of computers has enabled the development of a new and extensive part of physics, lying somewhere between experimental and theoretical physics.

In order to describe the physical properties of amorphous materials it is very important that one has knowledge of the atomic arrangement. The structure of disordered solids usually depends on their preparation method. It is therefore important that the preparation method is modeled first, following this, the received structures need to be studied. In chapter 2, low energy molecular dynamics simulations of atomic beam growth of amorphous carbon on a diamond [111] surface were carried out. Our aim was to construct large scale amorphous carbon models over 100 atoms by the quantum-mechanical treatment of the interatomic potential. The interactions were described by a well-tested and widely applied tight-binding potential. The structures were grown by atom-by-atom deposition onto substrates. The growth process was simulated as in experiments without any artificial model of energy dissipation. We used two different average bombarding energies E_{beam} = 1 and 5 eV, and two different substrate temperatures T_{sub} = 100 and 300 K for 30 ps simulation time. The simulations were prolonged by 15 ps at T_{sub} = 100 K to obtain larger structures. Six networks were prepared by the deposition technique with periodic boundary conditions in two dimensions. The most important structural parameters, like densities, radial distribution functions, coordination numbers, bond angle distributions, and ring statistics were then analyzed. The deposition rate was much higher than it is in experiments. On the basis of our time development investigation we are certain that much lower deposit rates would not cause a significant difference in our models. Our lower substrate temperatures, compared to experiments, provide a quicker energy dissipation which slightly compensates for the high deposition rate.

In chapter 3, we simulated the atomistic simulation of the bombardment process during the bias enhanced nucleation (BEN) phase of diamond chemical vapor deposition (CVD). Special attention was paid to the study of different hydrocarbon (C_xH_y)

projectile bombardment at varying impact energies. The simulations showed that larger kinetic energies produce deeper subplantations and that it is more probable that the species will be dissociated. For acetylene (C_2H_2) the carbon-carbon bond is almost never broken at low energies (20, 40 eV) and it is broken in 50 to 90% of cases with larger energies (80 eV). The computer experiments manifested that approximately 60% of the projectile hydrogen-carbon bonds are broken during the subplantation. Usually, one of the hydrogen-carbon bonds is not broken for methyl (CH_3) and the other two hydrogens form H_2 molecules. At the typical 200 V bias voltage, which is optimal for diamond nuclei formation in BEN, the C_2H_2 projectiles have 80 eV, and CH_3 ion species have 40 eV kinetic energy. There are significant differences in the structural rearrangements in the film caused by these two projectiles at this voltage. For the C_2H_2 species, the penetration is deeper and these projectiles cause changes in the deeper region than is the case with the CH_3 species. The CH_3 projectiles do not contribute to the deep variations in the film and cause structural rearrangements only in the surface regions. The structural changes in the film showed that higher kinetic energy ionic species under the average deposition depth generate a thicker sp^3 rich film and the surface mostly consists of atoms with sp^2 hybrids. The border between these two regimes move downwards with larger deposition energies. The results support the subplantation model. In the future it would be a very interesting task to do simulations over a silicon substrate and study the effect of this crystalline layer on the formation of diamond nuclei in the amorphous carbon film.

Chapter 4 deals with the simulation of amorphous silicon structures. The same atomic deposition program code, which had been developed for studying the amorphous carbon structure growth and was reported in chapter 2, was applied here for silicon. We used a well tested tight-binding Hamiltonian to describe the interatomic interaction between silicon atoms. A similar tight-binding potential was developed by the same group for carbon systems and we successfully applied it for the description of the amorphous carbon growth (see chapter 2). Nine different amorphous silicon structures were obtained by our deposition computer method. An additional tenth model was prepared by rapid cooling in order to check the difference between atom-by-atom deposition on substrate and melt-quenching preparation techniques. The most significant difference we have found between the models prepared in different conditions, is in the ring statistics, i.e. in the medium range order. Triangles are also present in the atomic arrangement, supporting three other independent pieces of evidence into the existence of triangles in amorphous silicon structures. Nevertheless, the fragments like equilateral triangles have never been considered at electronic density of states calculations or at an unsolved problems such as the breaking of weak bonds by prolonged illumination, which is the major mechanism for the light-induced defect creation. The tight-binding model potential used in our computer experiments slightly overestimates the bond distances, by giving values which were observed previously in

liquid silicon forms. The potential gives overcoordinated atomic sites (fivefold, and even sixfold coordinated atoms) during the amorphous silicon structure simulations. The sixfold coordinated atoms can be found in the liquid phase of silicon instead of in the amorphous structure. The well-known Stillinger-Weber classical empirical potential for amorphous silicon had a similar difficulty and has recently been successfully modified. A possible future aim would be to improve this tight-binding potential by a similar process.

Finally, in chapter 5, calculations for the hopping drift mobility of charge carriers in a one–dimensional regular chain of localization sites with energetic disorder were performed. In the analytic calculations, exact results were obtained for temperature and field dependences of the mobility in systems with uncorrelated disorder (Gaussian Disordered Model) and those with a correlated disorder (Correlated Disorder Model) for both asymmetrical and symmetrical transition probabilities. These dependences are shown to be determined by the length of the system. Therefore even the exact solutions usually obtained for infinite systems might be insignificant for thin samples which are used in real devices. Focusing on the description of the transport properties of the discotic liquid–crystalline glasses, one should take into account that the real device samples usually contain only 50 to 100 sites. For such systems one should use the theoretical results obtained in section 5.2 for finite systems and not those derived for infinite chains. In analytic calculations we considered only transitions of charge carriers to the nearest sites on a conducting chain. The results of Monte Carlo computer simulation reveal that for systems with uncorrelated space-energy disorder, the variable-range hopping plays an important role. Longer electron hops can modify the results for the field and temperature dependences of the carrier drift mobility as presented in section 5.3. For such systems the analytic results for transport coefficients can be considered as an approximation. Taking into account, for example, the more distant hops than hops to the nearest neighbors one obtains the value of the coefficient C, which describes the temperature dependence of mobility value in Eq. (5.41), which is approximately 10% different to that for only the nearest-neighbor hopping. With such accuracy one can even use analytic results (from section 5.2) for systems with an uncorrelated disorder. However, in the case of correlated space-energy disorder, this effect is much lower, implying that exact analytic solutions based on the nearest-neighbor hopping are valid for such systems without any restrictions.

Zusammenfassung

Ziel dieser Dissertation war die Untersuchung verschiedener physikalischer Eigenschaften von ungeordneten Systemen mit Hilfe von Computer Simulationen. Die überwältigend schnell gewachsenen Entwicklungen in der Informationstechnologie in den letzen Jahrzehnten hat es ermöglicht, Computer Ressourcen effektiver als je zuvor zu nutzen. Die ausgdehnte Nutzung von Computern hat eine neues und umfangreiches Gebiet der Physik hervorgebracht, das irgendwo zwischen experimenteller und theoretischer Physik liegt.

Die Kenntnis der atomaren Struktur ist sehr wichtig um die physikalischen Eigenschaften amorpher Materialien zu verstehen. Die Strukturen ungeordneter Festkörper hängen normalerweise von ihren Präparationsmethoden ab. Daher is es wichtig, die Präparation zuerst zu modellieren. Dadurch können die resultierenden Strukturen ermittelt werden. In Kapitel 2 wurden Niedrigenergie Molecular-Dynamic Simulationen von Atomstrahlwachstum von amorphem Kohlenstoff auf einer Diamant [111] Oberfläche durchgeführt. Unser Ziel war es, Modelle von amorphem Kohlenstoff mit über 100 Atomen mit einer quantenmechanischen Behandlung des interatomaren Potentials zu erhalten. Als Wechselwirkung wurde ein wohlgetestetes und weitbenutztes tight-binding Potential verwendet. Die Strukturen wurden durch atomweise Anlagerung auf dem Substrat gewachsen. Der Wachstumsprozess wurde dem Experiment entsprechend ohne die Annahme einer künstlichen Energiedissipation simuliert. Wir haben zwei unterschiedliche mittlere Atomstrahlenergien E_{beam} = 1 und 5 eV benutzt, und auch zwei veschiedene Substrattemperaturen T_{sub} = 100 und 300 K für eine Simulationszeit von 30 ps. Die Simulationen wurden um 15 ps bei T_{sub} = 100 K verlängert um größere Strukturen herzustellen. Es wurden sechs Netzwerke in zwei Dimensionen mit periodischen Randbedingungen durch diese Depositionstechnik erzeugt. Anschließend wurden die wichtigsten strukturellen Parameter, wie die Dichten, radialen Verteilungsfunktionen, Koordinationszahlen, die Verteilungsfunktionen der Bindungswinkel und Ringstatistiken analysiert. Die Depositionsgeschwindigkeit war größer als in den Experimenten. Auf Grund unserer Untersuchung zur zeitlichen Entwicklung sind wir sicher, daß eine niedrigere Geschwindigkeit der Anlagerung keine wesentlichen Unterschiede in unseren Modellen verursachen würde. Unsere niedrigeren Substrattemperaturen verglichen mit

den Experimenten stellen ein schnellere Energiedissipation sicher, die die hohe Depositionsgeschwindingkeit einigermaßen kompensiert.

In Kapitel 3, haben wir die atomistische Simulation des Chemical-Vapor-Depositionsprozesses während der Phase der bias-enhanced nucleation (BEN) von Diamant durchgeführt. Besonderes Augenmerk wurde auf die Untersuchung des Projektilbeschusses mit verschiedenen Hydrokarbonaten (C_xH_y) bei unterschiedlichen Energien gerichtet. Die Simulationen zeigten, daß großere kinetische Energien tiefere Subplantationen zur Folge haben und daß es wahrscheinlicher wird, daß diese Spezies dissoziert werden. Für Azetylen (C_2H_2) wird die Kohlenstoff-Kohlenstoff Bindung fast nie bei niedrigen Energien (20, 40 eV) gebrochen. Sie wird andererseits in 50 bis 90% der Fälle für größere Energien (80 eV) gebrochen. Die Computer Experimente offenbarten, daß ungefähr 60% der Wasserstoff-Kohlenstoff Bindungen der Projektile während der Subplantation gebrochen werden. Normaleweise wird bei Methyl (CH_3) eine der Wasserstoff-Kohlenstoff Bindungen nicht gebrochen und die anderen beiden formen H_2 Moleküle. Bei einer typischen bias-Spannung von 200 V, die optimal für die Formation von Diamantkeimen in BEN ist, haben die C_2H_2 Projektile 80 eV und die CH_3 Ionspezies 40 eV kinetische Energie. Es gibt bedeutensvolle Unterschiede in den strukturellen Umordungen der Filme, die von den beiden Projektilen bei dieser Spannung verursacht wurden. Für die C_2H_2 Spezies ist die Durchdringung tiefer und diese Projektile sind verantwortlich für die Änderungen in tiefern Regionen als es der Fall mit den CH_3 Spezies ist. Die CH_3 Projektile tragen nicht zu Änderungen in tiefen Lagen der Filme bei und verursachen strukturelle Änderungen nur an der Oberfläche. Die strukturellen Änderungen in den Filmen deuten darauf hin, daß Spezies mit hoher kinetischer Energie einen dickeren sp^3-reichen Film unterhalb der mittleren Depositionstiefe erzeugen und daß die Oberfläche aus Atomen mit sp^2 Hybriden besteht. Die Grenze zwischen diesen beiden Regionen bewegt sich mit größerer Depositionsenergie nach unten. Diese Ergebnisse unterstützen das Modell der Subplantation und deuten darauf hin, daß sp^3 Hybride unter der Durchdringungschwelle geordnet werden können. Zukünftig wäre es eine sehr interessante Aufgabe, Simulationen zur Siliziumstruktur zu unternehmen sowie die Auswirkungen dieser kristallinen Schicht auf die Formation von Diamantkeimen in den amorphen Kohlenstoffilmen zu untersuchen.

Kapitel 4 handelt von der Simulation von amorphen Siliziumstrukturen. Genau das gleiche Programm für die Deposition, wie es in Kapitel 2 für Kohlenstoff entwickelt wurde, fand hierbei Anwendung. Wir haben einen gut getesteten tight-binding Hamiltonian benutzt um die interatomare Wechselwirkung zwischen Siliziumatomen zu beschreiben. Neun verschiedene amorphe Siliziumstrukturen wurden durch unsere numerische Depositionstechnik generiert. Zusätzlich wurde ein zehntes Modell durch schnelle Abkühlung präpariert, um den Unterschied zwischen atomarer Deposition und Abkühlen aus der Schmelze zu untersuchen. Der wohl bedeutungsvollste Unterschied zwischen diesen Modellen lag in den resultierenden Ringstatistiken,

beziehungsweise in der Medium-Range Order. Selbst Dreiecke sind in der atomaren Struktur sichtbar. Dies unterstützt drei andere unabhängige Hinweise auf die Existenz von Dreiecken in amorphen Siliziumstrukturen. Dennoch wurden in der Literatur strukturelle Einheiten wie gleichseitige Dreiecke weder bei Rechnungen zur elektronischen Zustandsdichte noch bei der Theorie des Aufbrechens schwacher Bindungen berücksichtigt. Letzterer ist der dominante Mechanismus bei der lichtinduzierten Defekterzeugung. Das tight-binding Modellpotential in unseren Computer Experimenten überschätzt etwas die Bindungslängen, indem es Werte für Silizium in der flüssigen Phase liefert. Es erzeugt überkoordinierte Atome (fünffach und sogar sechsfach koordinierte Atome) während der Simulation der amorphen Struktur. Die sechsfach koordinierten Atome finden sich in der flüssigen Phase von Silizium, nicht jedoch in der amorphen Phase. Das wohlbekannte klassische, empirische Stillinger-Weber Potential für amorphes Silizium hatte das gleiche Problem und wurde kürzlich modifiziert. Es wäre interessant, unser tight-binding Potential auf ähnliche Weise zu verbessern.

In Kapitel 5 schließlich wurden Rechnungen für die Hopping-Driftbeweglichkeit von Ladungsträgern in einer ein-dimensionalen Kette mit lokalisierten elektronischen Zuständen mit energetischer Unordnung ausgeführt. In den analytischen Rechnungen wurden exakte Ergebnisse wurden für Abhängigkeit der Beweglichkeit von der Temparatur und dem Feld für Systeme mit unkorrelierter Unordnung (Gaussches Unordnungsmodell) erzielt und soche für korrelierte Unordnug (korreliertes Unordnungsmodell) für asymmetrische und symmetrische Übergangswahrscheinlichkeiten. Es zeigte sich, daß diese Abhängigkeiten von der Länge des Systems abhängen. Daher könnten exakte Lösungen, wie sie üblicherweise für unendliche Systeme erzielt werden, für realistische dünne Systeme, wie sie in Anwendungen vorkommen, nicht relevant sein. In Bezug auf die Beschreibung der Transporteigenschaften von diskotischen flüssigkristallinen Gläsern sollte man daran erinnern, daß die echten Device-Proben normalerweise nur 50 bis 100 molekulare Sites in der Stapelrichtung aufweisen. Hierfür sind die in Abschnitt 5.2 für endliche Systeme erzielten Ergebnisse relevant. In den analytischen Rechnungen haben wir nur Übergänge der Ladungsträger zu den Nachbarsites auf der Kette betrachtet. Die Resultate der Monte-Carlo Computersimulationen zeigen, daß dagegen für Systeme mit unkorrelierter räumlich-energetischer Unordnung Variable-Range-Hopping eine wichtige Rolle spielt. Längere Elektronensprünge können die Resultate für die Feld- und Temperaturabhängigkeiten der Beweglichkeit der Ladungsträger ändern. Für solche Systeme können die analytischen Ergebnisse für die Transportkoeffizienten (aus Teil 5.2) als eine Approximiation betrachtet werden. Nimmt man zum Beispiel Sprünge über mehrere Nachbarn an, so bekommt man Werte für die Koeffizienten C, die die Temparaturabhängigkeit der Mobilität beschreiben (5.41), die ungefähr 10% von denjenigen abweichen, die man für ausschließliche Sprünge zu den nächsten Nachbarn erhält. Mit einer solchen

Genauigkeit kann man sogar analytische Ergebnisse (aus Teil 5.2) für Systeme mit unkorrelierter Unordnung benutzen. Jedoch ist im Fall korrelierter räumlich-energetischer Unordnung dieser Effekt viel weniger ausgeprägt. Dies impliziert, daß die exakten analytischen Ergebnisse für Hüpfen zum nächsten Nachbarn für solche Systeme ohne Einschränkung gültig sind.

Összefoglalás

Ez a dolgozat rendezetlen rendszerek különböző fizikai paramétereinek számítógépes módszerrekkel való vizsgálatával foglalkozik. Az utóbbi évtizedekben az információs technológiában a hihetlenül intezív és gyors fejlődés lehetővé tette a fizikusok számára a számítógépek nagyon hatékony használatát. A széleskörű alkalmazások kifejlesztettek egy új és ma már széles körű részét a fizikának, amely valahol az elméleti és kísérleti fizika közötti határmezsgyén található.

Az amorf anyagok fizikai tulajdonságainak megértéséhez nagyon fontos az atomi elrendezés ismerete. A rendezetlen rendszerek szerkezete általában függ az elkészítésük módszerétől. Ezért fontos, hogy ezt a fizikai folyamatot modellezük először, majd utána vizsgáljuk a kész szerkezeteket. A 2. fejezetben, amorf szén [111] szubsztrátum felett való molekuláris dinamikai növesztésének kisenergiás, atomi bombázásos módszer segítségével vizsgáltuk. Az volt a célunk, hogy több mint 100 részecskét tartalmazó, atomi skálán nagyméretű, amorf szén modelleket állítsunk elő a potenciál kvantummechanikai leírásával. A kölcsönhatást egy alaposan tesztelt és széles körben alkalmazott szoros kötésű (tight-binding) potenciállal modelleztük. A szerkezetek az atomok a szubsztrátumra való egymás utáni párologtatásos növesztésével készültek. A növekedés a kísérleteknek megfelelően volt szimulálva. Két különböző átlagos bombázási energiát, $E_{beam} = 1$ és 5 eV, és két különböző szubsztrát hőmérsékletet $T_{sub} =$ 100 és 300 K alkalmaztunk a 30 ps hosszú szimulációs idő alatt. A szimulációk 15 pssmal meg voltak hosszabítva $T_{sub} = 100$ K esetén, hogy nagyobb méretű szerkezeteket kapjunk. Hat darab modell készült el ezzel a párologtatásos módszerrel, két−dimenziós periódikus határfeltételt alkalmazva. A legfontosabb szerkezeti paramétereket, mint a sűrűséget, radiális eloszlás függvényt, koordinációs számot, szögeloszlást, és gyűrűstatisztikát elemeztük. A párologtatási ráta sokkal nagyobb volt mint a kísérletekben. A rendszer időfejlődését követő vizsgálatunk alapján azonban azt várjuk, hogy sokkal kisebb párologtatási ráta esetén sem kapnánk jelentős változásokat a modelljeinkben. Az általunk használt, kísérletekhez képest sokkal alacsonyabb szubsztrátum hőmérséklet gyorsabb energia disszipációt eredményez, és kissé kompenzálja a nagy párologtatási rátát.

A 3. fejezetben, gyémánt, kémiai gőzfázis leválasztású (Chemical Vapor Deposition - CVD), elektromos előfeszítéses nukleációs fázisának (Bias Enhanced Nucleation -

BEN) atomi szintű modellezése van összefoglalva. Különös figyelmet fordítottunk különböző szénhidrát (C_xH_y) gyökök, más-más kinetikus energiával való bombázására. Az eredmények azt mutatják, hogy nagyobb kinetikus energia mélyebb szubplantációt okoz és a gyökök disszociációja is gyakoribb. Az acetilén (C_2H_2) esetén a szén-szén kötés nagyon ritkán bomlik fel alacsony energás (20, 40 eV) bombázás esetén, viszont az esetek 50−90%-ban felbomlik nagyobb energiák esetén (80 eV). A számítógépes kísérletek kimutatták, hogy körülbelül az esetek 60%-ban a szén-hidrogén kötés felbomlik a szubplantáció során. A metil (CH_3) esetén általában az egyik szén-hidrogén kötés megmarad, és a másik két hidrogén H_2 molekulát alkot. A tipikus 200 V-os előfeszítés esetén, ami optimális a gyémánt nukleusz képződéséhez a BEN során, a C_2H_2 gyökök 80 eV-os, míg a CH_3 ion gyökök 40 eV-os kinetikus energiával rendelkeznek. Ennél az előfeszítésnél, jelentős különbségek figyelhetőek meg a két gyök által okozott amorf szén vékonyrétegbeli szerkezeti átrendeződésében. A C_2H_2 gyök esetén, a behatolás mélyebb és a gyök mélyebb tartományokban okoz változásokat mint a CH_3 gyök. A CH_3 lövedék nem járul hozzá mély változásokhoz az amorf rétegben és csak a felület közelében okoz struktúrális átalakulásokat. A vékonyrétegben megfigyelt szerkezeti változások kimutatták, hogy nagyobb kinetikus energiájú gyökök az átlagos behatolási mélység alatt egy vastag, sp^3 hibridekben gazdag réteget hoznak létre és a felület pedig sp^2 hibridekkel rendelkező atomokból áll. A határ eközött a két réteg között lejjebb tolódik nagyobb bombázási energia esetén. Az eredményeink megerősítik a szubplantációs modell alkalmazását. Egy igen érdekes feladat lehet a jövőben megismételni a szimulációs kísérleteket egy szilícium szubsztrátum felett, és vizsgálni ennek a kristályos rétegnek a hatását az amorf szén vékonyrétegben a gyémánt nukleuszok kialakulásához vezető folyamatát.

A 4. fejezet az amorf szilícium szerkezetének szimulációjával foglalkozik. Ugyanazt az atomi párologtatási programcsomagot használtuk, mint amelyet kifejlesztettünk az amorf szén növesztésének vizsgálatára és a 2. fejezetben mutattunk be. Egy széles körben tesztelt, szoros kötésű (tight-binding) Hamiltont formalizmust alkalmaztunk a szilícium atomok közötti kölcsönhatás leírására. Egy hasonló szoros kötésű potenciált fejlesztett ki ugyanez a kutatócsoport a szén rendszerekre és mi ezt alkalmaztuk eredményesen az amorf szén vékonyrétegek növesztésének leírására (ld. 2. fejezet). Kilenc különböző amorf szilícium szerkezetet készítettünk el a számítógépes párologtatási módszerünkkel. Egy további tizedik modell gyorshűtéses technikával készült el, hogy összehasonlítsuk az atomi párologtatási és az olvadék hűtéses módszerek közötti különbségeket. Az általunk talált legfontosabb különbség a gyűrűstatisztikában figyelhető meg, azaz a középtávú rendben. Háromszögek ugyancsak megtalálhatóak az atomi elrendezésben, megerősítve ezzel három korábbi független bizonyosságát a háromszögek előfordulásának az amorf szilíciumban. Mindamellett, olyan fragmensek, mint például egyenlő oldalú háromszögek sohasem voltak figyelembe véve az elektron állapotsűrűség számításánál, illetve olyan megoldatlan problémák

esetén, mint a gyenge kötések felbomlása hosszú megvilágítás esetén, ami a fő mechanizmusa a fény által indukált hiba keltésének. A szoros kötésű modell potenciál egy picit túlbecsüli a kötéstávolságot a számítógépes kísérleteinkben, olyan értékeket adva, amelyeket korábban folyadék szilíciumban figyeltek meg. Az amorf szilícium szerkezetének szimulációja során a potenciál túlkoordinált atomokat is ad (ötös, sőt hatos koordináltságú atomokat is). Hatos koordináltságú atomok, inkább a szilícium folyadék fázisában találhatóak, mint az amorf szilíciumban. Az amorf szilícium esetében a jól ismert Stillinger-Weber klasszikus empirikus potenciál is hasonló nehézségekkel küzdött, és mostanában eredményesen lett módosítva. Egy jövőbeli cél lehet a szoros kötésű (tight-binding) potenciál hasonló módon való javítása.

Végezetül, az 5. fejezetben, egy egy-dimenziós rendezetlen lokalizációs energia állapotokon keresztül haladó töltéshordozók mozgékonyságának számítása található meg. Az analitikus számításokban, egzakt eredményeket kaptunk a mozgékonyság elektromos térerősség és hőmérséklet függésére mind nemkorrelált rendezetlen rendszer esetén (Gaussian disordered model - GDM) és mind korreláció esetén is (correlated disorder model - CDM), asszimetrikus és szimmetrikus átmeneti ráták esetén egyaránt. Ezek az eredmények a rendszer méretétől függenek. Ezért még az egzakt megoldások végtelen hosszú rendszerek esetén is érvényüket veszthetik olyan vékony minták esetén, amelyeket a valódi alkalmazásokban használnak. Középpontba helyezve az úgy nevezett oszloposan korongszerű folyadékkristályokat, figyelembe kell venni, hogy az alkalmazott eszközök általában csak 50-100 "építő elemből" állnak. Ilyen rendszerek esetén az 5.2. alfejezetben kapott elméleti eredmények közül a véges méretű rendszerekre kapott eredményeket kell alkalmazni, a végtelen hosszú rendszerekre levezetett eredmények helyett. Az analitikus számítások során a töltéshordozók hoppingjánál csak elsőszomszéd átmeneteket vettünk figyelembe. A Monte Carlo szimulációk eredményei kimutatták, hogy azokban a rendszerekben, ahol nincs korreláció az energia és lokalizációs állapotok térbeli elhelyezkedése között, a változó távolságú hopping fontos szerepet játszik és hatással van a töltéshordozó mozgékonyságának térerősség és hőmérséklet függésre (ld. 5.3. alfejezet). Ezekre a rendszerekre a transzport együtthatókra kapott analitikus eredmények közelítésként alkalmazhatóak. Például, ha távolabbi szomszéd hoppingot is figyelembe veszük, akkor a C együtthatóra, ami a mozgékonyság hőmérséklet függését írja le az (5.41) egyenletben, 10%-os különbség található a csak elsőszomszéd hoppingra levezetett eredményekhez képest. Ilyen hiba mellett, akár az analitikus eredmények (ld. 5.2. alfejezet) is mérvadóak lehetnek a korrelálatlan rendszerekben. Ugyanakkor, a korrelált rendezetlenség esetén, ez az effektus sokkal kisebb, utalva arra, hogy az elsőszomszéd hoppingra kapott egzakt analitikus eredmények különösebb korlátozások nélkül érvényesek ezekben a rendszerekben.

Acknowledgments

In Riezlern (September, 1999) I was really fortunate, as after we had dinner I could sit down and talk about my research with three very clever people. Basically, PD Dr. Sergei Baranovskii was explaining the model of a physical problem to me that I was going to work on in the following months. At that conversation Professor Peter Thomas said a sentence, which I shall never forget. The sentence went like this *"This problem is very easy to solve with computer simulations!"*. First I thought that Professor Peter Thomas should be right. However, the first reaction of Dr. Sergei Baranovskii was to say, *"Wait, maybe it is not that easy"*. By that time I had executed lots of computer simulations, bad ones as well as good ones. In the following two years after that discussion further thousands of programs were executed. This Ph.D. thesis tries to summarize how "*easy*" this work was. Furthermore, according to the sentence of my Hungarian supervisor Dr. Sándor Kugler *"The working hours of a Ph.D. student is 168 hours weekly, plus overtime."*, I hope the thesis shows how much work I did or I did not.

The present Ph.D. work was done under the (patient) guidance of my two supervisors, Dr. Sándor Kugler and PD Dr. Sergei Baranovskii. Words are not appropriate enough to express my gratitude to these two people, who have done an excellent job in edifying guidance. I am eternally grateful to Professor Peter Thomas for his valuable and helpful discussions and for organizing my stays in Marburg.

During the three years of work I had the opportunity to be a member of two scientific groups. The first being with Theoretical Physics Department at the Budapest University of Technology and Economics, and the second in the Semiconductor Group of the Institute of Physics at the Philipps–Universität Marburg. I would like to thank all of the members of those groups for the various help they supplied to me. Let me name a few of them here; Dr. István László for his valuable help and discussions during the developments of the tight-binding molecular dynamics program code; Dr. Harald Cordes, with whom we worked on the one–dimensional hopping transport problem in disordered organic solids; and some of the Ph.D. and ex-Ph.D. students: László Borda, Ralf Eichmann, László Kullmann, Dr. János Török, and Tamás Unger.

I would also like to thank Dr. Péter Deák (Department of Atomic Physics, Budapest University of Technology and Economics) and Professor Thomas Frauen-

heim (Department of Theoretical Physics, Universität-GH Paderborn) for organizing my summer work in Paderborn in 1999. In addition I would like to thank all the members of these departments for their support and I would like to name among them Dr. Szabolcs Kátai, who helped me to understand in more detail the experimental results of the field I worked in and Dr. Zoltán Hajnal, who helped me greatly in understanding the TBMD program code developed by the group in Paderborn.

Finally, I would like to thank my family for their continuous support and patience. Last, but not least, I would like to thank my girlfriend Sophie for simply everything and for making me happy all the time.

List of publications

1.) Krisztian Kohary, Sandor Kugler, Istvan Laszlo: *"Molecular dynamics simulation of amorphous carbon structures"*, J. Non-Cryst. Solids, 227-230 (1998) p594-596.

2.) Krisztián Koháry: *"Molecular Dynamics Simulation of Amorphous Carbon Structures"*, (thesiswork written in Hungarian)

3.) S. Kugler, K. Kohary, I. Laszlo: *"Microscopic Structure of Amorphous Carbon. Tight-Binding Molecular Dynamics Study"*, Proceedings of N2M Workshop, Grenoble, France, 1998. AIP Conference Proceedings 479. p64-69.

4.) S. Kugler, I. Laszlo, K. Kohary, K. Shimakawa: *"Molecular dynamics simulation of amorphous carbon structures"*, Functional Materials **6**, No.3 (1999) p459.

5.) K. Kohary, S. Kugler: *"Growth of amorphous semiconductors: tight-binding molecular dynamics study"*, J. Non-Cryst. Solids, 266–269 (2000) p746-749.

6.) H. Cordes, S. Baranovskii, K. Kohary, P. Thomas, S. Yamasaki, F. Hensel, and J−H. Wendorff: *"One-dimensional hopping transport in disordered organic solids. I. Analytic calculations"*, Phys. Rev. B **63**, 094201 (2001).

7.) K. Kohary, H. Cordes, S. Baranovskii, P. Thomas, S. Yamasaki, F. Hensel, and J−H. Wendorff: *"One-dimensional hopping transport in disordered organic solids. II. Monte Carlo simulation"*, Phys. Rev. B **63**, 094202 (2001).

8.) K. Kohary, S. Kugler: *"Growth of amorphous carbon. Low energy Molecular Dynamics simulation of atomic bombardment"*, Phys. Rev. B **63**, 193404 (2001).

9.) S.D. Baranovskii, H. Cordes, K. Kohary, and P. Thomas: *"On disorder-enhanced diffusion in condensed aromatic melts"* (accepted for publication in Phil. Mag. B)

10.) K. Kohary and S. Kugler: *"Time development during growth and relaxation of amorphous carbon films preparation. Tight-binding molecular dynamics study."* (submitted)

11.) K. Kohary, S. Kugler, Z. Hajnal, Th. Köhler, Th. Frauenheim, Sz. Kátai, and P. Deák: *"Atomistic simulation of the bombardment process during the BEN phase of diamond CVD"* (submitted)

12.) S. Kugler, Z. Várallyay, and K. Kohary: *"Growth of amorphous silicon. Low energy molecular dynamics simulation of atomic bombardment II."* (in preparation)

13.) I.P. Zvaygin, S.D. Baranovskii, K. Kohary, H. Cordes, and P. Thomas: *"Hopping in Quasi-One-Dimensional Disordered Solids: Beyond the Nearest-Neighbor Approximation"* (in preparation)

Curriculum Vitae

1st February, 1975	Born in Kaposvár (Hungary) Parents: Koháry István and Kováryné Drajkó Ágnes
1981-1986	Gárdonyi Géza Primary School, Budapest (Hungary)
1986-1988	29th Primary and Secondary School, Kalinin (U.S.S.R.)
1988-1989	Gárdonyi Géza Primary School, Budapest (Hungary)
1989-1993	Szent István Secondary School, Budapest (Hungary)
11th June, 1993	A-level exam
1993-1998	Studies in Engineering Physics at Budapest University of Technology and Economics (Hungary)
16th June, 1998	M.Sc. in Engineering Physics
From 1st September, 1998	PhD student at Budapest University of Technology and Economics (Hungary) and Philipps–Universität Marburg (Germany) (mutual education)